CERN/SPSC 99-20
SPSC/M635
LNGS-LOI 19/99
August 27, 1999

A long baseline ν_τ appearance experiment in the CNGS beam from CERN to Gran Sasso

(PROGRESS REPORT)

The OPERA Collaboration

K. Kodama, N. Ushida
Aichi University of Education, Aichi, Japan
M. Guler, E. Pesen[1], M. Serin-Zeyrek, R. Sever, P. Tolun, M.T. Zeyrek
METU, Ankara, Turkey
D. Duchesneau, J. Favier, H. Pessard
LAPP, IN2P3-CNRS and Université de Savoie, Annecy, France
M.T. Muciaccia, P. Righini, S. Simone
Bari University and INFN, Bari, Italy
C. Haeberli, M. Hess, R. Klingenberg, U. Moser, K. Pretzl, M. Weber
Bern University, Bern, Switzerland
L. Benussi, G. Van Beek, P. Vilain, G. Wilquet
IIHE (ULB-VUB), Brussels, Belgium
M. Spinetti, L. Votano
LNF, Frascati, Italy
T. Kawamura, S. Ogawa, H. Shibuya
Toho University, Funabashi, Japan
J. Dupraz, J.P. Fabre, P. Schilly, U. Stiegler
CERN, Geneva, Switzerland
J. Goldberg, M. Khalifa
Israeli group c/o Technion, Haifa, Israel
F.W. Buesser, A. Geiser, K. Höpfner, B. Koppitz, B. Naroska, W. Schmidt-Parzefall, R. van Staa
Hamburg University, Hamburg, Germany
S. Aoki, T. Hara
Kobe University, Kobe, Japan
L. Chaussard, M. Chemarin, Y. Déclais, P. Jonsson, S. Katsanevas, I. Laktineh, J. Marteau, G. Moret
IPNL, IN2P3-CNRS and Université C. Bernard Lyon I, Villeurbanne, France
A. Artamonov, P. Gorbounov, V. Khovansky
ITEP, Moscow, Russia
N. D'Ambrosio, P. Boschan, D. Frekers, D. Rondeshagen, J. Schmand, H.J. Wörtche, T. Wolff
Münster University, Münster, Germany
K. Hoshino, M. Komatsu, M. Miyanishi, M. Nakamura, T. Nakano, K. Niwa, O. Sato
Nagoya University, Nagoya, Japan
N. Bruski, S. Buontempo, F. Carbonara, A. G. Cocco, V. Cuomo, G. De Lellis, A. Ereditato[2], G. Fiorillo, R. Listone, M. Messina, P. Migliozzi, S. Sorrentino, P. Strolin[3], V. Tioukov
"Federico II" University and INFN, Naples, Italy
J.E. Campagne, B. Merkel, J.P. Repellin, J.J. Veillet
LAL, IN2P3-CNRS and Université Paris-Sud, Orsay, France
G. Rosa
"La Sapienza" University and INFN, Rome, Italy
E. Barbuto, C. Bozza, G. Grella, G. Romano
Salerno University and INFN, Salerno, Italy
Y. Sato, I. Tezuka
Utsunomiya University, Utsunomiya, Japan

[1]Presently at CERN.
[2]Contactperson.
[3]Presently CERN Scientific Associate.

ABSTRACT

The OPERA[4] experiment is designed for the appearance search of $\nu_\mu \leftrightarrow \nu_\tau$ oscillations in the parameter region indicated by Super-Kamiokande, as the explanation of the zenith dependence of the atmospheric neutrino deficit. OPERA is a long baseline experiment to be located at the Gran Sasso Laboratory in the CNGS[5] neutrino beam from the CERN SPS. The detector is based on a massive lead/nuclear emulsion target. Nuclear emulsions are used as tracking devices, for the direct observation of the decay of the τ leptons produced in ν_τ charged current interactions. Electronic detectors locate the events in the emulsions. Iron spectrometers measure charge and momentum of muons. The discovery potential of OPERA is ultimately due to a very low background level and could therefore play a decisive role in the clarification of the experimental scenario. In this Report the progress in the design of the experiment is presented. The OPERA performance is described in the light of more refined detector simulations, of experience gained with emulsions, of test measurement results and of the new CNGS beam design.

[4]Oscillation Project with Emulsion-tRacking Apparatus.
[5]Cern Neutrino beam to Gran Sasso.

Contents

Chapter 1

Introduction

1.1 Physics motivations

The possibility of a non-vanishing mass for the neutrino is one of the most intriguing questions of particle physics. On the one hand, there are no fundamental principles for the neutrino to be massless; on the other hand, a neutrino mass would be a direct indication of physics beyond the *Standard Model* of elementary particles, representing a fundamental milestone in particle physics, astrophysics and cosmology.

Most likely, the neutrino mass is too small and therefore out of reach of direct measurements based on kinematical methods [1, 2], One way to assess this issue with high sensitivity is to search for a process which may only occur if the neutrino has non vanishing mass, even if very low. Neutrino oscillations are such a process. They were originally postulated by Pontecorvo [3, 4] in terms of $\nu \leftrightarrow \bar{\nu}$ oscillation, before the discovery of distinct neutrino flavours. Maki et al. [5] introduced the possibility of neutrino flavour transitions with a mixing matrix, until the present description of the phenomenon in terms of weak and of mass eigenstates was provided [6].

According to the oscillation mechanism, a massive neutrino of a given weak interaction eigenstate, ν_e, ν_μ or ν_τ, may be seen as a different eigenstate at some distance from the source. The corresponding probability has an oscillatory behaviour (hence *oscillation*) with parameters which can be determined by experiments. In the simplified scheme where oscillations occur dominantly between a pair of neutrino flavours, they are described by two quantities: the mixing parameter $\sin^2 2\theta$ (related to the oscillation amplitude) and the mass squared difference Δm^2 between the two mass eigenstates. The sensitivity of the experimental searches to the above parameters depends on the neutrino energy E and on the distance L of the detector from the neutrino source.

The Kamiokande Collaboration [7] indicated neutrino oscillations as an explanation of the observed zenith dependence of the ratio of atmospheric muon neutrinos to electron neutrinos. The best fit to their data gives, in terms of $\nu_\mu \leftrightarrow \nu_\tau$ oscillations, $\Delta m^2 = 1.6 \times 10^{-2}\ eV^2$ and $\sin^2 2\theta = 1$. The CHOOZ reactor experiment excluded to a large extent the possibility of $\nu_\mu \leftrightarrow \nu_e$ oscillations [8] leaving open the interpretation in terms of $\nu_\mu \leftrightarrow \nu_\tau$ oscillations. The introduction of a fourth *sterile* neutrino would also allow $\nu_\mu \leftrightarrow \nu_{sterile}$ oscillations as a possible explanation of the experimental results.

The Super-Kamiokande experiment has then confirmed the Kamiokande result with a statistics several times larger [9], making a strong claim for the observation of neutrino oscillations. The interpretation in terms of $\nu_\mu \leftrightarrow \nu_{sterile}$ is still possible but the probability is somewhat worse than for the $\nu_\mu \leftrightarrow \nu_\tau$

hypothesis [10]. The data also disfavour the $\nu_\mu \leftrightarrow \nu_e$ oscillation interpretation. The above results have been confirmed by data on upward muons produced by neutrinos interacting with the rock surrounding the detector [11].

A combined analysis of all the Super-Kamiokande measurements (*sub-GeV*, *multi-GeV* and upward-going muons) has then been performed with improved statistics and knowledge of systematic effects [10]. The result gives $\Delta m^2 = 3.5 \times 10^{-3}\ eV^2$ and $\sin^2 2\theta = 1$ constraining at the 90% CL the oscillation parameters in the region of $\sin^2 2\theta > 0.8$ and $\Delta m^2 = (2-6) \times 10^{-3}$.

The Soudan2 experiment, exploiting a fine-grained tracking calorimeter, also observed a smaller than expected yield of ν_μ, although with less pronounced zenith angle dependence [12]. Soudan2 has a better angular resolution than Super-Kamiokande but a lower statistics. Finally, the MACRO experiment at the Gran Sasso [13], based on a massive calorimeter, also detected a statistically significant muon neutrino deficit consistent with the Super-Kamiokande observations.

The above parameter region is accessible by long baseline accelerator experiments. The OPERA experiment aims at a high sensitivity search for $\nu_\mu \leftrightarrow \nu_\tau$ oscillations. The experiment exploits nuclear emulsion as high resolution tracking devices for the direct detection of the τ lepton, produced in the charged current interaction of the ν_τ with the target. The experiment is designed for a long baseline oscillation search in the proposed CNGS beam [14] from the CERN SPS to the Gran Sasso Laboratory. Thanks to its capability of identifying electrons and to the small contamination of ν_e in the beam, the experiment will also accomplish a $\nu_\mu \leftrightarrow \nu_e$ oscillation search. The design principles of the experiment can be found in the Letter of Intent [15, 16].

The technique of nuclear emulsion has found a large scale application in the target of the CHORUS experiment [17], where the automatic scanning of a large samples of events has first been applied. This technique can be further improved for future $\nu_\mu \leftrightarrow \nu_\tau$ oscillation searches (see references quoted in [15]). In [18] and [15] the conceptual design of OPERA, a massive detector capable of exploring the atmospheric neutrino region with high sensitivity, was outlined. Emulsions are used exclusively as high precision trackers, unlike in CHORUS where they constitute the active target itself. The extremely high space resolution of the emulsion is suited for the detection of the short-lived τ lepton produced in ν_τ interactions.

The feasibility of OPERA implies, on the one hand, the production of emulsions at industrial scale and, on the other hand, it is linked to the impressive progress in the field of computer controlled microscopes read out by CCD cameras, with automatic pattern recognition and track reconstruction [19]. After its pioneering work, the Nagoya group of the CHORUS and OPERA Collaborations has delivered a third generation automatic system about 1000 times faster than previous semi-automatic systems [20]. Improvements are expected from the intense R&D programmes underway in Europe and Japan, in particular within several groups of the OPERA Collaboration.

This progress has determined a real revolution in the field of nuclear emulsion detectors. They can nowadays be considered *tracking* devices and no longer *visual* detectors. The analysis can be conducted in automatic mode without human intervention. The study of specific events can be carried out with graphic display tools applied after the event reconstruction, in the same way as for electronic detectors.

From 1999 onwards, the K2K experiment [21] will be searching for ν_μ disappearance by using the long baseline neutrino beam from KEK to Super-Kamiokande (250 km away). Given the low beam energy, which is below the kinematical threshold for τ production, K2K will not perform a $\nu_\mu \leftrightarrow \nu_\tau$ appearance search needed to reveal the source of the Super-Kamiokande signal.

The straightforward way to confirm the $\nu_\mu \leftrightarrow \nu_\tau$ oscillation indicated by atmospheric neutrinos is to use long baseline beams at the energies required for the detection of ν_τ charged current (CC) interactions. These beams provide higher intensities than atmospheric neutrinos and their features can be tuned according to the specific physics goal. This approach is complementary to that followed by the proposed atmospheric-neutrino calorimetric detector [22].

At Fermilab, the MINOS experiment [23] is approved and will use the NuMI beam [24] from Fermilab to the Soudan Mine, at 730 km distance, to test the hypothesis of neutrino oscillations with $\Delta m^2 \sim 10^{-2} - 10^{-3}\ eV^2$. The high repetition rate of the 120 GeV Main Injector make it suitable to perform a ν_μ disappearance experiment and a statistical search for ν_τ appearance by exploiting the measurement of the NC/CC ratio.

The CNGS facility from the CERN SPS to the Gran Sasso Laboratory is planned to deliver a ν_μ beam from 2005 onwards. In the hypothesis that $\nu_\mu \leftrightarrow \nu_\tau$ oscillations are the explanation of the observed atmospheric ν_μ deficit, a sizeable amount of ν_τ events could be observed by suitable detectors. The optimisation of the CNGS for ν_τ appearance coupled with the features of the OPERA detector offer the specific possibility of the observation of the τ production and decay.

1.2 Nuclear emulsion detectors for a ν_τ appearance search

The Emulsion Cloud Chamber (ECC) is a massive emulsion detector made of a sandwich of passive material plates interspaced with nuclear emulsion layers used as high precision tracking devices. We will see in the following that the present experience with the ECC, combined with the availability of automatic emulsion scanning devices allows us to conceive and realize a $\sim$ 1000 ton fine-grained vertex detector for the identification of ν_τ appearance in the CNGS beam.

1.2.1 The current emulsion technology

Nuclear emulsion as analog data storage

The development and the utilisation of automatic scanning systems have completely changed our idea of nuclear emulsions. Nowadays, nuclear emulsion can be considered as a data storage device which allows to record 3D vectors of particle tracks whose data are read out by automatic scanning systems.

Nuclear emulsions are made of micro-crystals of silver halides (AgBr) as sensitive devices dispersed in a thin gelatin layer. The size of the micro crystals ranges from 0.2 to 0.3 μm and the concentration of the crystals in the emulsion goes from ~ 25 to $\sim 50\%$ in volume. The dimensions and the type of the crystals can be well controlled by the current advanced industrial technologies developed for photographic films.

Emulsion Sheets (ES) have nuclear emulsion layers on both sides of a transparent plastic base whose thickness ranges from 70 to 1000 μm just like optical storage media (*e.g.* CD-R). The thickness of the emulsion layer can vary from 50 to 500 μm, depending on the specific use. For OPERA, as shown later, we are planning to use 50 μm thick emulsion layers on both sides of a 200 μm thick plastic base.

The incident particle beam has usually a direction perpendicular to the ES surface. When an ionising particle traverses the emulsion layer of an ES electron-hole pairs are created in the crystals. Clusters of several silver atoms are formed in several micro crystals by successive ionic processes.

Contrary to CD-R, chemical processing is required to make the ES readable by scanning systems. By chemical action the small silver clusters (called latent image) are amplified and silver clusters with diameter of $\sim 0.6\ \mu m$ are formed, which can be identified by the optical pick-up of the scanning system, *i.e.* by a microscope equipped with a CCD camera.

The recorded data of the ES are read out by automatic scanning systems. In this Section, we will refer to the Track Selector (TS) as an example of these systems, since it is routinely used in experimental data analysis. The basic components of the TS are designed to detect tracks with a predicted angle in the field of view of the CCD camera. The area of the view is $\sim 150 \times 120\ \mu m^2$. It is determined by the microscope optics and by the surface of the CCD. The focal depth of the microscope gives an image relative to $\sim 5\ \mu m$ of emulsion thickness.

The track detection algorithm is simple. Sixteen tomographic images of (*e.g.*) $100\ \mu m$ thick emulsion layers are taken and digitised. Every digitised image is shifted horizontally relative to the first layer, so that the predicted angle tracks become perpendicular to the emulsion surface. By superimposing the sixteen shifted digitised images tracks are identified as enhancements of pulse heights, as shown in Fig. 1.1. The quality of one track segment is measured by the signal pulse height. This value is strongly correlated to the grain density which is the conventional sensitivity parameter of nuclear emulsions. The emulsion sensitivity could be such that the track of a minimum ionising particle appears as a trail of 300 to 500 grains/mm (with average spacing of 2 to 3 μm).

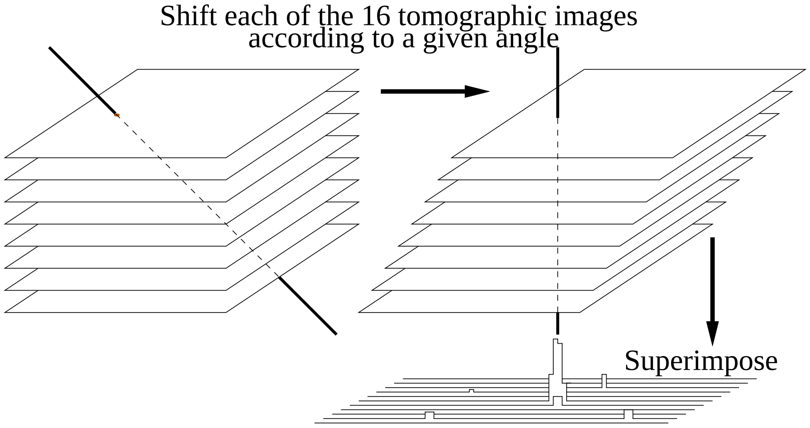

Figure 1.1: Principle of the Track Selector.

Outputs from the TS are the position (x, y, z) and the angle $(\theta x, \theta y)$ of the detected tracks (track segments). The efficiency of track recognition can be checked for each specific experimental application. In Fig. 1.2, the angular dependence of this efficiency is shown for the CHORUS experiment. The efficiency is higher than 98% up to about 400 $mrad$. One has to note that a space angular interval of $400\ mrad \times 400\ mrad$ includes about 95% of the emitted leptons from CNGS charged current neutrino interactions. The measured angular resolution is $\sim 2\ mrad$ by using $100\ \mu m$ long track segments. The corresponding position resolution is $0.6\ \mu m$ (Fig. 1.3).

In the Emulsion Cloud Chamber (ECC), which can be considered as an event data recorder, several ESs are stacked with passive material plates in a sandwich-like structure, as shown in Fig. 1.4. In Section 1.2.2,

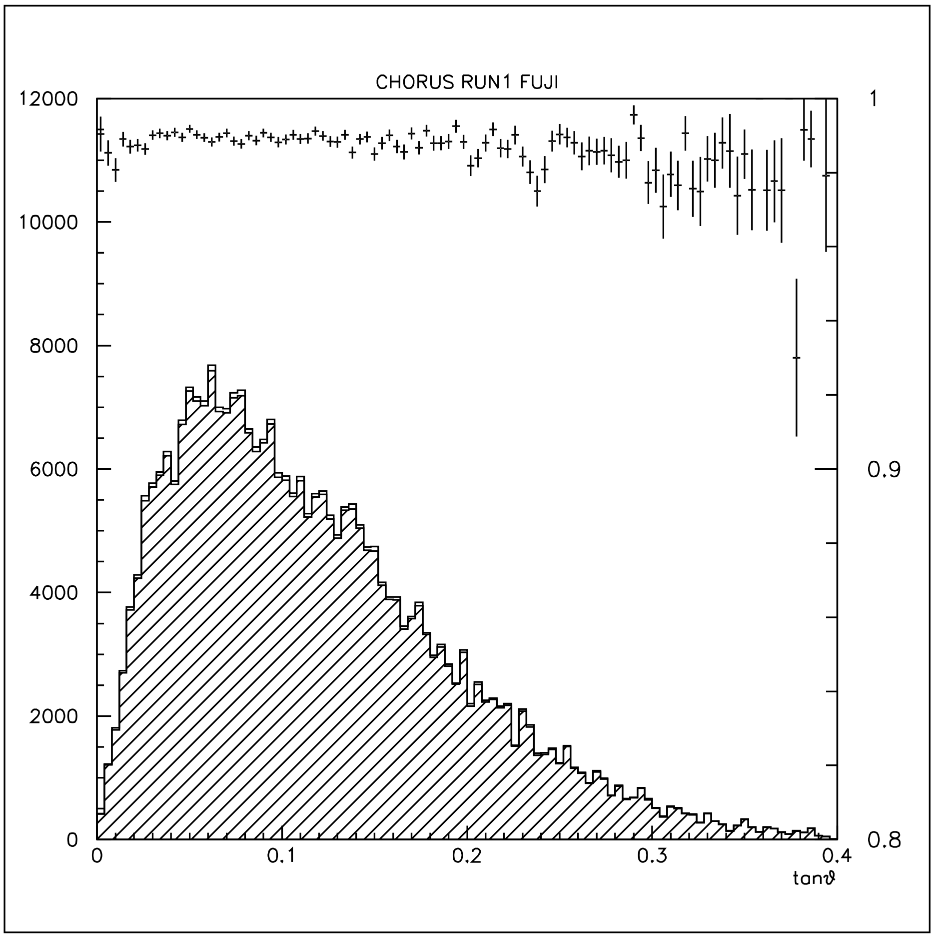

Figure 1.2: Angular dependence of the track detection efficiency of the Track Selector. Left scale: histogram of the reconstructed tracks; right scale: detection efficiency.

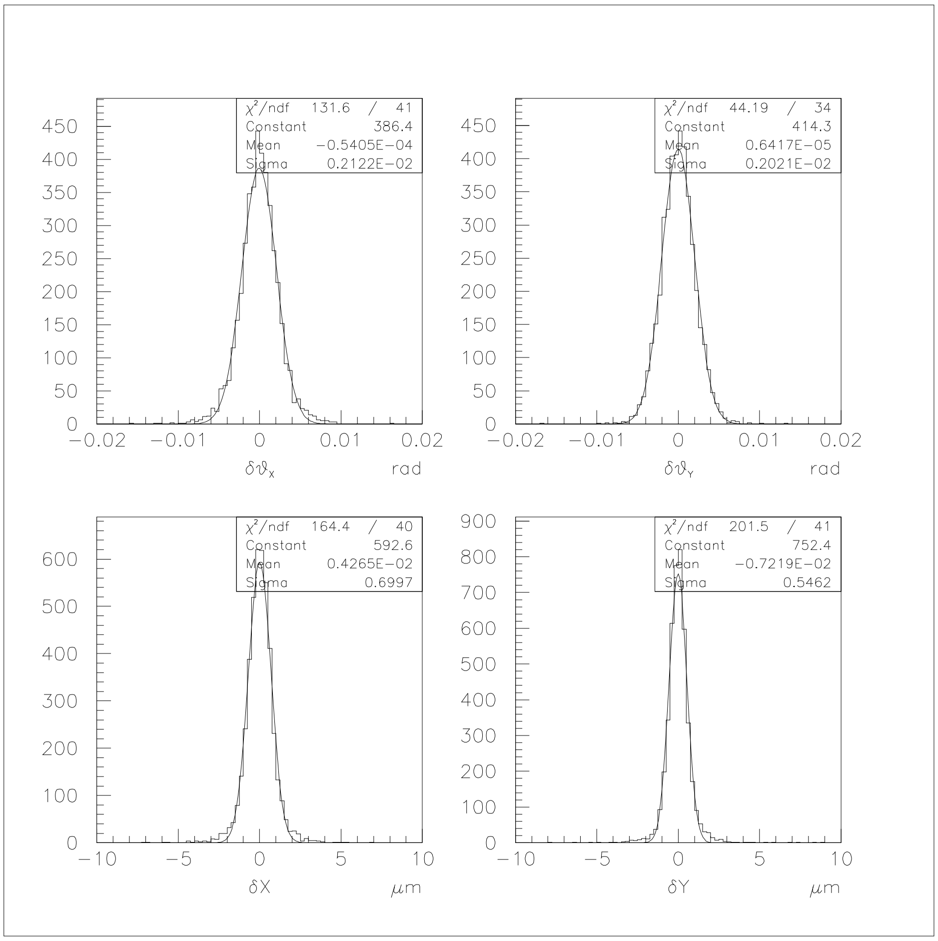

Figure 1.3: Position and angular resolution of the Track Selector obtained with 100 μm emulsion track segments.

the history and the general features of the ECC will be briefly reviewed.

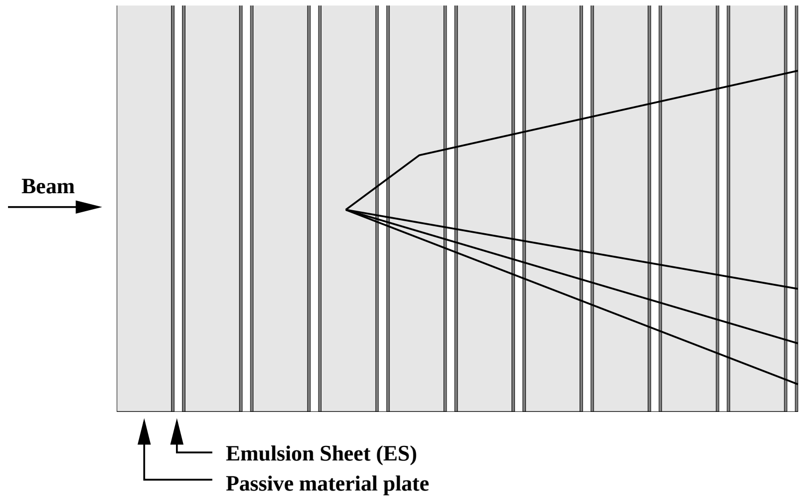

Figure 1.4: Schematic structure of an Emulsion Cloud Chamber (ECC).

Net Scan for general event analysis

Currently available scanning systems can scan wide space-angle intervals by using pipelined parallel processing. As an example, with the most recent TS generation (the Ultra-Track Selector (UTS)) all tracks in a space angle of 400 $mrad \times 400$ $mrad$ can be detected within 0.3 s. This corresponds to a scanning speed of ~ 1 $cm^2/hour$/system.

One application of the wide space-angle scanning is in the event vertex location, without the help of any precise prediction of track direction or vertex position. The DONUT experiment at Fermilab [25], aimed at the direct observation of prompt ν_τ, is presently employing nuclear emulsions with an ECC for the detection of the τ decay possibly coming from ν_τ CC interactions. In DONUT as well as in CHORUS, the so-called *Net Scan* is being used for the location of special events. With this procedure, for an event vertex position roughly predicted within a volume, typically of $1 \times 1 \times 2$ cm^3, 1 cm^2 of the surface of each emulsion layer contained in the volume is scanned. All the track segments detected within a wide 400 $mrad \times 400$ $mrad$ angular acceptance are recorded.

After this online data taking off-line processing is applied. One can then perform, for example, track connections between consecutive emulsion plates, relative alignment of the plates by maximising the number of associated track segments (recursive process), interaction (and decay) vertex finding by using connected tracks, etc. These tasks can be accomplished by off-line computers in a way analogous to the analysis of electronic detector data.

In Fig. 1.5, one example of *Net Scan* is shown. These data have been taken from the DONUT ECC. In that ECC the passive material is stainless steel (1 mm thick) interspaced with ESs made of 100 μm thick emulsion layers on both sides of a 200 μm thick plastic plate. The scanned area transverse to the beam is 5×5 mm^2, for each of the emulsion layers contained in eight emulsion/steel cells. This corresponds to ~ 1 cm in depth.

The total number of picked-up track segments is about 100000. By applying track reconstruction ~ 7000 tracks (60000 segments) are reconstructed in the fiducial volume. The remaining ~ 40000 single-track segments (corresponding to very low energy particles) and ~ 6000 tracks due to passing through background muons are rejected. About 900 tracks which stop in the fiducial volume are retained. After rejecting tracks with large scattering angle 180 high energy particle tracks remain. Next, a vertex search is applied by requiring at least two tracks to converge within an impact parameter of $\sim 10\ \mu m$. This allows to finally detect one clear neutrino vertex.

The accuracy in the determination of the impact parameter is given by the error on the measurement of the track segments and by the distance between the ES and the vertex. The rms of the measurement is about 2 μm for a distance between ES and vertex of 1 mm. Using connected tracks between consecutive plates improves the impact parameter resolution due to the higher angular resolution. Multiple scattering has also to be included in determining the cutting value for the impact parameter distribution.

Also the decay search is performed by using the measured track segments. Secondary interactions and secondary decay vertices can be detected in two ways: by identifying the daughter tracks emerging downstream from the located vertex or by detecting parent particle tracks which are associated to the located vertex and disappear downstream. Once a decay is detected further analysis can be applied to the daughter particle tracks in order to measure their momentum and perform particle identifications *e.g.* by identifying electrons.

The performance of off-line programs can be continuously improved after the emulsion data taking. In particular, the ongoing analyses of the DONUT and CHORUS data will be a test bench for the development of off-line algorithms to be used in the OPERA event analysis.

1.2.2 Brief history of the Emulsion Cloud Chamber (ECC)

The use of ECC detectors has been continuously developing in Japan since the late fifties until nowadays with a main field of application in cosmic ray experiments. In those early days, the main reason of the use of the ECC structure was the need to maximise the active detector area and acceptance though limiting the amount of emulsions. This was pragmatically motivated by those day's economical situations of Japan.

Although the utilisation of the ECC was stimulated by the work of Kaplon et al. [26] several applications have been developed in Japan since then. The first notable physics result obtained with an ECC was in 1956 the measurement of the transverse momentum of multi particle production in high-energy hadron interactions [27]. A schematic view of the ECC used in that experiment is shown in Fig. 1.6 (left part). The structure was separated into two parts: a so-called production layer with low Z material and an analysing layer with high Z material. In that study, the p_t distribution of the produced π^0 was measured by detecting cascade showers initiated by the daughter γ rays. The energies of the γs were estimated by comparing the measured transition curve with the predictions from the theory of cascade showers developed by Nishimura and Kamata [28]. The measured distribution and the average value agree well with those obtained in accelerator experiments which were carried out about 10 years later.

After this success, the ECC technique developed in two different ways. One consisted in building large size detectors at high altitudes, like for the experiments on Mt. Norikura [29], Mt. Chacaltaya [30], Mt. Pamir [31], Mt. Fuji [32] and Mt. Kanbala [33], which took advantage of the cost effectiveness of the ECC structure. The physics motivation was the observation of rare events at extremely high energies. The intention was to use the atmosphere as a target and the ECC as an analyser. Those ECCs consist of a

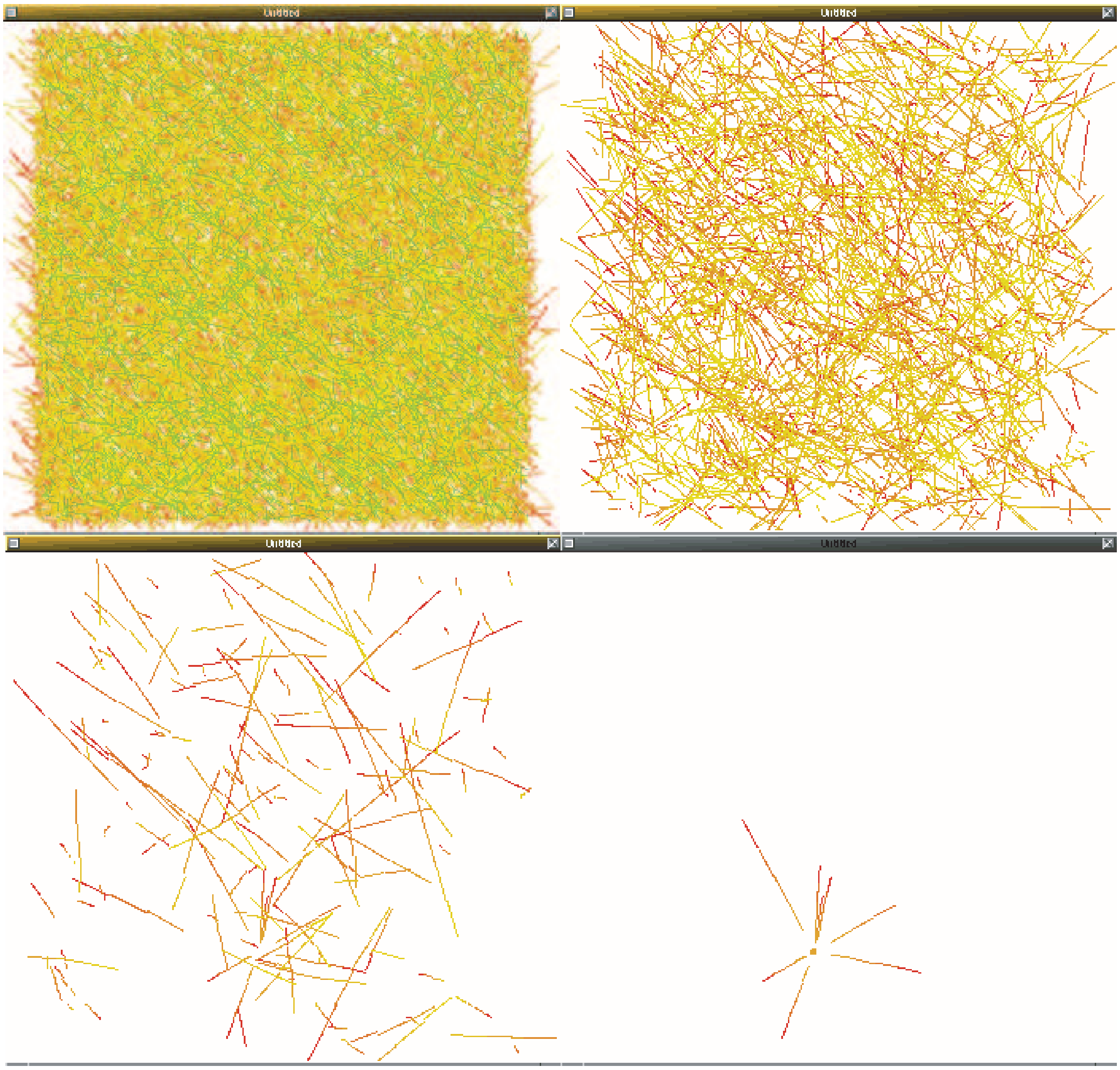

Figure 1.5: Example of data processing by *Net Scan* with DONUT ECC data. The scanned surface (orthogonal to the beam) is 5 $mm \times 5$ mm times eight emulsion plates. Top left: 100000 track segments integrated over the eight plates. Top right: $\sim$ 900 reconstructed tracks stopping in the fiducial volume after rejection of single segments and penetrating tracks. Bottom left: 180 high energy tracks are left. Bottom right: a vertex is found, after requiring at least two tracks converging with an impact parameter of ~ 10 μm.

sandwich of thick material plates (5 mm lead or 1 cm iron) and shielded packages of emulsion plate and X-ray films. The area of the exposures extended up to $100 - 1000$ m^2 for a corresponding weight of $100 - 1000$ ton.

The other way consisted in carrying out detailed observations of particular events with compact ECCs by profiting from the high spatial resolution of the emulsions. An example of this is the discovery of charmed particles in cosmic ray interactions by Niu et al. [34,35] in 1971, three years before the J/Ψ discovery. The schematic layout of that ECC is shown in Fig. 1.6 (right part). In that application the analysing layer was used not only for the energy measurement of electromagnetic showers, but also for the momentum measurement of charged particles by multiple scattering. Until the end of '75, Niu and coworkers also observed the difference in lifetime between charged and neutral charmed particles by analysing the event samples accumulated in several cosmic-ray experiments [36]. This result was confirmed by experiments employing compact ECC detectors at Fermilab [37] [38] and at CERN [39] about five years later.

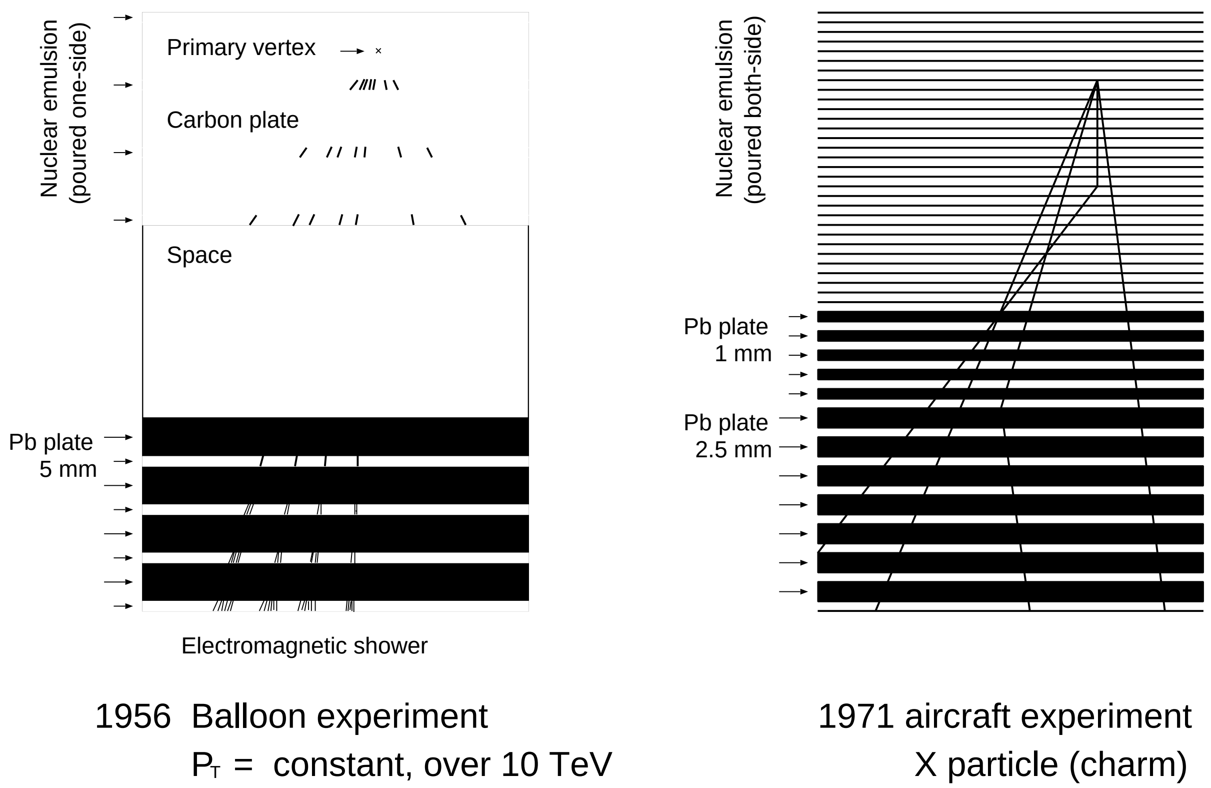

Figure 1.6: ECC detectors used in cosmic ray experiments. The one on the right is the ECC which allowed the discovery of X particles in 1971. Those events had been the first evidence for charm production.

The application of the ECC technique to the OPERA experiment can be considered as a unification of the above two approaches, by using the mass of a mountain-like ECC while keeping the precision of a compact ECC.

1.2.3 Development of automatic scanning systems

An essential ingredient in the development of the ECC technique was a technical study on semi-automatic and automatic emulsion scanning systems. The effort was initiated by Niwa in the late '70s [40]. The motivation was to improve the analysing power needed to increase the statistics of detected charm events (X-particles at that time). The concept of full automatic track recognition, which is the base of the algorithm used in the current systems, was proposed already at the end of the '70s. Unfortunately, the technology was not advanced enough to implement it and the group started the realization of semi-automatic devices by using industrial TV camera tubes and specially developed image digitisers and stage controller (DOMS) with micro-metric accuracy. In Table 1.1 some of those experiments where the semi-automatic scanning systems were used are listed.

Table 1.1: Experiments employing semi-automatic scanning systems.

Experiment	Physics aim	Beam	Emulsion vol. (liters)	Film type	♯ of located events
FNAL E531	Charm $\nu_\mu \to \nu_\tau$	ν	58.6	thick & thin	$\sim 4K$
CERN WA75	Charm, Beauty	350 GeV π^-	80	thick & thin	$\sim 10K$
FNAL E653	Charm, Beauty	800 GeV proton /600 GeV π^-	71	thick & thin	$\sim 50K$
CERN NA34	Charm Production	200 GeV/n ^{16}O	6	thick & thin	$\sim$ 1k
CERN EMU09	Charm Production	200 GeV/n ^{32}S	3	emulsion tape	$\sim 1K$
KEK E176	H-dibaryon /Double Λ Nucleus	1.7 GeV K^-	40	thick & thin	$\sim 1K$

In parallel with the above applications, the effort in the development of full automatic systems continued. In the '80s, an improved version of the prototype Track Selector was devoted to the real physics analysis of the CERN WA75 and FNAL E653 experiments. The system worked satisfactory. However, since the data flow was tuned for semi-automatic systems, the TS speed was not high enough (due to the support

Table 1.2: Steps in the development of the Track Selector systems.

Name	Year	TV Camera	Base clock	Angle recognition	Stage control
TS	1982	ITV tube	10MHz	single processor	independent (DOMS)
TS2	1994	30Hz CCD	10MHz	single processor	independent (DOMS)
NTS	1996	120Hz CCD	20MHz	parallel processor	synchronised system
UTS	1998	120Hz CCD	120MHz	parallel processor with zero suppress.	synchronised system
Super UTS	2000	1kHz CCD parallel out	300MHz	super-parallel proc. with zero suppress.	synchronised continuous driving of X,Y,Z

software) to move the analysis to full automatic mode. The complete application of the automatic system was postponed for about five years until the CHORUS data analysis.

Table 1.2 gives a short summary of the R&D work for the Track Selector. Fig. 1.7 shows the road map presently achieved and future plans. The improvements have been practically following the development of the digital technologies like clock-up, parallel processing and pipeline processing. However, the basic method of recognising tracks has not changed since the original TS. The TS2, NTS and UTS listed in the Table have been (and are being) devoted to the analysis of CHORUS; a real cradle for present and future developments.

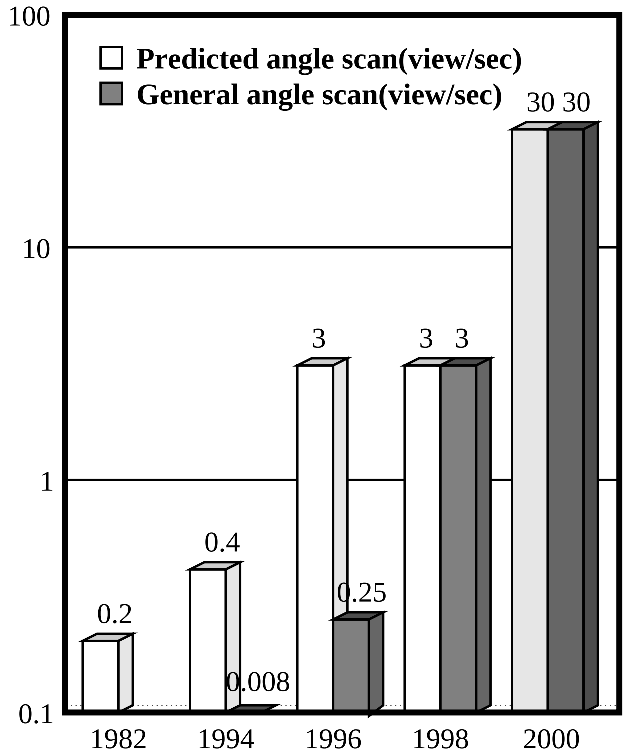

Figure 1.7: The R&D road map of the Track Selector. Note the log vertical scale.

The Super UTS development is specially planned in order to fulfil the scanning power required for OPERA ($\sim$ 1000 cm^2/day). The challenge is to remove the bottleneck of the data taking by employing a fast scanning CCD camera and a continuous movement of the driving unit (stage), exactly like a CD or a Hard Disk. Due to the requirements of the scanning in depth, objective lenses will be driven by piezo oscillators whose movement will be synchronised with the CCD image taking rate. Preliminary tests have been performed and the results are promising.

Automatic scanning systems using different track recognising algorithms and methods are being developed within several other groups like CERN, Münster, Naples, NIKHEF, Rome and Salerno. Some of them will be described in Section 4.1.3.

Chapter 2

The experiment

2.1 Overview

2.1.1 Decay channels

The signal of the occurrence of $\nu_\mu \leftrightarrow \nu_\tau$ oscillations is the CC interaction of τ neutrinos in the detector target: $\nu_\tau N \rightarrow \tau^- X$. The reaction is identified by the detection of the τ lepton in the final state through the decay modes into single charged hadron, muon and electron

$$\tau^- \rightarrow h^- \nu_\tau (n\pi^0), \quad \tau^- \rightarrow \mu^- \nu_\tau \overline{\nu}_\mu, \quad \tau^- \rightarrow e^- \nu_\tau \overline{\nu}_e$$

Despite its distinctive experimental signature, the multi-prong channel of the τ has not been considered for the present estimate of the OPERA sensitivity, due to the unfavourable signal to noise ratio.

The branching ratio (BR) of the three 1-prong decay modes are 49.5%, 17.7% and 17.8% for the hadronic, muonic and electronic channel, respectively. The $c\tau = 87\ \mu m$ leads to an average decay length of the order of one millimetre at CNGS energies.

2.1.2 Cell structures

A long baseline neutrino detector aimed at τ detection can be designed starting from the ECC concept, which combines in a *cell* the high precision tracking capabilities of nuclear emulsion and the large mass achievable by employing metal plates as a target. By piling-up a series of cells in a sandwich-like structure one obtains the so called *brick*, which constitutes a detector element appropriate for the assembly of more massive structures (*walls*).

One can envisage two basic cell arrangements to be used for the identification of the τ decay kink through its direct detection, *i.e.* not only by an impact parameter measurement.

The first one, called *compact cell*, is shown in Fig. 2.1. The cell can be made of a 1 mm thick metal plate (lead, in particular) followed by a thin emulsion sheet (ES). The ES is made up of a pair of emulsion layers 50 μm thick on either side of a 200 μm plastic base. Charged particles give two track segments in each ES. The number of grain hits in 50 μm (15-20) is adequate for reconstruction of track segments by means of automatic scanning devices and ensures redundancy in the measurement of particle trajectories.

If a τ is produced by a ν_τ interacting in a lead plate, it will decay either in the same plate (*short decays*) or in the following plate (*long decays*). For short decays, only an impact parameter measurement is possible. For long decays, instead, the τ is detected by measuring the angle between the charged decay daughter and the τ direction. This kink angle is caused by the invisible neutrino(s) produced in the decay. For its measurement, the directions of the tracks before and after the kink are reconstructed (in space) by means of a pair of ESs, sandwiching the lead plate where the primary vertex occurred (Fig. 2.1). The τ can also decay in one of the ESs downstream of the vertex plate (*e.g.* in its plastic base). Even in this case the kink angle can be reconstructed though with a lower angular resolution.

A source of background to the hadronic τ decays in the lead plates is given by hadron re-interactions. One of the primary hadrons may re-interact in the lead plate giving products not seen by the emulsion, hence simulating the charged 1-prong decay of the τ. Unlike the hadronic channels, both the electron and muon decay modes are characterised by low background, as will be shown in the following. The electron channel benefits from a dense lead/emulsion sandwich structure, which allows the electron identification through its showering in the downstream cells.

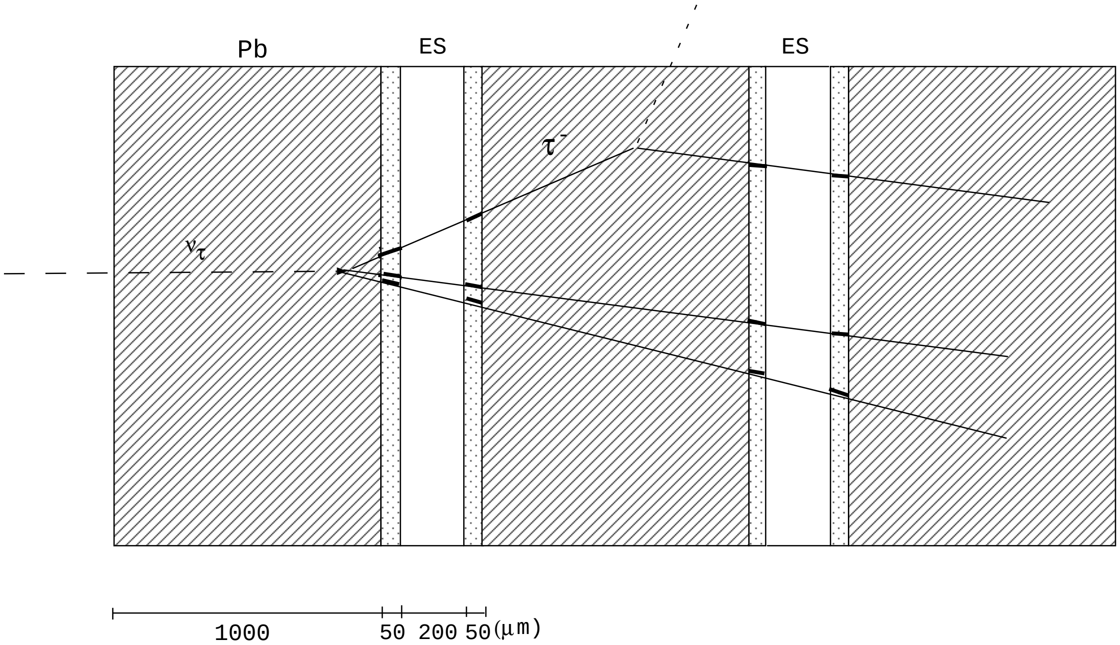

Figure 2.1: Schematic structure of a compact ECC cell employing thin emulsion sheets. The τ decay kink is directly reconstructed in space by using four track segments in the emulsion sheets (ES).

Another possible ECC cell structure (called *spacer cell*) foresees the insertion of a low density spacer between consecutive emulsion sheets [15,16,18] (Fig. 2.2). This gap between the ESs allows direct detection of the τ decay kink, as with the compact cell of Fig. 2.1. In this case, however, the low density of the spacer makes the hadron re-interaction probability negligible. This results in a substantial background reduction for the τ hadronic decay channels, which have the largest branching ratio. The τ decays in the spacer are classified as *gold plated* events, with practically no background. We are presently studying and optimising the cell structure. A possible design foresees a cell composed of a 1 mm thick lead plate followed by an ES, a spacer of 3 mm and another ES, as shown in Fig. 2.2. The spacer consists of very low density material (Rohacell, polystyrene foam, etc.).

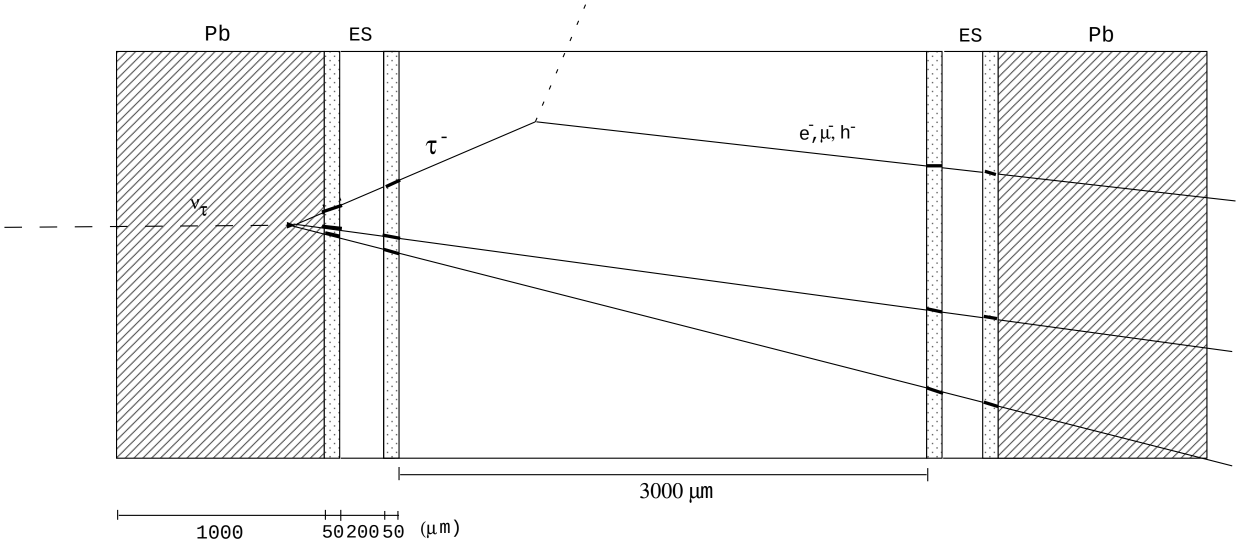

Figure 2.2: Schematic structure of a spacer cell.

The design of the OPERA target can then be based on a lead-emulsion target subdivided into walls made of bricks. Two types of bricks can be used consisting of sequences of *compact* or *spacer* cells. In the following, the features of either approach will be described.

2.1.3 Event finding and reconstruction

Electronic detectors, placed downstream of each emulsion brick wall, are needed to identify the brick where the neutrino interaction took place and to guide the scanning. OPERA at the Gran Sasso is naturally shielded against non penetrating particles and it is exposed to a neutrino beam without halo muons. This leads to a relatively low density of background tracks stored in the emulsion and removes the need for a precise location of individual tracks in the ESs by electronic trackers. Therefore, a moderate space resolution can be tolerated, also imposed by practical considerations on the cost of the electronic detectors.

The main purpose of the electronic detectors is to determine the event shower-axis, hence locating the brick whose emulsion must be scanned. Fig. 2.3 shows for one of the two projections the signals from the trackers in a simulated ν_μ interaction. The brick where the neutrino interacted is visible despite the presence of some back-scattering. The determination of the brick containing the primary vertex from the tracker signals will be discussed in Section 2.4.2.

Once the brick has been identified, it can be removed from the detector and its ESs developed. Scanning could then begin following analysis procedures derived from those developed in the last years for neutrino emulsion experiments.

Starting from the most downstream ES in the brick, track segments are detected and measured in position and angle. This procedure continues in the other ESs until the interaction vertex plate is found. The search

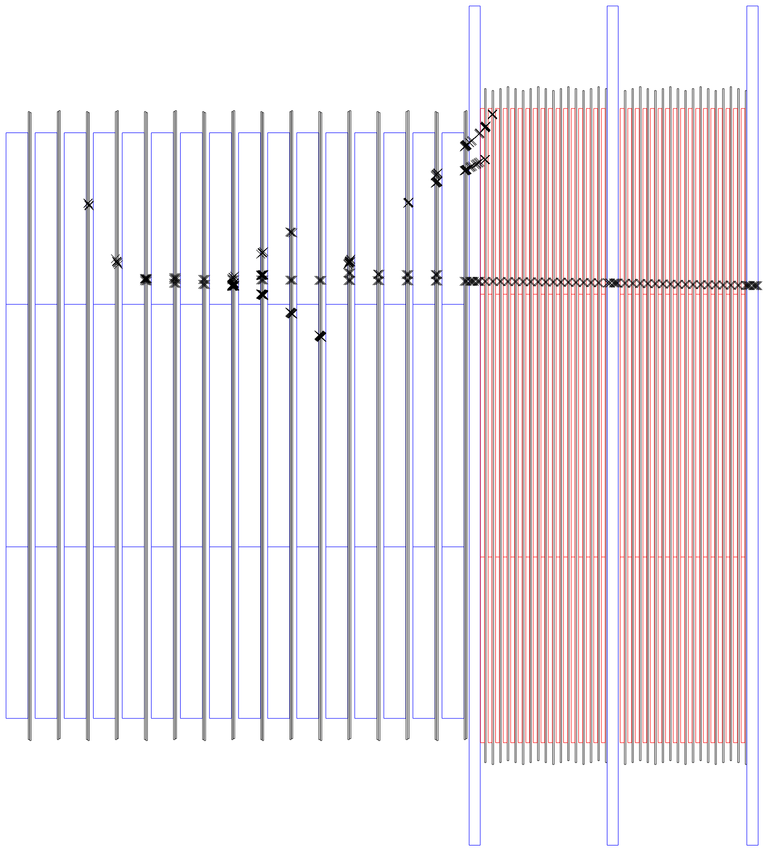

Figure 2.3: Display of a simulated ν_μ CC event (showing some back-scattering). The target section is shown on the left side. Walls of emulsion bricks are interleaved by electronic trackers. Hits in the trackers are shown with a granularity of 2 cm. A muon spectrometer is shown on the right hand side.

for a decay topology is performed with the ESs just downstream of the vertex metal plate. Different scanning methods can be applied, both for vertex finding and kink search. Fig. 2.4 shows the simulation of a ν_μ CC event occurring inside a brick.

An important requirement for the experiment is the determination of the decay transverse momentum of the daughter particle. This is a tool to reject background events. For most of the muons this measurement can be accomplished by means of the muon spectrometers. For electrons the energy is estimated from the shower development. For charged hadrons the momentum is measured by multiple scattering in the ECC sandwich structure.

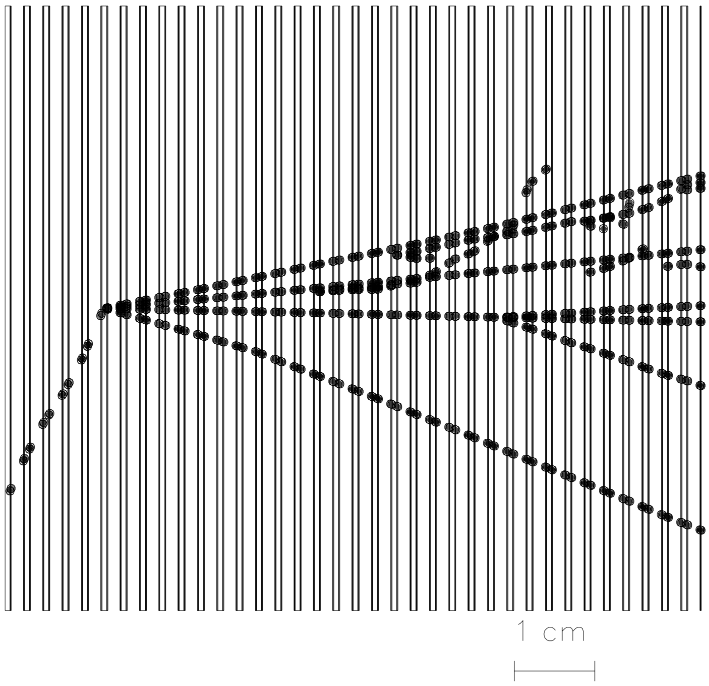

Figure 2.4: Simulated ν_μ CC event in one brick of OPERA. The isolated primary muon track (from bottom-right) points to the vertex.

2.2 Detector requirements and design

2.2.1 General features of the experiment

The main distinctive feature of OPERA is its capability of performing a $\nu_\mu \leftrightarrow \nu_\tau$ oscillation search with low background. A few signal events are therefore meaningful. This extends the discovery potential down to the values of the Δm^2 parameter allowed by the atmospheric neutrino anomaly. Nuclear emulsions are a key ingredient to achieve this result due to the unambiguous detection of the τ decay kink. The solution offered by the ECC technique is appropriate, since it exploits the tracking capabilities of nuclear emulsions, though for a mass much smaller than the total target mass.

The τ decay channel into a muon, despite the relatively low BR and the overwhelming (reducible) background from ν_μ CC interactions, has special features which make it attractive, in particular for a preliminary search. The presence of the penetrating (often isolated) muon track allows an easier event vertex finding. The electronic decay mode can be identified by the characteristic energy loss of the electron inside the dense ECC material (Fig. 2.5). Hadronic modes have the largest BR. Their analysis completes the oscillation search.

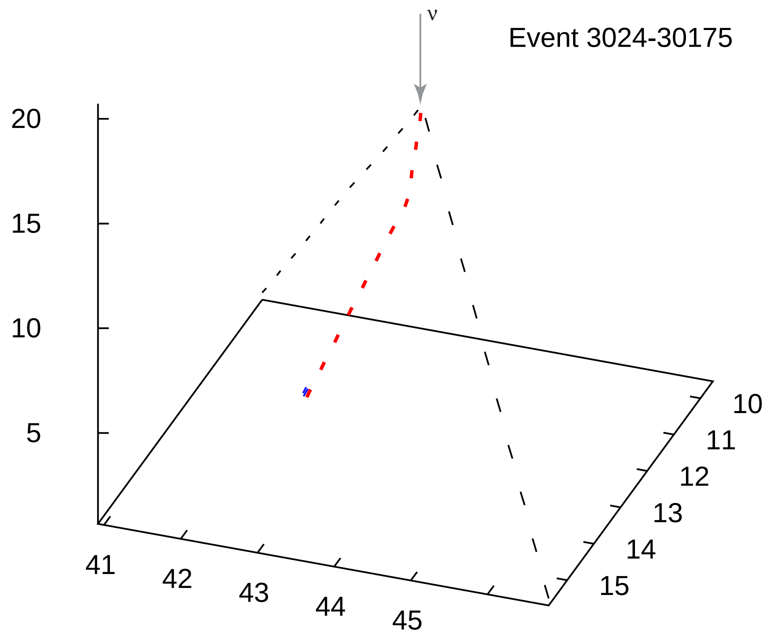

Figure 2.5: DONUT τ candidate event. The three tracks are reconstructed in the ECC. The central track with the kink is interpreted as due to a $\tau \rightarrow e$ decay. The electron starts showering in the downstream ECC plates. The units are millimetres.

Using ECC compact bricks, one would directly profit from the experience already gathered on the ECC technique in *e.g.* the DONUT experiment. A compact design has merits as far as the direct (long decays) kink detection of the muonic and electronic decay channels of the τ is concerned. Moreover, there is an optimal use of the emulsion, since only one ES is needed for each cell.

ECC spacer bricks are expected to offer the appealing feature of the kink detection in a low density material. In particular, hadronic decays inside the spacer have, as shown later, negligible background from primary-hadron re-interactions and decays. However, this is a novel technique which requires further tests and R&D.

The detector design is based on a modular structure. In the present configuration, the total thickness of one brick with (without) spacer is about 14 cm (7.5 cm) along the beam direction. A matrix of adjacent bricks arranged in a plane structure forms a target wall of $\sim 6.5\ m$ transverse dimensions. A wall and its related electronic detector planes constitutes a *module*. A *supermodule* is defined by a target section made of several consecutive modules followed by a muon detection system. The modularity of the target is used to reach the total mass needed to meet the physics goal of the experiment. The structure of the target permits the removal of the *fired* bricks and to analyse their emulsion sheets during the run.

Supermodules can be built with either types of bricks (see next Section). Each supermodule contains a given target mass and thus delivers a given number of signal (and background) events. The global detector will eventually consist of a suitable number of such basic *building blocks*. The types and the number of supermodules will be dictated by the physics objectives, but also by the results of the test programmes underway and by the progress in the understanding of the basic properties of the ECC technique as well as by considerations of cost effectiveness.

2.2.2 The target

The dimensions of the bricks are determined by conflicting requirements. A small brick size favours the optimal use of the emulsions when considering brick removals after interactions. In fact, about 25000 events are expected in the total running period and one brick has to be removed for most of the events. The integrated mass to be taken out has to be small compared to the total target mass. In addition, bricks have to be small and light enough to allow easy handling by automatic machines, *i.e.* quick installation and removal. On the other hand, losses due to edge effects are reduced with larger brick cross section.

Another issue is the brick thickness in units of radiation lengths. It determines the particle identification capabilities when following tracks in consecutive cells and also the momentum measurement by multiple scattering. For instance, the actual thickness of the compact bricks is motivated by the need of electron identification via its electromagnetic showering.

In the present configuration, which is still subject of further optimisation, each brick has dimensions of $15 \times 15\ cm^2$ orthogonal to the beam direction. Compact bricks can consist of 56 cells with a total thickness of about 7 cm (10 X_0) and a weight of about 14.5 kg. Bricks with spacers can contain 30 *cells* with 14 cm thickness (5 X_0) and about 8 kg weight.

Tracks from τ candidate events will have also to be followed in consecutive (and in some cases adjacent) bricks to perform a complete kinematical analysis by measuring and identifying the largest number of particles. This requirement imposes mechanical constraints on the way brick walls are assembled and installed and on their support structures. The distance between consecutive walls has to be minimised ($\sim 5\ cm$, just to permit the insertion of electronic detectors) as well as the transverse distance between bricks in the wall matrix ($\sim 5mm$). The need of connecting events in consecutive bricks is the motivation for further optimisation of the brick dimensions, once experimental information is available on the specific scanning procedure.

The wall support structure has to be of sufficiently low mass in order to reduce the amount of neutrino interactions in the uninstrumented material, thereby avoiding the possible removal and scanning of *empty* bricks.

The operation of the system for brick removal must minimise the number of times a brick is displaced with respect to the neighbouring ones. The spatial correlation of tracks in neighbouring brick is determined on the basis of common hit patterns in different ESs. This correlation can be mantained for any period between relative brick displacements, provided a sufficient number of connecting tracks can be found.

Module and supermodule dimensions are governed by the efficient use of the space in the underground cavern. The beam size is, obviously, not an issue, as its rms value at the Gran Sasso is about 800 m. This would motivate large transverse dimensions of the modules. However, one has then to deal with the requirements of large surface electronic detectors, with the realistic dimensions of the muon spectrometers (iron magnets), with the mechanical design and with the need for sufficient (lateral) space for services and for the handling of bricks.

All the above considerations favour a transverse wall dimensions of about 6.5 m. The shape of the brick wall, $i.e.$ of the way bricks are assembled, could be squared or octagonal in order to match the actual shape of the supermodule muon spectrometer. The number of modules in a supermodule, and hence its longitudinal dimension, is basically determined by the muon acceptance and thus by the maximum realistic size of the spectrometers. This limits the longitudinal length of a target supermodule to about 3.5 m.

According to the above requirements and to the present tentative design, the target structure can be as follows. The octagonal section is assumed as a reference. A supermodule with spacer bricks consists of 18 modules. Each module is made of a plane of electronic detectors and a wall of 1340 bricks: 14 cm thick and $\sim$ 6.3 m side to side. The number of bricks per wall comes from a practical estimate of the dead space between bricks (a few mm), which to some extent depends on the support structure. The space between consecutive brick walls is 5 cm, available for the electronic trackers. This makes the total length of the spacer supermodule about $\sim$ 3.5 m. It comprises 24120 bricks for a total mass of 185 ton. A compact brick supermodule consists of 24 modules. The thickness of the bricks is in this case 7.7 cm and the supermodule length is $\sim$ 3 m. Each supermodule includes 32160 bricks for a mass of 455 ton. Table 2.1 lists the features of the target supermodules. Their schematic layouts are shown in Fig. 2.6.

Table 2.1: Design features of the target supermodules.

Item	Spacer-brick supermodule	Compact-brick supermodule
Dimensions	$\sim 6.3 \times 6.3 \times 3.5\ m^3$	$\sim 6.3 \times 6.3 \times 3\ m^3$
Cell thickness (mm)	4.6	1.3
Number of cells/brick	30	56
Brick x-section (cm^2)	15×15	15×15
Brick thickness (cm)	14.2	7.7
Brick thickness (X_0)	5.3	10
Brick weight (kg)	7.6	14.2
Module thickness (cm)	19.2	12.7
Bricks/wall	1340	1340
Number of modules/superm.	18	24
Number of bricks/superm.	24120	32160
ES surface/supermodule (m^2)	32500	40500
Supermodule weight (ton)	185	455

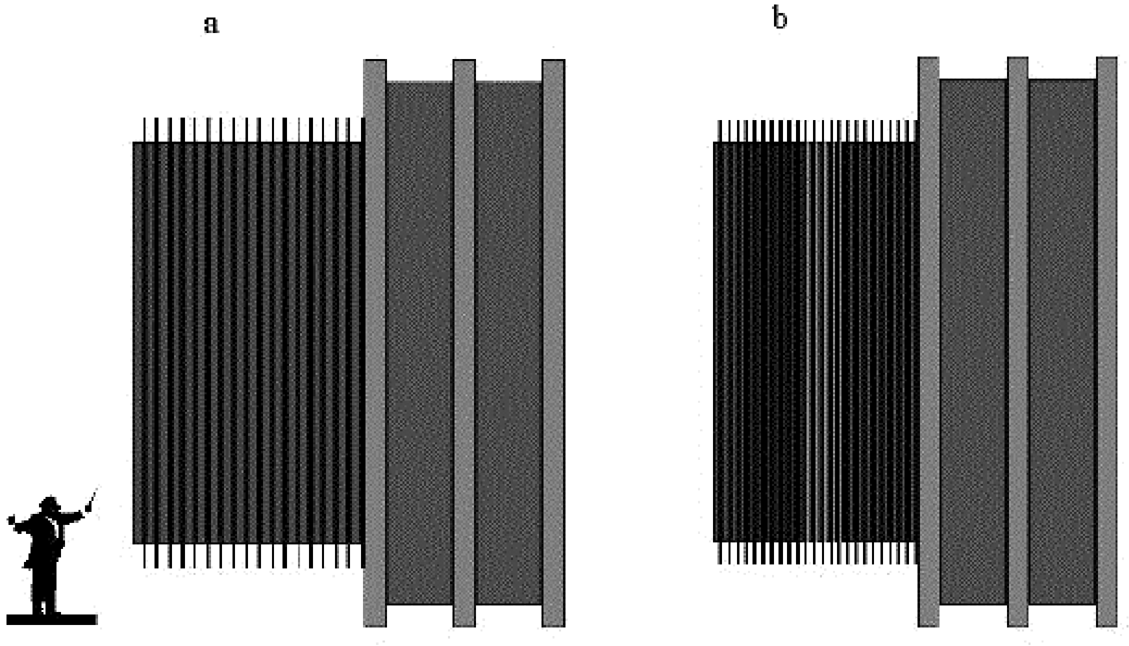

Figure 2.6: Side view of the two types of supermodules: a) spacer and b) compact.

2.2.3 Electronic detectors in the target modules

The electronic detectors of the target modules are arranged in planes between brick walls. They measure the transverse coordinates of tracks, locate the interaction vertex brick and contribute to the hadronic energy measurement.

In order to assess the physics requirements, we have simulated CNGS beam interactions with different brick structures. This allowed to study the behaviour of the secondary particles exiting the vertex brick. Fig. 2.7 shows the charged particle multiplicity in a two tracker planes, downstream of the vertex brick and of the following brick wall. This is shown both for spacer and compact bricks. Particles with energy above 10 MeV enter the plots. One can see that due the thickness of the compact brick (10 X_0) the charged multiplicity decreases significantly already after the second wall.

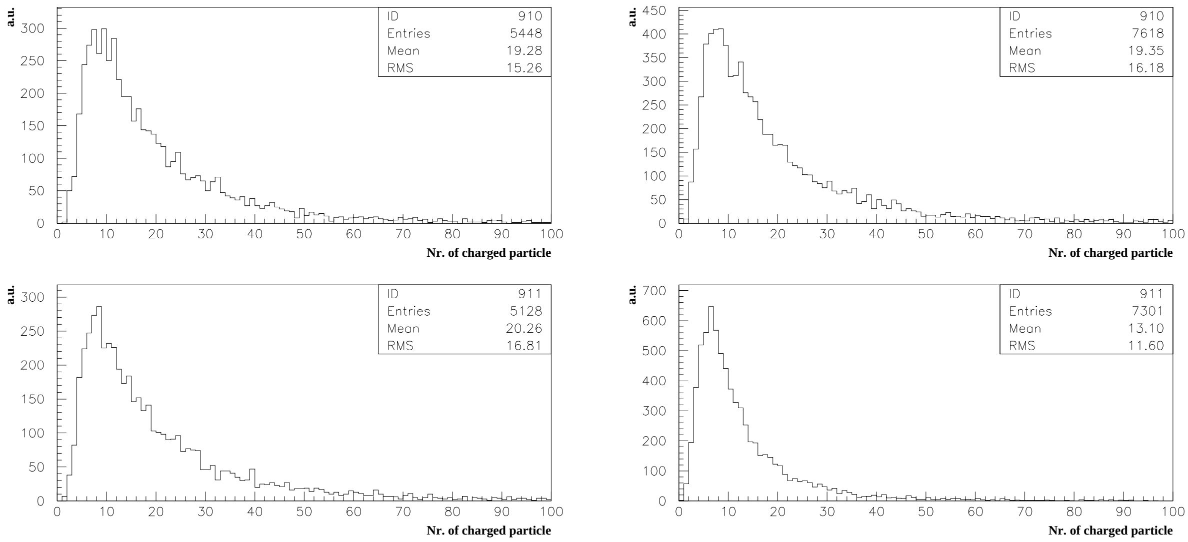

Figure 2.7: Charged particle multiplicity in tracker planes after the vertex brick (top) and after the following brick wall (bottom). Left (right) plots: spacer (compact) bricks.

In Fig. 2.8 the distribution of the width of the shower at the tracker plane downstream of the vertex brick is shown for both types of bricks. The width is defined as the distance between the two most distant particles in the plane. The Figure also shows the distribution of the difference between the vertex position and the shower axis as determined by the centre of gravity of the energy release in the tracker plane. The resolution is about 3 cm for spacer and 2 cm for compact bricks by using the signals from one tracker plane. For the above calculations a plane of scintillator strips two centimetres wide and one centimetre thick has been taken.

In Fig. 2.9, the rms value for the longitudinal vertex position prediction is plotted in the case of 1 cm, 5 cm and 9 cm wide scintillator strips with analog or digital readout for both compact and spacer bricks.

The electronic detectors have to provide adequate space resolution, high efficiency and long term reliability. The large total area (about 4000 m^2 for each coordinate measurement) restricts the choice to cost

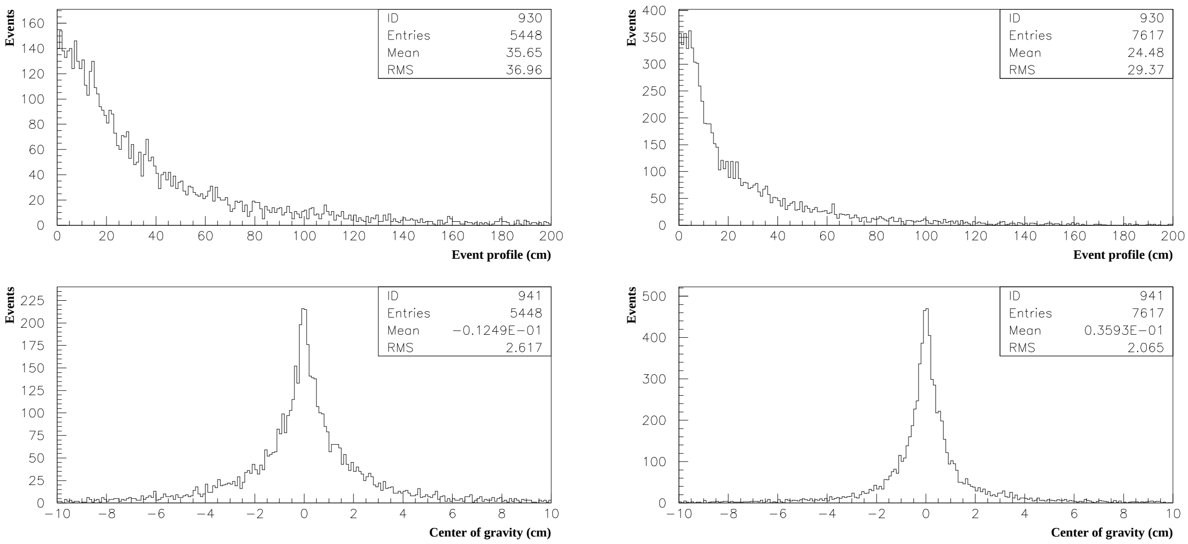

Figure 2.8: Top plots: shower width distribution at the first tracker plane; bottom plots: shower centre of gravity resolution. Left (right) plots: spacer (compact) bricks.

effective and mature technologies previously used in applications of a similar scale and suitable for industrial production. Flammable gases and polluting materials also limit the possible detector options given the strict rules at the Gran Sasso Laboratory.

The baseline option for the OPERA target section is based on scintillator strips read out by wave length shifter (WLS) fibres coupled to photo-detectors. Another detector option is represented by liquid scintillator tubes.

2.2.4 Muon detection

A muon spectrometer constitutes the downstream part of each supermodule. Its purpose is to identify muons with high efficiency, which is of basic importance in order to reduce the charm background, and to measure the sign of the charge. One will see later that the number of single and associated charm background events produced in ν_μ CC interactions is proportional to the primary muon identification inefficiency $(1-\varepsilon_\mu^{charm})$. The design goal is to obtain an overall muon identification efficiency of $\sim$ 95%. Note that going from an ε_μ^{charm} of 90% to 95% reduces the charm background by 50%.

The background given by charmed mesons $C^\pm$ produced in CC and NC ν_μ interactions and decaying into muons is further reduced by the measurement of the muon charge. This reduction is proportional to the charge determination inefficiency $(1-\varepsilon_{ch}^{C^\pm})$ of the decay muon. The measurement of the charge is practically impossible for the other decay modes.

For muonic τ decays, a measurement of the muon momentum is also required to perform the kinematical analysis of the candidate events, together with the momentum measurement which can be performed by measuring the multiple scattering with the emulsions.

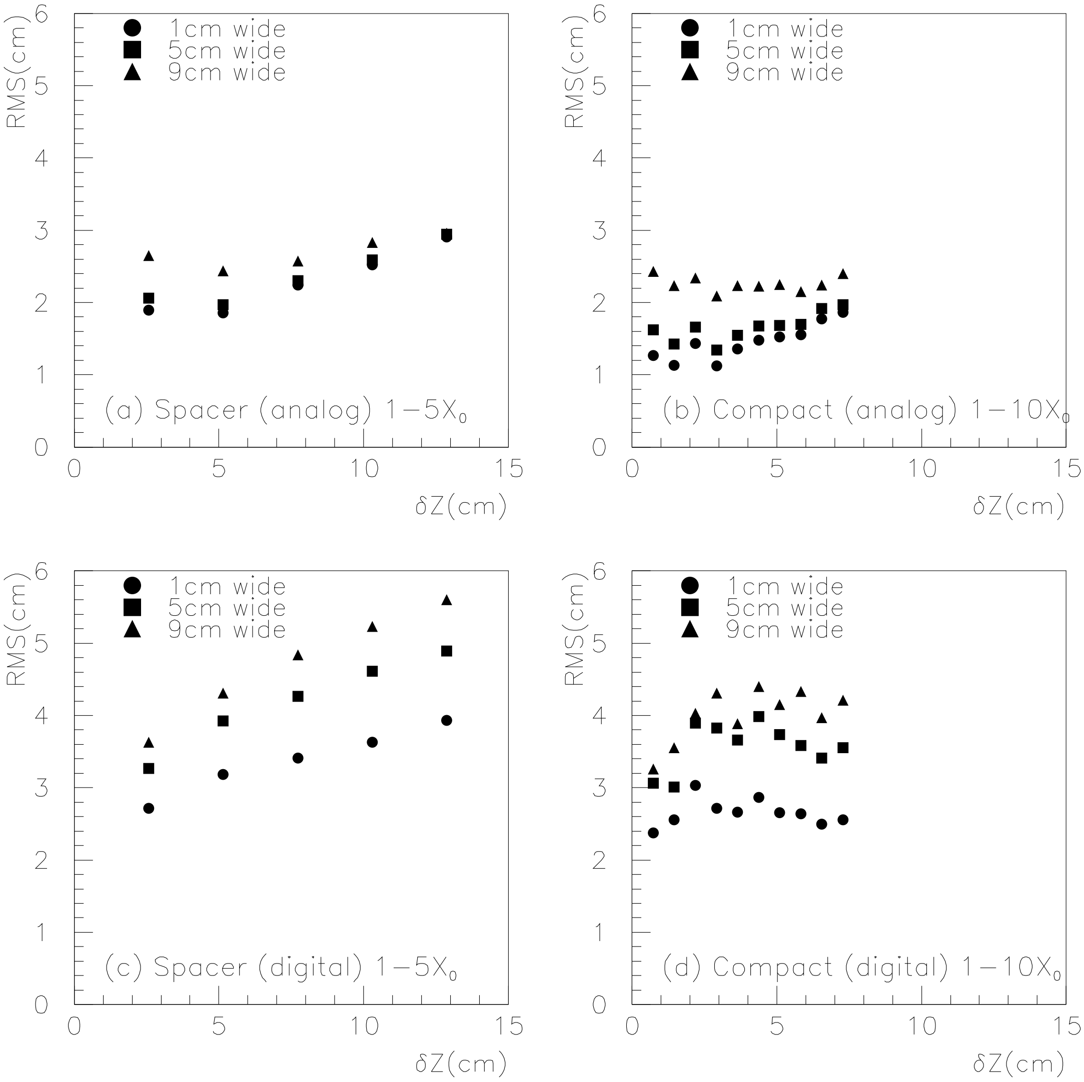

Figure 2.9: Accuracy on the estimate of the longitudinal vertex position in a brick by the electronic trackers. δZ is the distance from the vertex to the downstream tracker plane. (a) spacer brick (analog readout); (b) compact brick (analog readout); (c) spacer brick (digital readout); (d) compact brick (digital readout).

Finally, through the measurement of the muon charge and momentum from ν_μ CC interactions, essential information can be gained on the beam, like its total flux, its energy spectrum and its $\overline{\nu}_\mu$ contamination.

In the baseline option each spectrometer is made of three high resolution trackers interleaved by two toroidal magnets made of octagonal steel plates. The total steel thickness ($2 \times 51\ cm$) together with the magnitude of the magnetic flux density ($1.5\ T$ averaged over the transverse area of the magnet) and the space resolution of the trackers ($\sigma_t \leq 1\ mm$) provide the required momentum resolution of at least 30% in the relevant kinematical domain. The resolution is given by

$$(\frac{\Delta p}{p})^2 = 0.2^2 + (0.01 \times \sigma_t[mm] \times p[GeV/c])^2$$

where the constant term is the multiple scattering contribution. The fraction of wrong sign measurements at the average μ^- momentum of $16\ GeV/c$ in the quasi-elastic channel is 0.17%. It is 0.06% at $9\ GeV/c$, the average momentum of the μ^- from τ^- decay.

The transverse size of the magnets is $7.5\ m$ from edge to edge of the octagon. It complies with the width and length of the target supermodule and with the high geometrical acceptance required for muon identification. The energy loss of muons traversing the full length of the target is $0.7\ GeV$ for a spacer supermodule and $1.7\ GeV$ for a compact one. The energy loss of muons in the spectrometer is $0.6\ GeV$. The muons which cross the spectrometer or stop in it have an identification probability of almost 100%.

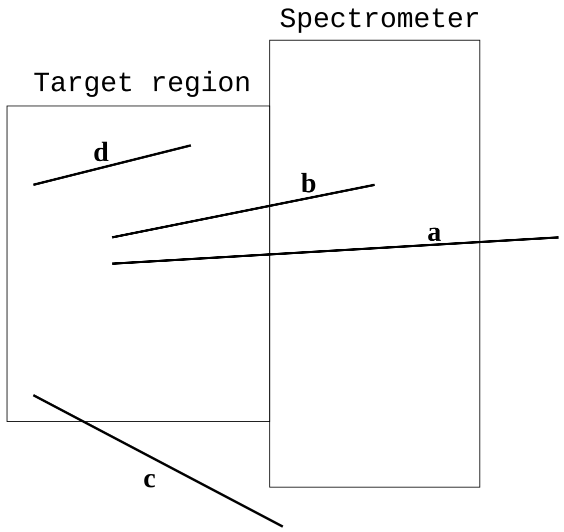

Figure 2.10: Different muon topologies.

Muon identification is performed in OPERA through the target electronic trackers, the muon spectrometers and the emulsions themselves. Possible muon topologies are shown schematically in Fig. 2.10. Averaging over the full spacer (compact) supermodule 87.5% (82.5%) of the primary muons from charm events cross the spectrometer (a) and 8.5% (9.5%) stop inside it (b). Out of the other muons, 1% (1%) leave the detector from the side (c) and 3% (7%) stop in the target before reaching the spectrometer (d). In Fig. 2.11 (Fig. 2.12) the muon acceptance, subdivided in the above four categories, is plotted as a function of the number of modules per supermodules, for spacer (compact) supermodules.

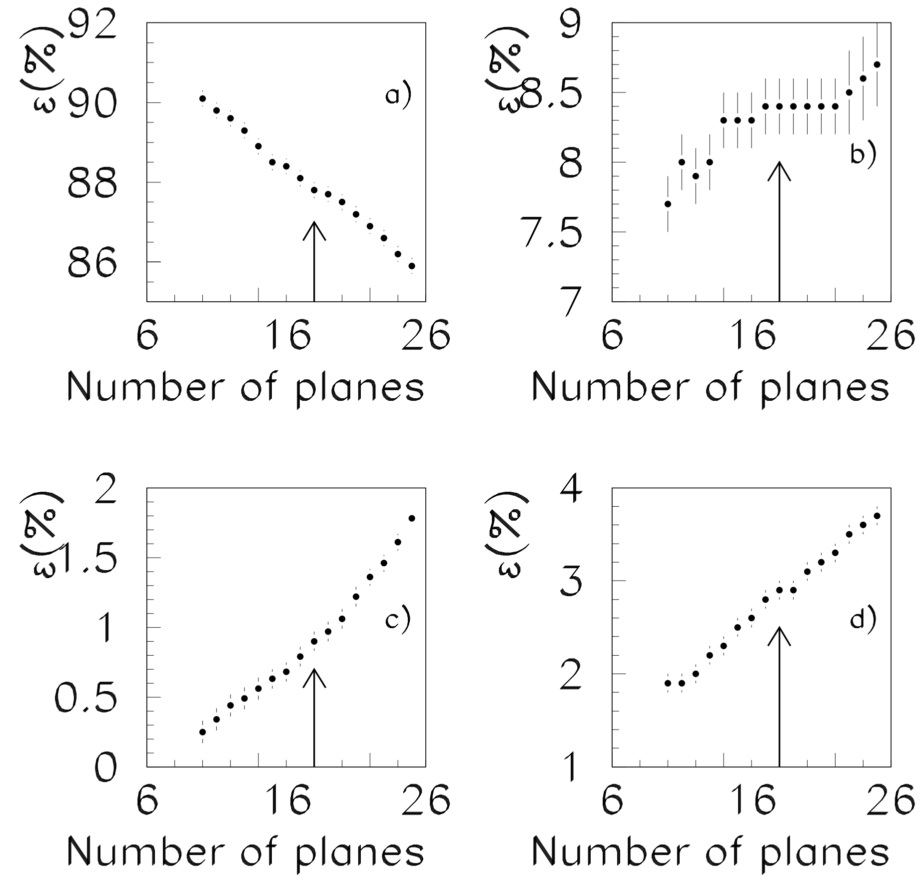

Figure 2.11: Muon acceptance for spacer supermodules as a function of the number of modules per supermodule. a) passing the spectrometer; b) stopping in the spectrometer; c) exiting the target sideways; d) stopping in the target. The arrow indicates the number of modules in the present design.

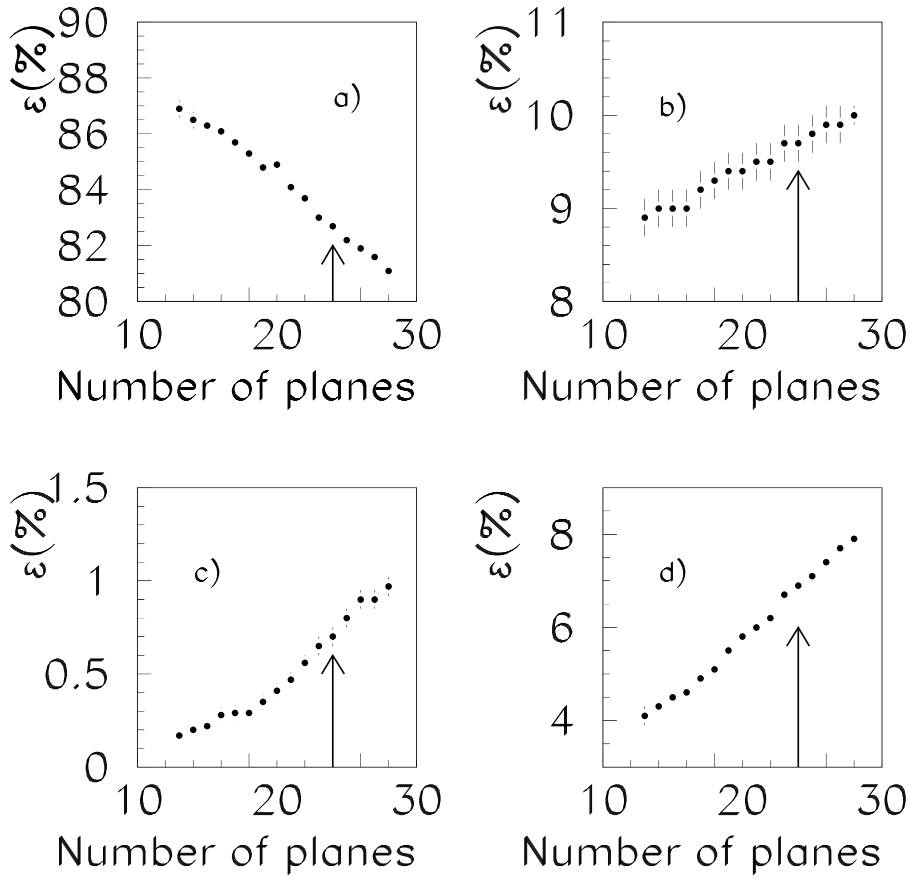

Figure 2.12: Muon acceptance for compact supermodules as a function of the number of modules per supermodule. a) passing the spectrometer; b) stopping in the spectrometer; c) exiting the target sideways; d) stopping in the target. The arrow indicates the number of modules in the present design.

The magnets can be further instrumented with scintillator planes. Their purpose is to provide

- a measurement of the tail of the hadronic energy leaking from the target with a resolution of $\sim 80\%/\sqrt{E}$;
- a measurement by range of the energy of the muons which are too slow ($E \leq 1\ GeV$) to traverse the two magnets, with a resolution of $\sim 5\%$;
- a coarse tracking inside the magnet that facilitates the track matching between trackers;
- a possible measurement of the NC/CC ratio for events occurring in the spectrometer steel if used as a target.

2.3 Neutrino beam and interactions

The original CNGS *reference* neutrino beam from the CERN SPS to the Gran Sasso is described in [14]. A further optimisation of the ν_τ interaction yield was proposed in [41]. It contributed to the new CNGS beam design developed by the CERN/INFN Technical Committee [42], to which we will refer in order to evaluate the OPERA performance.

The nominal CNGS beam features with the new design are summarised in Table 2.2. The quoted numbers of neutrino interactions include deep-inelastics (DIS), quasi-elastics (QE) and resonances (RES). The expected number of interacting ν_τ for $\sin^2 2\theta = 1$ and three values of Δm^2 is shown in Table 2.3. In Fig. 2.13 the energy spectrum of the CNGS beam is presented, together with the spectrum of the oscillating ν_τ.

Table 2.2: Nominal performance of the updated CNGS reference beam [42].

pot/year	4.5×10^{19}
ν_μ (m^{-2}/pot)	7.45×10^{-9}
ν_μ CC events/pot/kton	5.44×10^{-17}
$\langle E \rangle_{\nu_\mu}$ (GeV)	17
ν_e/ν_μ	0.8 %
$\overline{\nu}_\mu/\nu_\mu$	2.0 %
$\overline{\nu}_e/\nu_\mu$	0.05 %

Table 2.3: Number of ν_τ CC interactions at the Gran Sasso per *kton* and per *year*. The expectation for $\Delta m^2 = 10^{-3}\ eV^2$ and $\sin^2(2\theta) = 1$ is given [42], together with the corresponding numbers at higher Δm^2.

Δm^2	ν_τ interactions/kton/year
$1 \times 10^{-3}\,\mathrm{eV}^2$	2.48
$3.5 \times 10^{-3}\,\mathrm{eV}^2$	~ 30
$5 \times 10^{-3}\,\mathrm{eV}^2$	~ 60

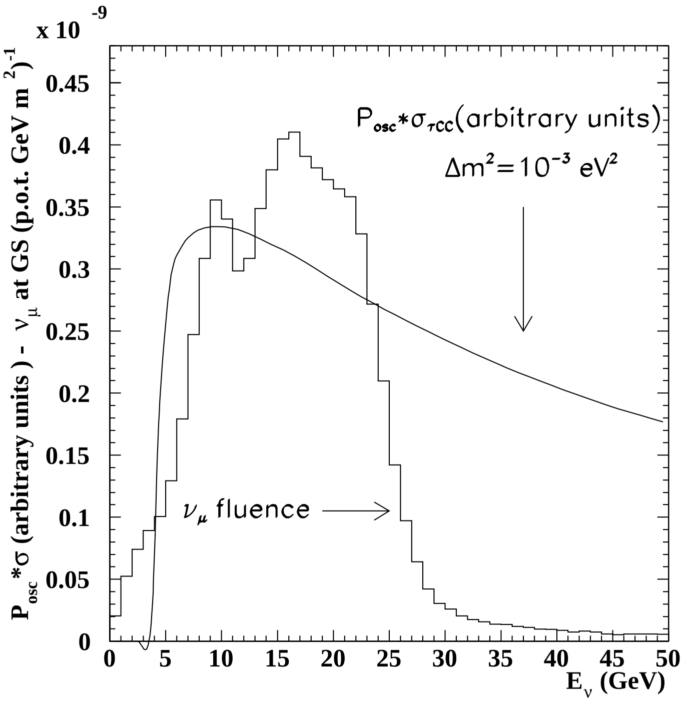

Figure 2.13: CNGS ν_μ spectrum. Superimposed is the spectrum of the oscillating ν_τ for $\Delta m^2 = 10^{-3}\ eV^2$.

2.4 Detection efficiency for the τ decay

The τ detection efficiency of OPERA has been estimated by simulations which take into account the experience gathered with past neutrino experiments and by test measurement results. The efficiency depends on the actual type of bricks (supermodules). The efficiency is also dependent on the kinematical features of the events and therefore of the oscillation parameters. In the following, the estimates are given for $\Delta m^2 = 3.5 \times 10^{-3}\ eV^2$ and full mixing.

2.4.1 Simulation and event reconstruction

A GEANT (version 3.21) simulation of the full supermodules has been performed, taking into account geometry and materials. All primary tracks from a neutrino interaction event in the target are generated according to the JETTA package [43] and traced through the entire apparatus taking into account the relevant physical processes. Secondaries down to 1 MeV kinetic energy for electrons and gammas and 10 MeV for all other particles are also traced. Monte Carlo information about each particle crossing the active detectors is recorded, to provide data input for event reconstruction programs. This information, classified as *hits*, includes detector identifier, crossing position, energy deposition, particle kinematics, etc.

In addition, a detailed simulation of the bricks has been performed, to study the event topology in the vertex region, to estimate the physical background and to study brick material and configurations. A standard GEANT 3.21 software requiring high performance in terms of tracking step length, position resolution and machine precision has been used for this purpose. The simulation of the emulsion composition has already succesfully been tested for CHORUS.

Track segments on both sides of the ES are reconstructed from simulated data. The two high resolution space points measured at the base define the high precision (space) segments used for tracking. A smearing has been introduced on the above two points in order to simulate an angular resolution of 5 $mrad$ in each projection.

A simple framework for event file processing and reconstruction has been developed and used to analyse Monte Carlo data. For that a modular code was used. In this way, the role of the framework is essentially to control I/O of data and provide hooks for reconstruction submodules in the various processing steps (run/event initialisation, data reading, processing, termination). Specific unpacking routines to handle data input in packed format are part of the framework. Outside the framework, a collection of routines for general purpose utilities and basic reconstruction has been developed.

The task of the basic reconstruction routines is to provide an interface between the data input from the simulations and the main reconstruction and analysis submodules. As discussed above, reconstruction of track segments from grains in the emulsions is performed at the level of the simulation code, assuming unitary track finding efficiency for each emulsion plate. Submodules for track reconstruction in different subsystems (bricks, electronic detectors, spectrometers) have been developed. Their output is accessible from other modules.

The software of the simulations programs is based on the Fortran 77 code with support of standard scientific libraries developed at CERN and has been written to run on AIX and Linux platforms. The ZEBRA package has been used for memory management and data storage. A long term approach using modern OO-models under development for HEP simulation has been tested to run on different platforms.

2.4.2 Brick finding efficiency

The brick finding efficiency in OPERA is determined by electronic trackers. They perform the measurement of the axis of the shower induced by the neutrino interaction and therefore the identification of the brick where the interaction occurred. The reconstruction of individual particles can contribute to the event location.

Sources of inefficiencies are, in the longitudinal direction, back-scattering at the event vertex and, in the transverse direction, finite resolution effects at the boundary between adjacent bricks and interactions in the material of the support frames. However, an initial misidentification of the right brick can be recovered later by scanning another brick.

Back-scattering may lead to wrong identification of the wall where the interaction occurred. Monte Carlo simulations show that the wall is chosen correctly in about 85% of the τ decay events. This result can be improved upon up to 95% by removing in certain cases an additional downstream brick.

Tests have been performed to determine the accuracy of the determination of the fired brick transverse with respect to the beam direction (Section 5.2). The results obtained with a prototype scintillator electronic tracker indicate that the correct brick can be located in 85% of the cases. In these tests a mixture of muon and pion interactions has been used. In the real experiment the above performance will be improved by more refined analyses based on the observation of the full event. In addition, in some of the cases neighbouring bricks could be removed. This way one expects to reach an efficiency of 95%.

The above figures lead to a global brick detection efficiency $\varepsilon_{br} \sim 90\%$.

2.4.3 Geometrical efficiency

Tracks can be reconstructed up to very close to the ES edge. Here, we assume $3\ mm$ (~ 25 microscope views). For bricks with $15 \times 15\ cm^2$ cross section this produces a 8% loss in the effective emulsion surface. Forthcoming tests will investigate how to minimise this loss.

For candidate events, one may need to follow the τ daughter into other bricks for particle identification and momentum measurement. For this purpose, the direction of the particle has to be measured so implying that it has to be traced in the vertex brick for a few cells downstream. This implies a small loss in geometrical acceptance.

The effect of the dead space for the brick-to-brick event connection has been evaluated. According to present estimates this leads to an inefficiency of $5 - 10\%$. This value is a function of several parameters and will be the subject of forthcoming studies and tests aimed at its minimisation.

Events occurring in the last wall of a supermodule or at the outer edges have a lower efficiency for particle identification decay p_t measurement. This may lead to an additional volume loss at the $1 - 2\%$ level.

The various contributions result in an overall $\varepsilon_{geom} \sim 80\%$.

2.4.4 Vertex finding efficiency

Once the brick where the neutrino interacted has been identified, scanning proceeds according to the analysis methods discussed in Sections 1.2 and 4.1. The relatively low background of tracks stored in the ESs, though imposing care for their alignment, facilitates the procedure of vertex finding.

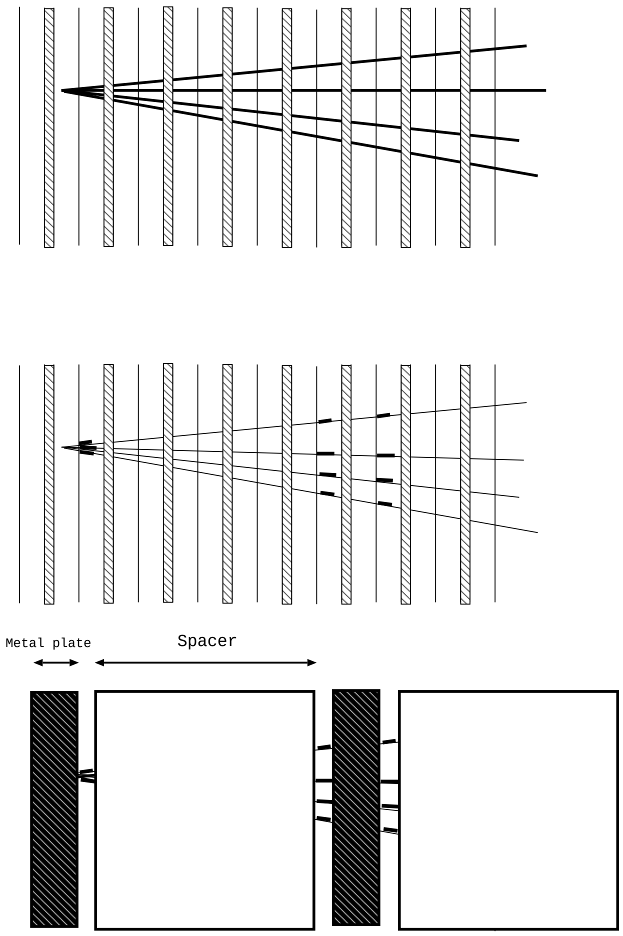

Figure 2.14: The CHORUS emulsion target is compared with the OPERA cell structure with spacers. Top: one event in the CHORUS target. Middle: automatic microscopes measure 100 μm segments. Bottom: by looking only at some of the measured segments one can mimic the OPERA cell.

One can estimate the vertex finding efficiency ε_{vert} for bricks with or without spacer either by Monte Carlo simulations or by simulations using real data, *e.g.* from CHORUS.

In Fig. 2.14, we show how track segments measured in the CHORUS emulsions for identified neutrino vertices allow to estimate the vertex finding efficiency in OPERA. The result of such analysis are shown in Fig 2.15. General scanning is applied to the interface emulsion sheets attached to the most downstream emulsion plate in a CHORUS target module [17]. All segments within a wide angular acceptance cone of 800 $mrad$ are measured. About 2000 segments are found in the test measurement (top left plot). Note that this corresponds to a track density several orders of magnitude higher than in OPERA. These segments are then extrapolated into the emulsion layers placed at a distance of 3 mm (equivalent to an OPERA spacer) then into another layer 1 mm further upstream (equivalent to a lead plate) and so on (top right plot). Progressing upstream, all matching tracks are stored (bottom left plot) and out of them one is a multi track vertex (bottom right, expanded view).

In order to obtain a statistically significant result with the above method, general scanning of large areas is needed. With the presently routinely available system (New Track Selector) this would require about 10 $hours/cm^2$ which is excessive. To simplify the procedure a selected set of data was used. We used a sample of about 100 already located multi-track events (CC and NC) from CHORUS, for which the *prediction* scanning of the special sheet had been performed. For each predicted track, 700×700 μm^2 are scanned with an angular acceptance of 30 $mrad$ retaining all measured track segments. The segments are then extrapolated to the upstream emulsion layers according to the *jumping* scheme previously described. A vertex finding efficiency of about 85% (90%) was found for spacer (compact) bricks despite the adverse conditions of high track density.

Another method which makes use of the CHORUS data can be investigated. Given the target mass and the total number of neutrino interactions, about three neutrino event vertices are expected per cubic centimetre of the CHORUS emulsions. A volume scanning of about 10 cm^3 CHORUS emulsions has started with the state of the art UTS scanning system available in Nagoya. The aim is to identify about 30 primary vertices with a *minimum bias* general scanning.

All the results given above can be compared with those experimentally obtained with DONUT ECC data, which seem to indicate a somewhat lower efficiency. However, one should note that DONUT has much higher track density than expected in OPERA.

Based on all these considerations, for the time being we assume $\varepsilon_{vert} = 80\%$ on average for all τ decay channels.

We realise that vertex finding efficiency is an important design parameter for the experiment. For this reason a dedicated test measurement with OPERA bricks exposed to a pion beam is underway. Results are expected soon.

2.4.5 Muon identification

As already discussed in Section 2.2, muon identification is an important issue for background reduction. In fact, single charm production only occurs in charged current neutrino interactions. Therefore, if the primary muon is identified, the charm decay cannot be mistaken as a τ.

The muon identification algorithms we are developing combine the 3D track information from the ES with the signals from the downstream electronic trackers. Their main goals are: identification of the muon

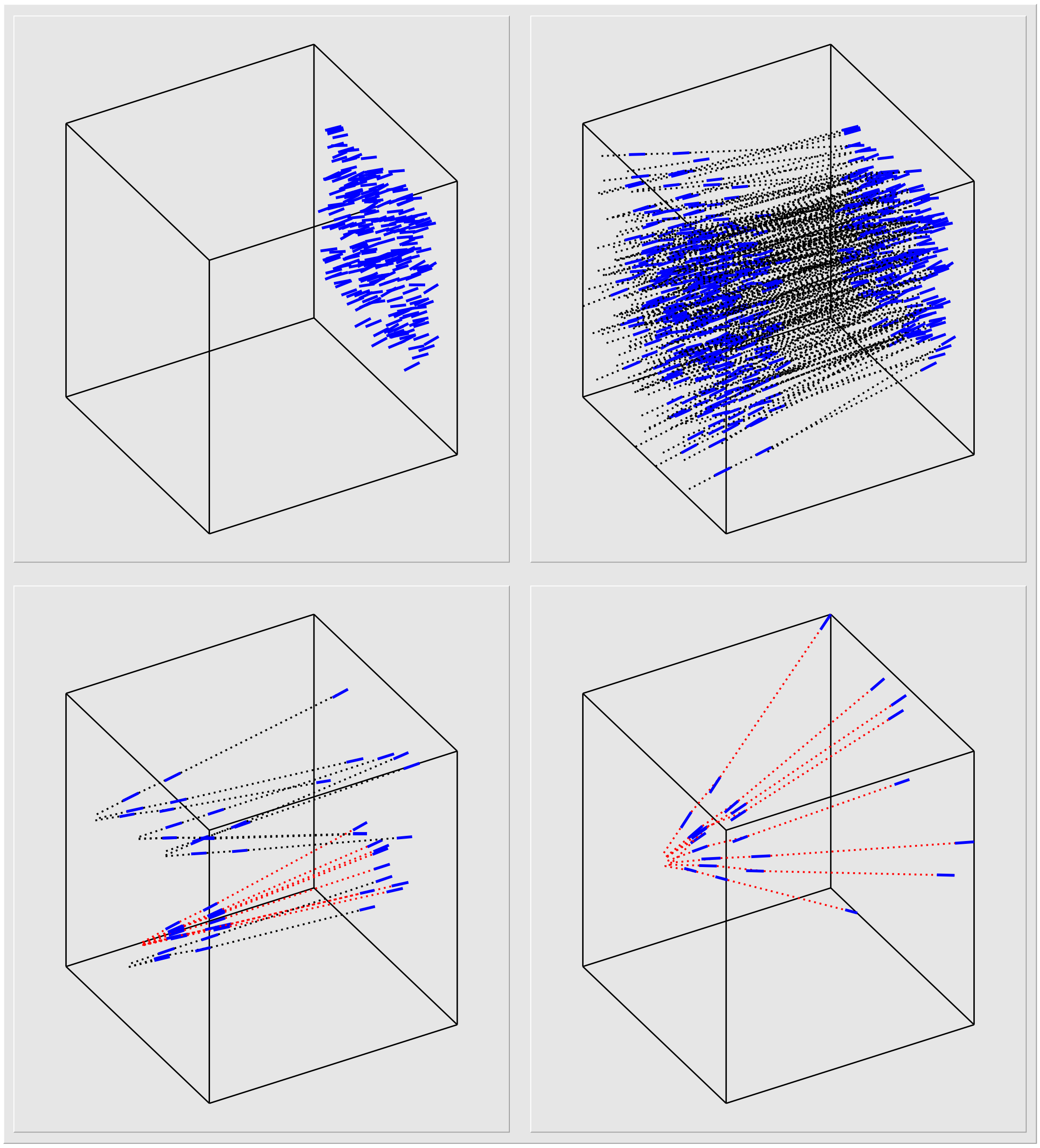

Figure 2.15: CHORUS data allow to simulate the vertex finding procedure in OPERA (see the text for the explanation).

track produced either at the primary (background) or at the decay vertex (signal); matching of the muon track identified in the electronic trackers with the one measured in the emulsions.

The muon identification efficiency not only affects the background reduction, but it is also important to select $\tau \rightarrow \mu$ decays in the compact bricks. As we will discuss in Section 2.4.7, only leptonic decays of the τ are searched for in compact bricks. Therefore an inefficiency in the muon identification implies loosing τ decay events. In contrast, for spacer bricks such an inefficiency just leads to classify a $\tau \rightarrow \mu$ decay as a hadronic or electronic decay.

In addition to its identification, it is also important to match the muon either to the primary vertex (background ν_μ CC interaction) or to the decay vertex (possible $\tau \rightarrow \mu$ decay). In order to keep the background as small as possible, one has to reject events containing a track identified as a muon but not matched either to the primary or to the decay vertex. This rejection reduces the charm background by a factor $(1 - \varepsilon_\mu^{charm})$ at the expense of some efficiency for the $\tau \rightarrow \mu$ channel.

The combined inefficiency of the muon identification and of its matching at the primary (decay) vertex is expressed as $(1 - \varepsilon_\mu)$. Given the features presented in Section 2.2.4, the results of the analysis on muons from neutrino events indicate that a fraction $(1 - \varepsilon_\mu) = 15\%$ (20%) of the $\tau \rightarrow \mu$ events are lost in the case of the spacer (compact) supermodule configuration. For what concern charm rejection efficiency $\varepsilon_\mu^{charm} = 95\%$.

In order to increase ε_μ for low momentum muons one can exploit a method based on momentum-range consistency. The momentum of a $\tau \rightarrow \mu$ candidate can be determined by measuring the multiple scattering in the ECC cells and compared with the one estimated by range in the supermodule. This possibility is presently under study.

2.4.6 Detection efficiency for spacer bricks

Some of the factors which contribute to the detection efficiency are independent of the τ decay channel. A τ produced in ν_τ CC interactions and decaying outside the vertex plate is identified through a direct kink detection. Given the CNGS beam features and the τ kinematics, for $\Delta m^2 = 3.5 \times 10^{-3}\ eV^2$ the probability ε_{long} for the τ to exit the vertex plate is 45%. The distribution of the longitudinal τ decay point in the OPERA elementary cell with spacer is shown in Fig. 2.16. One can see from the Figure that the spacer itself ($3\ mm$) collects $\sim 25\%$ of the τ decays. Its thickness meets the requirements of commercial availability and mechanical properties. A thinner spacer (*i.e.* $2.5\ mm$) would reduce the number of detected kinks by $\sim 5\%$. A thinner metal plate would give a higher efficiency, but also fewer interactions.

ε_{long} consists of two terms: $\varepsilon_{long}(base)$, which gives the probability for the τ to decay inside the first ES plastic base, and $\varepsilon_{long}(spacer)$, the probability for a decay in the spacer or in one of the two adjacent emulsion layers (in which case the kink can be measured equally well). The above distinction is required since decays in the base (see Fig. 2.17) and in the spacer are characterised by a different angular resolution. In Fig. 2.18 $\varepsilon_{long}(base)$ (open circles) and $\varepsilon_{long}(spacer)$ (black circles) are shown as a function of the neutrino energy. Taking into account the ν_τ spectrum the respective values are $\varepsilon_{long}(base) = 12\%$ and $\varepsilon_{long}(spacer) = 28\%$.

An additional factor entering into the detection efficiency is given by the rejection of small-angle and very large-angle kinks. The upper cut ($> 500\ mrad$) is motivated by considerations related to the scanning efficiency of the automatic microscopes, as shown in Fig. 1.2 for CHORUS data. The loss of signal due to this cut is about 5%. The lower cut is due to the angular resolution in the measurement of the kink angle in

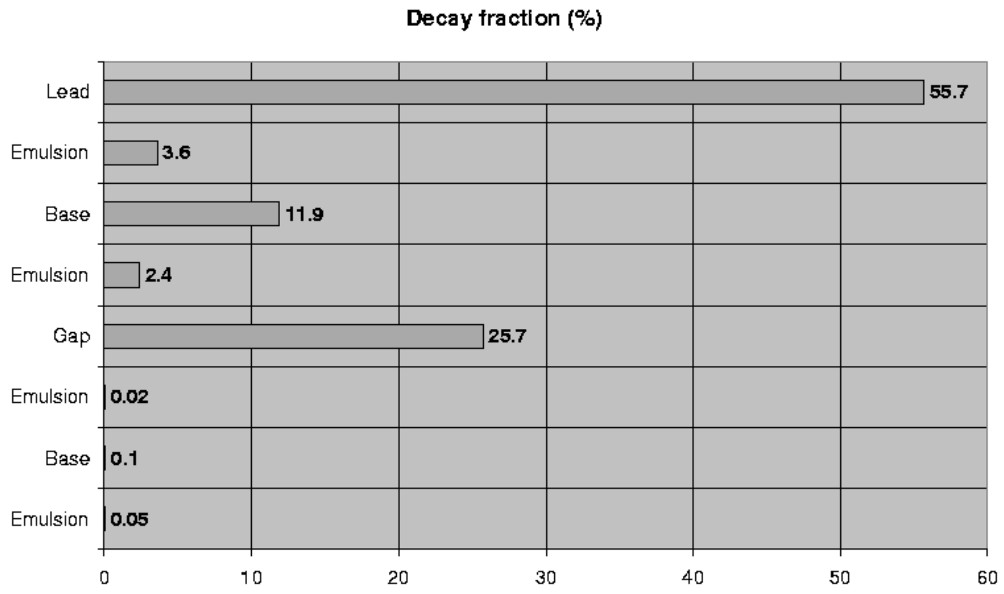

Figure 2.16: Distribution of the longitudinal τ decay length in the cell with spacer.

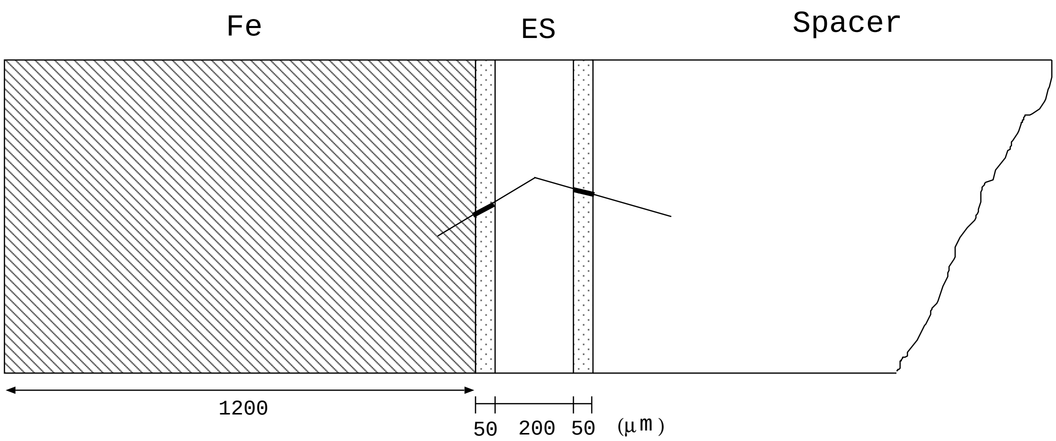

Figure 2.17: Kink angle for τ decaying in the first ES plastic base.

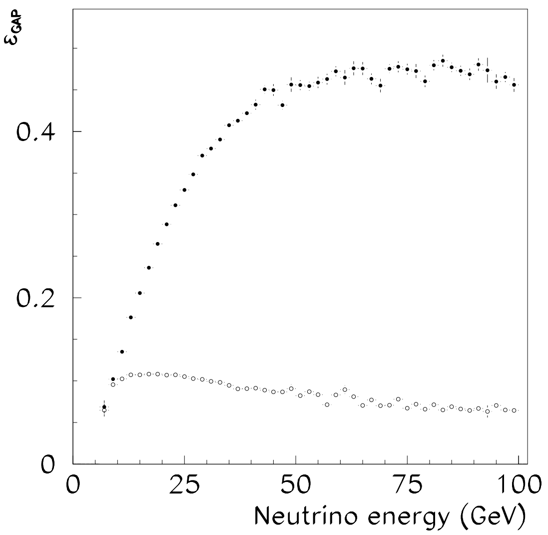

Figure 2.18: Probability of long τ decay kinks as a function of the neutrino energy. Open circles: decays in the first ES base; black circles: decays in the spacer.

the space. Test beam measurements (see Section 5.1.3) indicate that the angular resolution per projection, measured by means of four track segments in the ESs, is $\sigma_\theta \sim 5\ mrad$, while it becomes $\sigma_\theta \sim 10\ mrad$ for decays in the base. Therefore, the lower cut has been set to 25 $mrad$ (50 $mrad$) for decays in the spacer (base). In this way one rejects fake kinks due to the angular resolution. This resolution would be improved, in principle, by fully exploiting the grain information of the ES track segments. However, this would require local analyses whose feasibility must be assessed.

The fraction ε_{kink} of τ decays with a kink angle in the useful range depends of the actual decay mode. It amounts to $\sim 85\%$ for the electron and muon decay modes and $\sim 90\%$ for the hadronic decays. The standard set of oscillation parameters has been assumed.

One has also to consider the probability that one of the two segments corresponding to the kink is lost or not associated in space. This can be due to scanning inefficiencies and to possible cuts due to resolution effects. The overall efficiency depends on the scanning method. We have seen that once the interaction vertex is located, a *restricted Net Scan* is applied to the vertex region with the aim of picking-up all track segments and then perform the decay search. This procedure is being developed and follows the progress of the analysis methods presently used for DONUT and CHORUS. With the present knowledge an inefficiency at the percent level can be anticipated.

It will be shown in Section 2.5.3 that the decays of low energy hadrons in the spacer are a potential background source, because of their short flight length and large decay angle. Its suppression profits from the easier multiple scattering measurement at low momenta. Although the cut essentially acts on the (low) energy, it is more effectively expressed in terms of p_t at the decay vertex. The fraction ε_{p_t} of τ hadronic decays with p_t larger than 250 MeV/c amounts to 75% and for electronic and muonic decays to 85%.

We point out that the decay daughter identification is, in principle, not necessary for spacer bricks unlike for compact bricks. Since all single prong decay channels are retained, a wrong particle identification only leads to attribute the event to a different decay mode.

In order to measure the momentum of the decay daughters by multiple scattering, one has to follow particle tracks in the downstream (or adjacent) brick for some of the candidate events. Therefore, one needs to evaluate the effect of the brick-to-brick event connection efficiency on the overall τ detection efficiency. This is a function of the actual scanning method employed, of the brick dimensions, of the vertex position inside the brick and of the decay channel. Planned studies will quantify this effect.

2.4.7 Detection efficiency for compact bricks

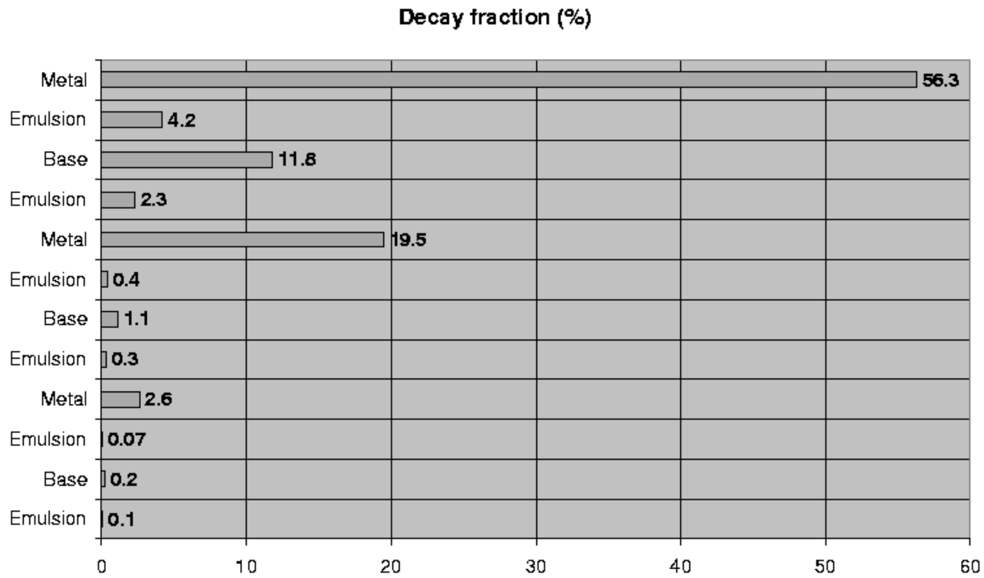

Figure 2.19: Distribution of the longitudinal τ decay length in the compact elementary cell. ν_τ interactions are assumed to occur in the first metal plate.

The distribution of the longitudinal τ decay length in the compact cell is shown in Fig. 2.19. Compact bricks are designed to detect the electron and muon decay channels of the τ. The identification of the daughter electron is done by exploiting the special energy loss behaviour in the plates downstream of the vertex plate. In the following, analyses based on Monte Carlo simulations are presented. Using arguments analogous to those applied to spacer bricks, decays occurring between the base of the first ES downstream of the vertex plate and the base of the first ES of the next to following cell are retained ($\sim 38\%$).

Electron identification algorithms have been studied by Monte Carlo simulations with mono-energetic electrons and pions. The GEANT 3.21 package was used to produce events with momenta ranging from 1 to 10 GeV/c and to generate hits in the emulsions, as described in Section 2.4.1. All particles emerging from the electron shower are simulated down to 20 MeV/c momentum. The same energy threshold is applied in the generation of pion interactions.

One method exploits the difference between electromagnetic and hadronic induced showers. Starting from the cell of the interaction vertex a cone of 50 $mrad$ is opened. All emulsion track segments found in the general scanning acceptance ($\pm$ 500 $mrad$ in each projection) are summed-up. As an example, in Fig. 2.20 the number of track segments (as defined above) inside the cone is plotted as a function of the vertex cell position, both for electrons and pions of the same energy (10 GeV). A cut on this quantity is suitable to separate electrons from pions. Its optimisation may take into account the actual vertex position. With this method, one obtains an electron detection efficiency ε_e of about 80% for an electron purity higher than 95%.

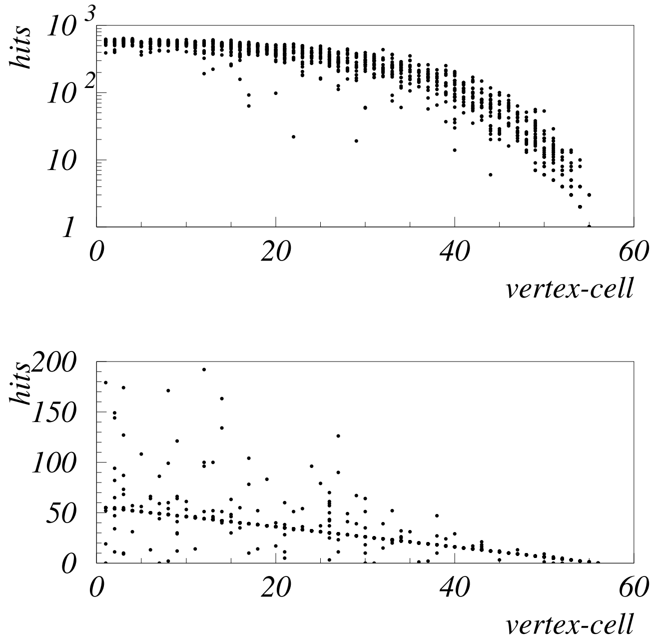

Figure 2.20: The number of tracks inside a cone of $\pm$500 $mrad$ as a function of the vertex plate both for 10 GeV electrons (top) and 10 GeV pions (bottom). Note the different vertical scale.

Another more refined method exploits the different energy loss between electrons and hadrons in measuring the scattering along the track. In the case of electrons the energy loss proceeds through bremstrahlung, with an exponential energy dependence. On the other hand, hadrons loose their energy by ionisation. By a χ^2 fit one can distinguish between the exponential and the dE/dx energy loss behaviour. One can then identify $80 - 90\%$ of the electrons within about 5 X_0. By combining the electromagnetic shower detection with the result of the above fit, $\sim$ 98% of the electrons can be identified with a purity higher than 95% (Fig. 2.21). The dependence of the electron identification on the depth of material traversed after production is shown in Fig. 2.22. A good electron identification is obtained after two radiation lengths. On the other hand, it is rather difficult to identify the electron within the vertex brick as soon as the vertex plate is downstream of cell number 45. This motivates the need, in that case, of connecting consecutive bricks.

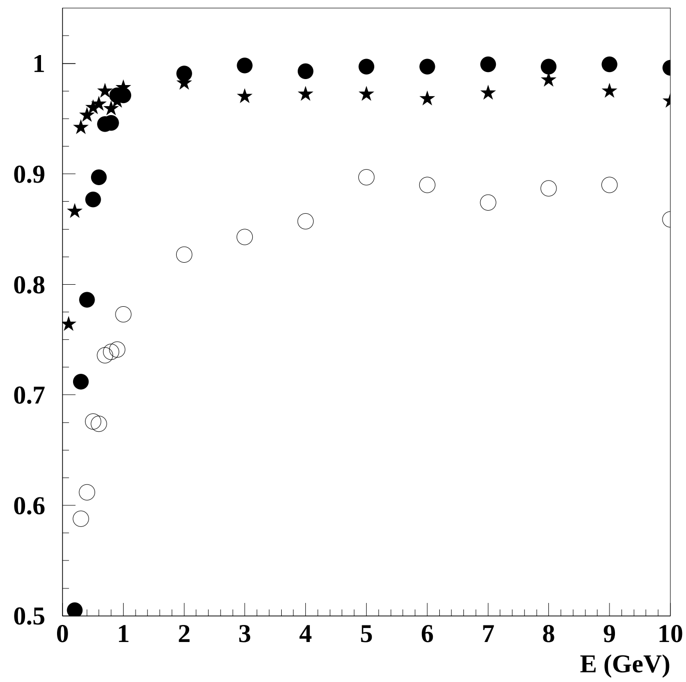

Figure 2.21: The electron detection efficiency as a function of the energy (open circles). The same quantity is plotted in the case when one also exploits electromagnetic shower detection (black circles); the corresponding purity is also shown (stars).

On the basis of the above calculations, we make the conservative choice of assuming an electron detection efficiency $\varepsilon_e = 80\%$. Test measurements will contribute to the development of more efficient algorithms and to the experimental determination of ε_e. The programme of tests has started and some results will be presented in Section 5.1.5.

A calibration in energy has been performed by a Monte Carlo simulation. The number of tracks inside the cone satisfying the scanning cuts is counted as a function of the electron energy. The results indicate an energy resolution of $\sim 20 - 30\%$ for an electron energy above 2 GeV. The electron energy resolution has been the subject of measurements performed with prototype bricks exposed to test beams. Their analysis is underway.

The muon detection efficiency ε_μ amounts to $\sim$ 80% for muonic τ decays occurring in the lead. In addition, one has to reject kinks which may originate from the scattering of a prompt muon in the lead.

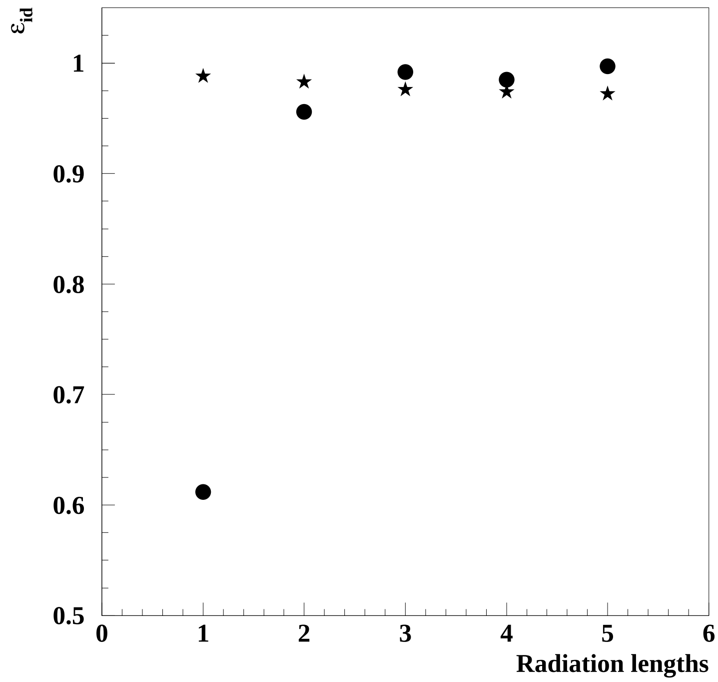

Figure 2.22: The electron identification efficiency as a function of the depth (in radiation lengths) of the traversed material (circles). The electron purity is also shown (stars).

Table 2.4: Detection efficiency for different τ decay modes and types of supermodules (for $\Delta m^2 = 3.5 \times 10^{-3}\ eV^2$).

Supermodule	Decay mode	τ det. eff.
spacer	$\tau \rightarrow e^-$	3.0%
"	$\tau \rightarrow \mu^-$	2.6%
"	$\tau \rightarrow h^-$	7.3%
"	total	12.9%
compact	$\tau \rightarrow e^-$	3.0%
"	$\tau \rightarrow \mu^-$	2.6%
"	total	5.6%

This issue is discussed in Section 2.5.4. With a suitable cut on the total momentum and on p_t, an efficiency for the signal $\varepsilon_{p_t} = 85\%$ is obtained. We stress that this cut is not needed for electron decay events which can be identified by the methods discussed above.

2.4.8 Overall detection efficiency for long decay events

One can now evaluate the overall signal detection efficiency for *long decay* events for spacer and compact supermodules. We define

$$\varepsilon_{common} = \varepsilon_{br} \times \varepsilon_{geom} \times \varepsilon_{vert} \times \varepsilon_{long} \tag{2.1}$$

as the efficiency contribution common, in a first approximation, to all decay modes. Introducing also the branching ratio (BR), the detection efficiencies for the various channels are

$$\begin{aligned}
\varepsilon_{tot}(electron) &= \varepsilon_{common} \times \varepsilon_{kink} \times \varepsilon_{p_t} \times \varepsilon_e \times BR \quad \text{(spacer)} \\
\varepsilon_{tot}(electron) &= \varepsilon_{common} \times \varepsilon_{kink} \times \varepsilon_e \times BR \quad \text{(compact)} \\
\varepsilon_{tot}(muon) &= \varepsilon_{common} \times \varepsilon_{kink} \times \varepsilon_{p_t} \times \varepsilon_\mu \times BR \quad \text{(spacer and compact)} \\
\varepsilon_{tot}(hadron) &= \varepsilon_{common} \times \varepsilon_{kink} \times \varepsilon_{p_t} \times BR \quad \text{(spacer)}
\end{aligned}$$

By multiplying all factors and accounting for deep-inelastic (DIS), quasi-elastic (QE) and resonance interactions (RES), one obtains the efficiencies shown in Table 2.4.

Note that the lower efficiency of the compact supermodules shown in Table 2.4 is counterbalanced by twice the target mass at the same amount of emulsion.

The knowledge of the τ detection efficiency will be improved by further studies and measurements. In particular, work is planned or in progress on the vertex finding, on the brick-to-brick event connection and on the electron identification.

2.5 Background

The background evaluation has been performed by means of a full simulation including the beam features, the physics processes and the detector structure. The expected background sources for long decay events are

- prompt ν_τ production in the primary proton target and in the beam dump;
- cosmics and radioactivity;
- hadronic decays and re-interactions;
- muon scattering;
- 1-prong decay of charmed particles.

The effect of the above sources depends on the specific decay channel and of the type of brick.

2.5.1 ν_τ prompt background

Prompt ν_τ originate from the decay of τ produced in the CNGS target by D_s mesons. The rate of ν_τ production through the interaction of 450 GeV protons in a Be target and in the downstream beam dump has been evaluated in [44, 45] for the CERN Wide Band Beam. Prompt ν_τ production in OPERA has to be scaled taking into account the different features of the CNGS beam and the distance of the experiment from the source. Following the method of [44], a total of $1.5 \times 10^{-6} \times N_{CC}$ ν_τ interactions would occur. N_{CC} is the total number of ν_μ CC events collected in OPERA. If one also takes into account the detection efficiency this contribution becomes completely negligible.

2.5.2 Beam unrelated background

The kink finding procedure is based on the space association of track segments reconstructed with the two ESs of a cell. Given the angular range allowed for the kink ($\pm$ 500 $mrad$), the segments corresponding to the τ and to its daughter are searched for over an ES surface which depends on the distance between the two consecutive ESs (3 mm for spacer cells and 1 mm for compact cells). Therefore, one has to consider the potential background given by accidental association with isolated track segments, which could originate from beam-unrelated sources. The smaller surface scanned in the case of compact cells (due to the smaller lever arm) makes this association probability lower than for spacer cells.

The main beam unrelated source is given by β rays from lead radioactivity. The background from radioactivity in the experimental hall is expected to be negligible. Measurements will be soon performed with test experiments using emulsion sheets poured and exposed in the Gran Sasso cavern.

The lead radioactivity level strongly depends on the lead origin and can vary by more than one order of magnitude. For a given type of lead the rate of detected α particles in the emulsion can be used as a measurement of the radioactivity. The experiment requires less than ~ 1 α particle per microscope view integrating over the exposure time.

We performed tests by two methods. In the first, ESs are placed in direct contact with the lead plates under test and the recorded α particles are counted. In the other method, the rate of α and β emissions

Table 2.5: Decay rates in the spacer.

Decay mode	Events $\times 10^{-4}/N_{CC}$
$\pi \to \mu$	2.2
$K \to \pi + \pi^0$	0.3
$\Sigma \to p\ (\pi)$	7.6

from the lead plate are measured separately by using 2π proportional gas chambers with a cosmic ray veto. The measured α rates by the two methods are compared to each other. The calibration factor which is also applied to convert the β rate to the real data is estimated. The resulting α rates range from 0.2 to 15 particles per view, extrapolated to five years exposure. The corresponding numbers of β electron tracks go from 5 to 100 per view. With suitable selection of the commercial lead the radioactivity background can be kept at a low level.

Another source of background is due to cosmic ray exposure prior to ES location in the Gran Sasso cavern. This produces isolated and uncorrelated track segments in the different ESs of a brick thus representing a potential source of accidental kinks. There are ways to overcome this problem and keep this background at the acceptable level of ~ 1 segment per square millimetre. The first consists in packing the ESs needed for one brick soon after production and in keeping their order and relative position when assembling the brick. In this way, cosmic rays would be recognised by the scanning system as passing through tracks. Another way to reduce this background would imply the use of emulsions with controlled fading. Tracks stored before data taking could be erased with a suitable procedure based on temperature variations. A drastic approach would require to assemble bricks with two ESs instead of one, so identifying cosmic tracks as correlated segments in the two ESs. This scheme, obviously, requires the use of twice as many ESs. The above arguments show that, in principle, one can keep the cosmics background under control and reduce the probability of fake track associations.

Test measurements are planned to address the issue of beam-unrelated backgrounds and to quantify their effect on the OPERA performance.

2.5.3 Hadron decays and re-interactions

We have estimated the number of hadronic re-interactions or decays which may mimic a τ decay by means of a GEANT 3.21 based Monte Carlo. About 10^5 ν_μ CC and NC events have been generated with all particles produced in a metal plate followed downstream. All physical processes occurring in the spacer have been considered and studied in detail.

The potentially relevant sources of background for hadron decays in the spacer are shown in Table 2.5. The detection efficiency and the selection criterion on the apparent kink angle ($25 - 500\ mrad$) have been considered. The events are characterised by relatively low momentum, as shown in Fig. 2.23. A cut on the decay particle transverse momentum can be applied. The p_t distribution is shown in Fig. 2.24. By rejecting p_t lower than 250 MeV/c no background events survive. This background is even less important for compact bricks.

We also studied re-interactions of charged particles in the low density spacer ($\sim 30\ kg/m^3$). 100000 ν_μ CC events have been simulated. Out of them, 37 events have a charged hadron interacting in the spacer

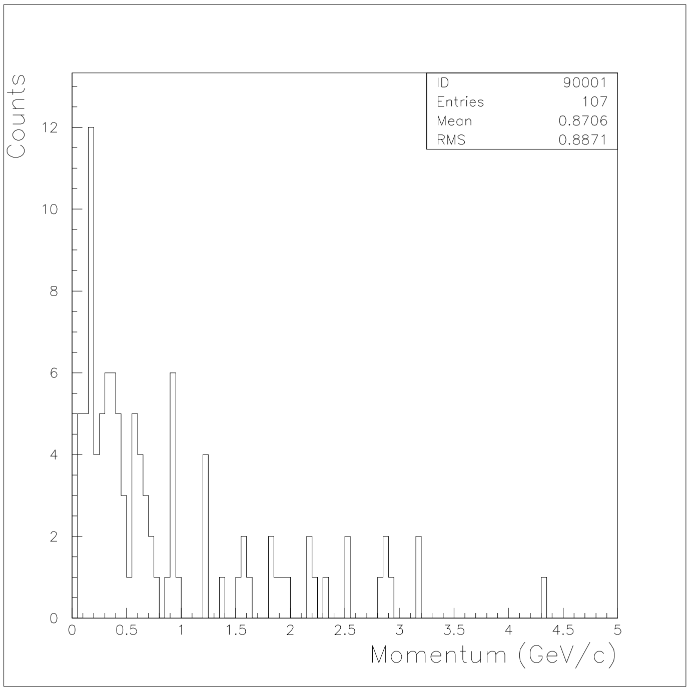

Figure 2.23: Momentum distribution of particles from decays in the spacer.

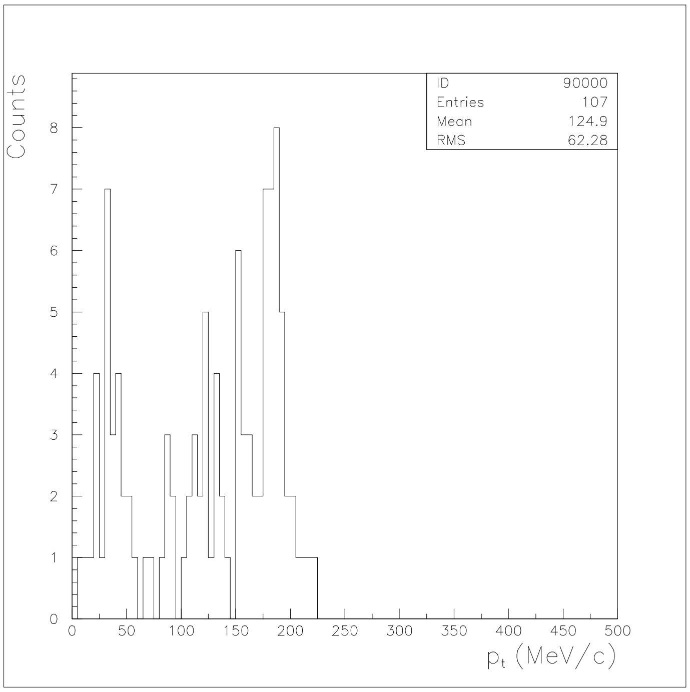

Figure 2.24: p_t distribution of particles decaying in the spacer.

material. Only one event out of the 37 exhibits a topology similar to a τ decay. This single event, however, is characterised by very low momentum of the scattered particle (550 MeV/c) and is already eliminated by the previously described p_t cut.

The above results indicate that less than $1 \times 10^{-5} \times N_{CC}$ background events are expected from hadron decays and re-interactions.

2.5.4 Background from muon scattering

This background is only relevant for compact bricks. In this case, a muon may undergo a Coulomb scattering in the lead plate following the vertex plate hence mimicking a muonic τ decay. About 70000 ν_μ CC events in compact bricks have been simulated according to the CNGS beam spectrum. In 0.5% of the events, the prompt muon has an *apparent* kink angle larger than 25 $mrad$ in the lead plate downstream of the vertex plate.

In Fig. 2.25 the muon transverse momentum is shown for τ and background events as a function of the momentum. The correlation between the two quantities is exploited to apply a combined cut, shown in the Figure. Taking into account the other factors of the detection efficiency (ε_{geom}, ε_{br} and ε_{vert}), one is left with a background of $1.3 \times 10^{-5} \times N_{CC}$ events for a 1 mm lead plate. Since decays are searched for in two consecutive lead plates behind the vertex one, the total background becomes $2.6 \times 10^{-5} \times N_{CC}$.

In order to check the above results, we have also generated (by a GEANT 3.21 simulation) muons of different energies crossing orthogonally 1 mm of lead. The projected angular distribution has a width which is consistent with the expectations from theoretical calculations. The contribution from non Gaussian tails amount to about 2% of the total sample, justifying the above evaluation. We observe that this background can be measured. We are planning to do this in the near future.

2.5.5 Charm production and decay

Charmed particles are produced in CC and NC neutrino interactions through the reactions:

$$a)\ \nu_\mu N \rightarrow c\,\mu X, \qquad b)\ \nu_\mu N \rightarrow c\bar{c}\,\mu X, \qquad c)\ \nu_\mu N \rightarrow c\bar{c}\,\nu_\mu X$$

Charmed mesons have mass and lifetime similar to those of the τ. The above processes may thus constitute a background to the oscillation signal, if one fails to detect the primary muon (a), the charm partner (c) or both (b).

The most relevant source is given by single charm production (reaction (a)). The (positive) sign of the D^+ daughter is only measured for the muonic channel by the muon spectrometer. This is done in about 70% of the cases. Hence, if the primary muon is missed, a D^+ meson decaying in one charged particle (plus neutrals) can fake a genuine τ event.

In order to evaluate the expected charm background we must take into account the theoretical uncertainties on the evaluation of the charm production cross section in deep inelastic (DIS) neutrino interactions ([46] and references therein). Relatively to ν_μ CC interactions, the fraction of events with a charmed hadron in the final state strongly depends on the value assumed for the charm quark mass. It also depends on the parton distributions, which in turn are a function of the QCD scale (μ), whose dependence on Q^2 and x-Bjorken is not well known. Due to the above uncertainties, we adopted a parametrisation as a function of the

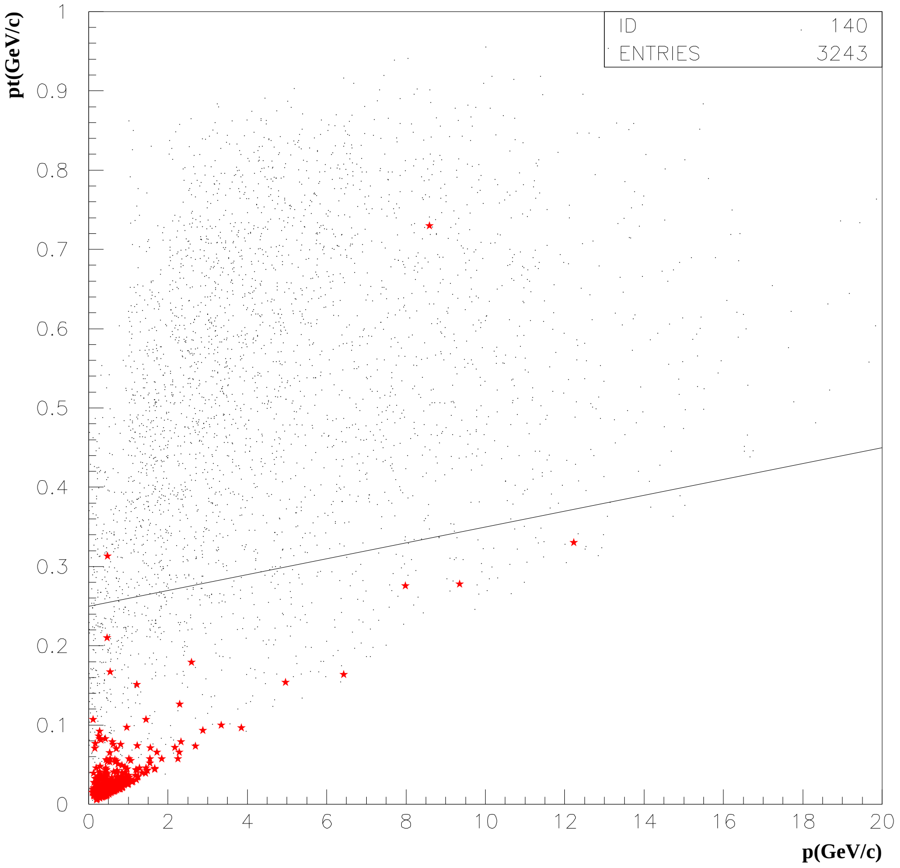

Figure 2.25: p_t vs momentum distribution of prompt muons scattering in the lead (stars) and of muons from τ decay (dots). The kink angle selection criteria have been applied. The cut to reduce the background is shown as a straight line.

neutrino energy (Fig. 2.26) which reproduces the E531 data [47]. By convoluting the above parametrisation with the CNGS neutrino spectrum [42] one obtains

$$\frac{\sigma(\nu_\mu N \rightarrow \mu^- cX)}{\sigma(\nu_\mu N \rightarrow \mu^- X)} \equiv \frac{\sigma_c}{\sigma_{CC}} = (3.3 \pm 0.5)\% \tag{2.2}$$

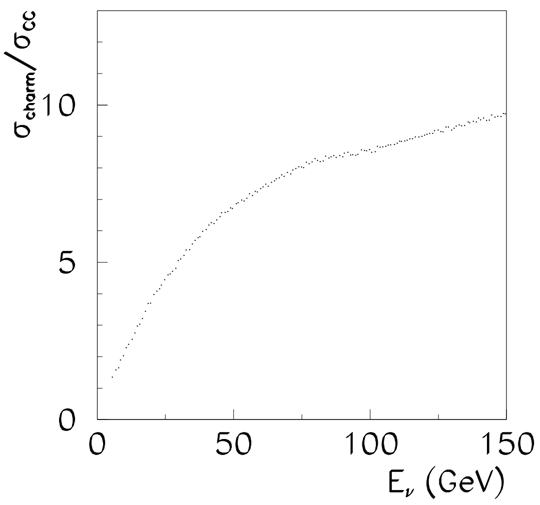

Figure 2.26: Parametrisation of the relative charmed-particle production rate in ν_μ CC interactions, as a function of the neutrino energy. The vertical scale is in %.

We then assume the factorisation theorem to obtain the charmed hadron (C) cross section, which can be related to the charm quark (c) cross section through fragmentation functions:

$$\frac{d^5\sigma(\nu_\mu N \rightarrow \mu^- CX)}{dxdydzdp_t^2} = \frac{d^2\sigma(\nu_\mu N \rightarrow \mu^- cX)}{dxdy} \times \sum_h f_h \times D_c^h(z, p_t^2) \tag{2.3}$$

where $D_c^h(z, p_t^2)$ is the probability distribution for the charm quark fragmenting into a hadron h carrying a fraction z of the quark's longitudinal momentum and transverse momentum p_t with respect to the quark direction.

The quantity f_h is the fraction of hadrons h among the produced charmed hadrons. We assume $\sum_h f_h = 1$ with the sum extended to the hadrons considered below. From the equation (2.3) it follows that f_h depends on the chosen hadronisation scheme (*i.e.* the functions $D_c^h(z, p_t^2)$). Several sets of the $D_c^h(z, p_t^2)$ exist [46]. We used functions determined from fits to neutrino charm production data [47, 48]. The charmed hadron fractions f_{D^0}, f_{D^+}, $f_{D_s^+}$ and $f_{\Lambda_c^+}$ are given in [48] as a function of the neutrino energy. Since the charmed hadrons have different $c\tau$ the expected background depends on the values of f_h which in turn are function of the neutrino energy. In the case of the CNGS beam one obtains

$$f_{D^0} = 0.45 \pm 0.14, \quad f_{D^+} = 0.10 \pm 0.03, \quad f_{D_s^+} = 0.18 \pm 0.05 \text{ and } \quad f_{\Lambda_c^+} = 0.26 \pm 0.08$$

The branching ratios of the charged charmed hadrons have been taken from the PDG [49].

In the special case of quasi-elastic charm production, one has

$$\frac{\sigma(\nu_\mu n \to \mu^- \Lambda_c^+)}{\sigma(\nu_\mu N \to \mu^- X)} = 0.6\%$$

In addition, most of the produced charmed-baryons decay in a short distance (within the lead plate). Since we are considering *long* decays, this contribution to the background is negligible.

The background from single charm production can then be determined as follows. In ν_μ CC interactions, C^+ mesons $(D^+, \Lambda_c^+, D_s^+)$ are produced. If the primary muon is missed, a C^+ decaying in one charged particle (we consider single-prong τ decay modes) can fake a genuine τ event, if the charge of the daughter particle is not measured. For each decay channel the background from C^+ can be written as follows

$$N_{bg} = \frac{\sigma_c}{\sigma_{CC}} \times f_{C^+} \times (1 - \varepsilon_{ch}^{C^+}) \times \varepsilon_{common} \times \varepsilon_{kink} \times (1 - \varepsilon_\mu^{charm}) \times BR \times N_{DIS}$$

where ε_{common} is defined by equation 2.1 and N_{DIS} is the total number of CC deep-inelastic events. The contributions from QE and RES neutrino interactions are negligible.

For events occurring in supermodules with spacer bricks we obtain $2 \times 10^{-5} \times N_{DIS}$ background events for the 1-prong hadronic D decay, $0.3 \times 10^{-5} \times N_{DIS}$ events for the muonic channel and $0.5 \times 10^{-5} \times N_{DIS}$ events for the electron channel. For compact bricks the charm background produces about $0.09 \times 10^{-5} \times N_{DIS}$ events for the muonic channel and the same for the electron channel. The contribution from $\overline{\nu}_\mu$, ν_e and $\overline{\nu}_e$ to the charm background is in any case negligible, as they constitute only a small contamination of the ν_μ beam.

Another potential source of charm background is given by the associated charm production, where two charmed hadrons are produced and one of the two escapes detection. This process has been observed only by E531 [47] with one single event compatible with the NC production of a pair of charmed particles $(D^0 - \bar{D}^0)$. The neutral current $c\bar{c}$ production rate can then be estimated to be

$$\frac{\sigma(\nu_\mu N \to c\bar{c}\nu_\mu X)}{\sigma(\nu_\mu N \to \nu_\mu X)} \equiv \frac{N_{c\bar{c}}}{N_{NC}} = 0.13^{+0.31}_{-0.11}\%$$

If, instead, one makes the assumption that in the observed event a muon from the lepton vertex was not identified, the following upper limit on $c\bar{c}$ production in CC interactions is obtained

$$\frac{\sigma(\nu_\mu N \to c\bar{c}\mu X)}{\sigma(\nu_\mu N \to \mu X)} < 0.12\%$$

In the following, we will assume that the $c\bar{c}$ production is the same both in neutral and charged current neutrino interactions. In order to extrapolate the above results to OPERA one needs to know how the

Table 2.6: Probability to have a given pair of charmed particles in the final state ($f_{CC'}$). The final state which does not contribute to the background is indicated with bold character.

	D^0	D^+	D_s^+	Λ_c^+
$\bar{D}^0$	**0.203**	0.045	0.081	0.117
D^-	0.045	0.010	0.018	0.026
D_s^-	0.081	0.018	0.032	0.047
Λ_c^-	0.117	0.026	0.047	0.068

produced charm quark is dressed, *i.e.* the charmed fractions f_h and $\bar{f}_h$. There are no experimental measurements of these quantities. Therefore, we have to use the z and p_t^2 distributions valid for single charm production. The results are shown in Table 2.6.

The contribution of associated charm production can be written for the different channels and for both CC and NC reactions as

$$N_{bg}(CC) = \frac{N_{c\bar{c}}}{N_{CC}} \times f_{CC'} \times (1 - \varepsilon_{ch}^{C^\pm}) \times \varepsilon_{common} \times \varepsilon_{kink} \times (1 - \varepsilon_{\mu}^{charm}) \times (1 - \varepsilon_{c\bar{c}}) \times BR \times N_{DIS}$$

$$N_{bg}(NC) = \frac{N_{c\bar{c}}}{N_{NC}} \times f_{CC'} \times (1 - \varepsilon_{ch}^{C^\pm}) \times \varepsilon_{common} \times \varepsilon_{kink} \times \frac{\sigma_c}{\sigma_{CC}} \times (1 - \varepsilon_{c\bar{c}}) \times BR \times N_{DIS}$$

The above expressions lead to a total background from associated charm lower than $0.1 \times 10^{-5} \times N_{DIS}$ events, for spacer as well as for compact bricks.

Within the present estimates the assume a $\sim 10\%$ systematic error on the total number of events from charm. The precision on the background evaluation for OPERA will benefit in the future from the ongoing charm analysis performed by CHORUS.

2.6 Short decays

Short τ decays are affected by background sources like hadronic re-interactions and charm decays, hence they are not considered for the present evaluation of the sensitivity and of the discovery potential. However, such events could be used at a later stage for the determination of the oscillation parameters, once the experiment has observed a clear signal. In particular, we can consider the τ muonic decays occurring in a lead plate.

The main background to the muonic short-decays comes from charm. Let's consider events with a vertex (formed by at least two tracks) observed in the lead plate and with an identified muon having a large impact parameter. These events can be either due to a τ decay or to a charm hadronic decay with no other detected hadron tracks from the neutrino interaction vertex, as shown for a spacer cell in Fig. 2.27. In other words, it is topologically impossible to ascertain whether the observed vertex is the primary neutrino interaction vertex (signal) or a secondary charm decay vertex.

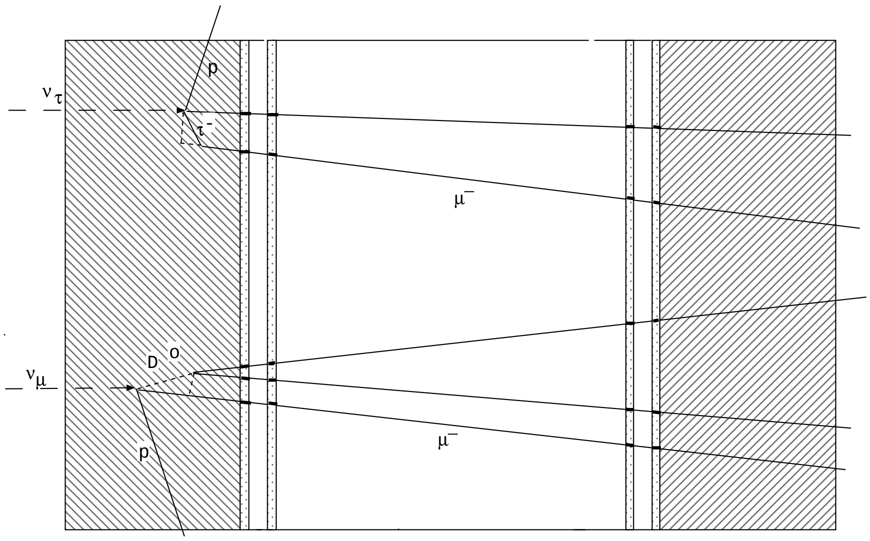

Figure 2.27: Signal and charm background for $\tau \to \mu$ short decays.

In principle, one can discriminate between the above two cases by estimating the invariant mass of the particles originating from the observed vertex. For charm decays this mass is bound to the charmed hadron mass. For τ decays its value can be larger. Methods based on kinematics can thus be used to improve the signal to background ratio. Their application relies on the measurement of particle momenta by multiple scattering. The first calculations encourage to pursue these studies.

2.7 Sensitivity to oscillations and discovery potential

2.7.1 Sensitivity

Table 2.7 summarises the number of signal and background events which can be collected in the various channels by one supermodule (spacer or compact) with $2.25 \times 10^{20}\, pot$ from the SPS. This corresponds to a nominal five years run not considering the possibility for a dedicated running mode or an improved CNGS performance.

In order to cover the Super-Kamiokande allowed region [10], five supermodules are required. One could then obtain ~ 20 events if $\nu_\mu \leftrightarrow \nu_\tau$ oscillations occur at the Super-Kamiokande central value of $\Delta m^2 = 3.5\ \times 10^{-3}\ eV^2$.

Further studies of the detailed performance are needed before a decision on the supermodule configuration is made. For the evaluation of the general features of the experiment in terms of sensitivity and discovery potential we consider here the combined use of both types of supermodules in a scheme which leads to the detection of a suitable signal in the different channels. The entire detector can comprise five supermodules

Table 2.7: τ and background events detected by one spacer or compact supermodule. Full mixing and three values of Δm^2 are assumed. The values are given for $2.25 \times 10^{20} pot$.

Supermodule	τ decay mode	Signal ($2 \times 10^{-3} eV^2$)	Signal ($3.5 \times 10^{-3} eV^2$)	Signal ($6 \times 10^{-3} eV^2$)	BG
spacer	e^-	0.26	0.81	2.38	0.010
"	μ^-	0.23	0.70	2.06	0.006
"	h^-	0.64	1.97	5.79	0.036
compact	e^-	0.65	2.00	5.88	0.040
"	μ^-	0.56	1.73	5.08	0.15

in a row. Three supermodules would be assembled with bricks with spacers, for a total mass of ~ 555 ton. Two supermodules with compact bricks can yield a mass of ~ 910 ton employing a quantity of emulsions similar to that of the three supermodules with spacer bricks. The total target mass would amount to about 1500 ton. With 2.25×10^{20} pot the experiment would collect $\sim$ 18000 charged current and $\sim$ 6000 neutral current ν_μ events, summing-up DIS, QE and RES events.

In order to compute the sensitivity to $\nu_\mu \leftrightarrow \nu_\tau$ oscillations, the energy dependence of the neutrino spectra and of the detection efficiencies have been taken into account. The conventional two-flavour mixing has been assumed to evaluate the performance of the experiment in comparison with experimental observations.

OPERA is expected to obtain a signal of oscillations in various channels each characterised by a specific background and statistical significance. Therefore, the sensitivity has been evaluated with a method similar to the one described in [50]. This method allows the computation of exclusion confidence levels by combining different experimental channels. Furthermore, it gives the possibility to take into account the uncertainty in the estimated signal and in the background of each event sample.

In the framework of this method, several experiments have been simulated. The observed number of events is extracted according to a Poisson distribution with a mean corresponding to the expected signal and background. In this way, one can obtain exclusion limits and, in the case of a positive search, confidence levels.

The aim of OPERA is to be sensitive to the oscillation parameter region corresponding to the Super-Kamiokande signal. The low expected background is the key element to achieve this goal. The sensitivity in Δm^2 improves with the square root of the number of detected events. This implies that already after a run of about two years a significant limit could be set in the case of a negative search. This is shown in Fig. 2.28, where the exclusion plots at the 90% CL are given for a two, three or four years' run. The Figure also shows the result from a global fit of the different Super-Kamiokande measurements on atmospheric neutrinos. The result is consistent with full mixing and indicates a Δm^2 range which extends at the 90% CL from about 2 to 6×10^{-3} eV^2 [10].

At the 90% CL, a four years' run yields a limit on the mixing angle (for large Δm^2) $\sin^2 2\theta_{\mu\tau} < 6.2 \times 10^{-3}$ and a minimum Δm^2 (for full mixing) of $1.2 \times 10^{-3}\ eV^2$.

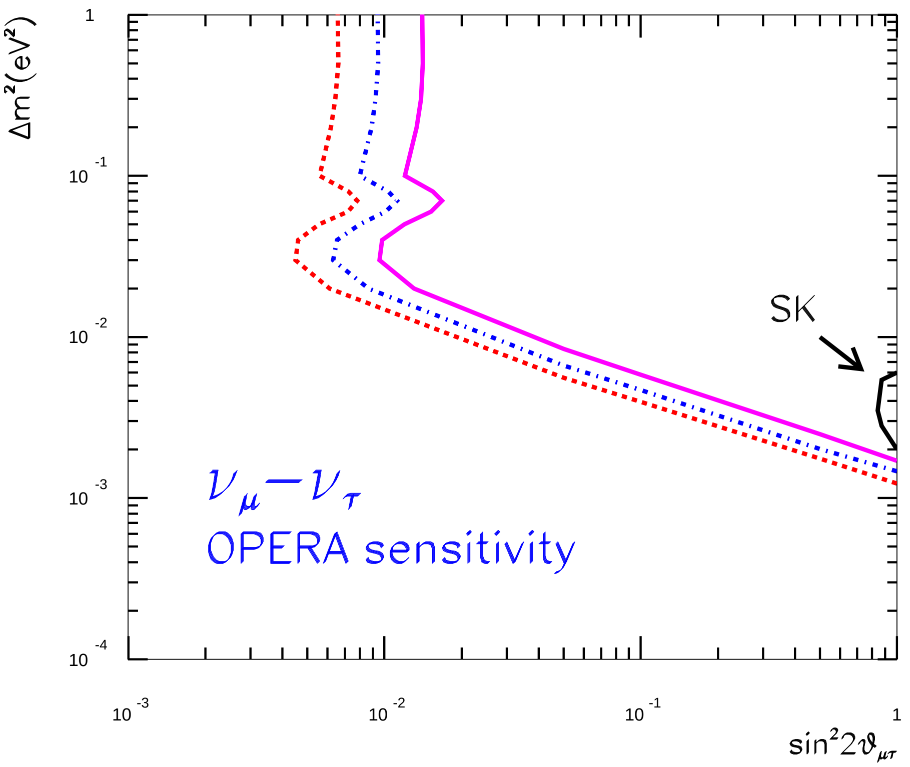

Figure 2.28: Sensitivity of OPERA in the search for $\nu_\mu \leftrightarrow \nu_\tau$ oscillations. The 90% CL exclusion limits (2, 3 and 4 years' run) are plotted together with the region allowed by Super-Kamiokande.

2.7.2 Discovery potential

Arguments similar to those presented in the previous Section also apply to the case when a signal is observed by the experiment. OPERA should be able to detect candidate events already after one or two years of run. With the low expected background the statistical significance improves linearly. A long run would then be motivated. This justifies our choice of normalising the experiment performance to 2.25×10^{20} *pot*, *i.e.* five years of nominal CNGS running.

Table 2.8 gives the expected numbers of τ events detected in the various decay channels with the supermodule configuration taken in the previous Section. In each of the three decay channels the expected number of events is almost equal. Assuming that $\nu_\mu \leftrightarrow \nu_\tau$ oscillations occur with parameter values $\Delta m^2 = 3.5\ \times 10^{-3}\ eV^2$ and $\sin^2 2\theta_{\mu\tau} = 1$, about 18 ν_τ CC events are detected by OPERA. Since the unambiguous experimental signature leads to a very low background, this number is representative for the discovery potential.

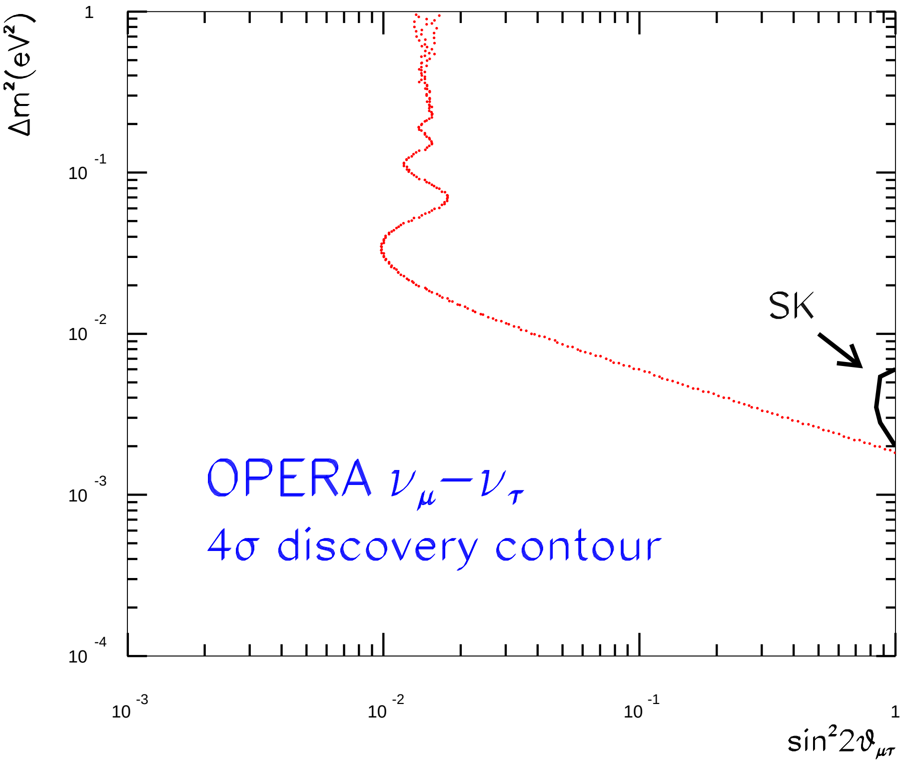

Figure 2.29: Four σ discovery potential of OPERA in the search for $\nu_\mu \leftrightarrow \nu_\tau$ oscillations (2.25×10^{20} *pot*).

Table 2.8: Detected τ and background events with three spacer and two compact supermodules, for full mixing, three values of Δm^2 and $2.25 \times 10^{20} pot$.

τ decay mode	Signal ($2 \times 10^{-3} eV^2$)	Signal ($3.5 \times 10^{-3} eV^2$)	Signal ($6 \times 10^{-3} eV^2$)	BG
e^-	2.1	6.4	18.9	0.11
μ^-	1.8	5.6	16.3	0.32
h^-	1.9	5.9	17.4	0.11
Total	5.8	17.9	52.6	0.54

In Fig. 2.29, the 4 σ discovery contour is plotted in the $\sin^2 2\theta$–Δm^2 parameter plane. The 4 σ discovery level is defined by the $1.0 - (6.3 \times 10^{-5})$ CL upper limit of the Poisson distribution with a mean value corresponding to the expected number of background events. For full mixing this corresponds to $\Delta m^2 = 1.8 \times 10^{-3}\ eV^2$.

2.7.3 Determination of the oscillation parameters

In the case of a positive result, values for the oscillation parameters could be inferred. Given a parameter with true value μ_t and an experiment performing a measurement of a quantity $x_0(\mu_t)$, one can define an interval $[\mu_1, \mu_2]$ which contains the *true* (unknown) value μ_t in a fraction α of a series of experiments: $P(\mu_t \in [\mu_1, \mu_2]) = \alpha$). We determine the confidence interval (*central confidence interval*) so that

$$P(x < \mu_1 \mid \mu_t) = P(x > \mu_2 \mid \mu_t) = \frac{1-\alpha}{2}$$

The construction of the interval $[\mu_1, \mu_2]$ can be performed according to the method described in [50]. If $\nu_\mu \leftrightarrow \nu_\tau$ oscillations occur with *true* parameter values $\Delta m^2 = 3.5 \times 10^{-3}\ eV^2$ and $\sin^2 2\theta = 1$, we have seen that OPERA detects ~ 18 ν_τ events. One obtain in this case the 90% CL interval shown in Fig. 2.30. An experimental systematic error of 10% has been assumed on the estimated numbers of signal and background events.

OPERA is aimed at detecting ν_τ induced events unambiguously. However, once a clear oscillation signal has been found, one can make use of other channels for the determination of the oscillation parameters which are not background free. This applies in particular to the muonic τ decays in the lead (short kinks) discussed in Section 2.6 or to some hadronic decays in compact bricks (*e.g.* the $\tau \rightarrow \rho$ channel). We are studying this subject in order to obtain quantitative estimates.

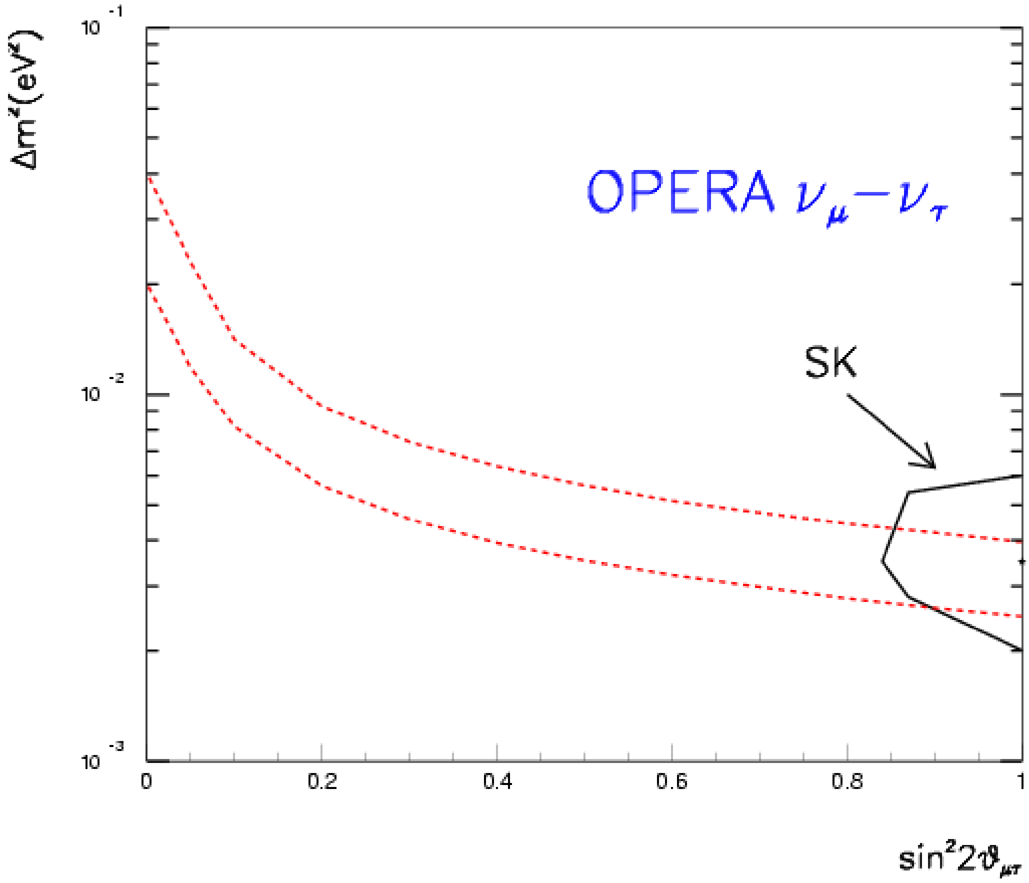

Figure 2.30: OPERA allowed parameter region (90% CL) obtained under the assumption that $\nu_\mu \leftrightarrow \nu_\tau$ oscillations occur at the preferred Super-Kamiokande values.

2.8 Search for $\nu_\mu \leftrightarrow \nu_e$ oscillations

2.8.1 Physics motivations

OPERA is also sensitive to $\nu_\mu \leftrightarrow \nu_e$ oscillations. Together with the $\nu_\mu \leftrightarrow \nu_\tau$ appearance search this measurement will permit to perform a global three-flavour mixing analysis with a single experiment. The study presented below is based on two supermodules with compact bricks.

2.8.2 Electron detection

The primary tracks from the vertex in muon-less events are measured to look for the occurrence of ν_e CC interactions. Electron identification is performed by following tracks into the ESs downstream of the vertex plate. We carried out simulations and tests of the electron identification capability in compact bricks by means of energy loss measurements.

Algorithms for electron identification have been adjusted to multi-prong events, as required to identify electrons among all the primary tracks. Three samples have been considered in the simulations since they give the main contribution to signal and background: ν_e CC, ν_μ NC and ν_μ CC interactions with the muon not identified. An angular cone is opened around each track segment in the first ES after the vertex. Standard criteria are applied to identify an electron and to measure its energy. In order to reduce the background a 3 GeV cut on the reconstructed energy is applied.

The overall rejections of ν_μ NC and ν_μ CC are 95% and 90%, respectively. The efficiency for ν_e CC is 70% averaged over the neutrino spectrum. In Fig. 2.31 the efficiency for ν_e CC is plotted as a function of the neutrino energy.

2.8.3 Background

One background source is the ν_e ($\bar{\nu}_e$) contamination of the ν_μ beam, with a flux ratio ν_e/ν_μ of about 1%. This yields ~ 40 detected events, accounting for all factors in the detection efficiency.

Another background source are electrons from the Dalitz decay of neutral pions produced in ν_μ NC interactions ($\pi^0 \to e^+e^-\gamma$) and photon to electron conversions in the lead plates ($\pi^0 \to 2\gamma$ followed by $\gamma N \to e^+e^-N$). Selecting neutrino interactions with one electron (positron) identified of measured energy greater than 3 GeV we estimate a background of 140 events from neutral pions considering both ν_μ CC and NC interactions. The contamination from pions misidentified as electrons is included in this evaluation.

The statistical errors of the background events determine the sensitivity for the measurement of the oscillation parameters together with systematic errors due to the uncertainty ($\sim 10\%$) of the ν_e content of the beam and to the uncertainty ($\sim 20\%$) of the number of prompt electrons produced by π^0.

2.8.4 Sensitivity

In the case of a negative search and given $2.25 \times 10^{20}\, pot$, OPERA will achieve a limit for the mixing parameter of $\sin^2 2\theta_{\mu e} \sim 1.5 \times 10^{-2}$ (90% CL) for large Δm^2. For full mixing the limit for Δm^2 is $\sim 1.4 \times 10^{-3} eV^2$.

This region is interesting in relation to the Kamiokande solution of the atmospheric anomaly [7] and has been also explored by the CHOOZ reactor experiment [8]. The result of this search will then be compared with the outcome of the $\nu_\mu \leftrightarrow \nu_\tau$ oscillation search. The sensitivity of the experiment is described by the

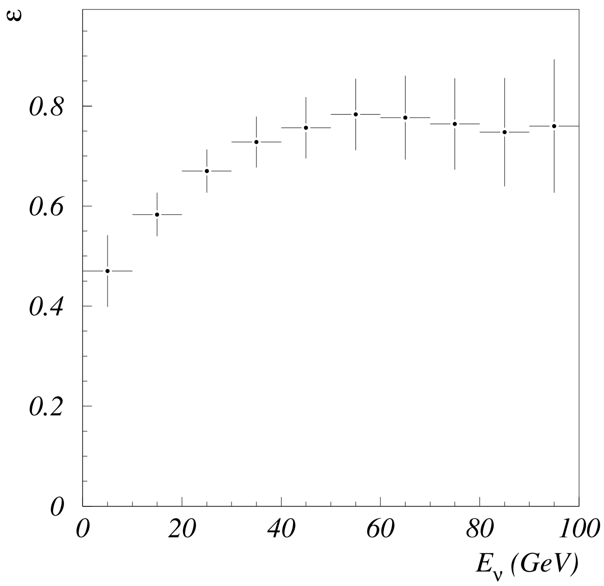

Figure 2.31: Electron identification efficiency for ν_e CC interactions.

exclusion plot shown in Fig. 2.32. The 4σ discovery contour is also shown, together with the results from various experiments.

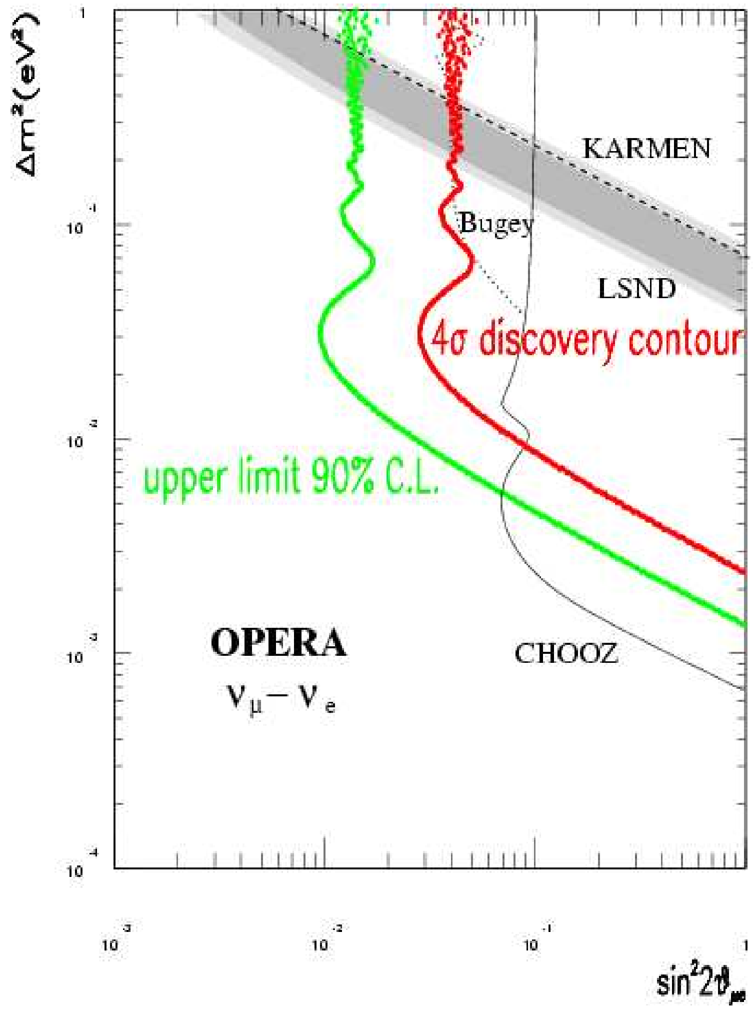

Figure 2.32: Sensitivity of OPERA in the search for $\nu_\mu - \nu_e$ oscillation. The 90% CL contour limit is shown together with the results of other experiments.

Chapter 3

The detector

3.1 Emulsions

3.1.1 Machine-coated emulsion sheets (MES)

The total area of emulsion sheets needed for OPERA could be as large as $\sim$ 200000 m^2. This would correspond to $\sim$ 20 m^3 of dried emulsion gel. For comparison, the large amount of emulsion handled in the case of CHORUS corresponds to 500 m^2 or a total volume of dried emulsion of 0.4 m^3.

The emulsion sheets used for CHORUS were poured by hand following standard procedures developed in many years of experience. The procedure lasted about six months involving several skilled people. The same operation would be prohibitively time consuming when applied to OPERA.

To overcome this problem, an R&D project is jointly being carried out by the Nagoya University and the Fuji Film company in Japan. The aim is to establish the process of machine coating of nuclear emulsion sheets (hereafter Machine coated Emulsion Sheets will be referred as MES) in order to deal with the large total surface which is needed.

For machine coating dilution of the gel is required. Under normal conditions, the grain density decreases almost linearly by dilution, although there is a sensitivity regaining process in the development. Fuji Film has solved this problem by increasing the sensitivity of each crystal utilising the current technology of crystal growth developed for normal photographic films.

The currently achieved grain density of the MES with a factor of two dilution is $\sim$ 30 grains/100 μm, which can be compared with 34 grains/100 μm for ET7B (without dilution) used for CHORUS and $\sim$ 28 grains/100 μm for ET7C (without dilution) used for DONUT. This sensitivity ensures the good operation of automatic scanning system.

We have performed test measurements with MES. The emulsion layer thickness is 50 μm on both sides of a plastic film of 200 μm thickness. The MES has a protection gelatin layer of 1 μm thickness on the sensitive layers (Fig. 3.1) which prevents the occurrence of black or gray spots on the film. These spots are due to deposited silver and are normally observed in hand poured emulsion sheets. To removeme these black spots was the most time consuming task in the emulsion pre-processing for the experiments performed so far.

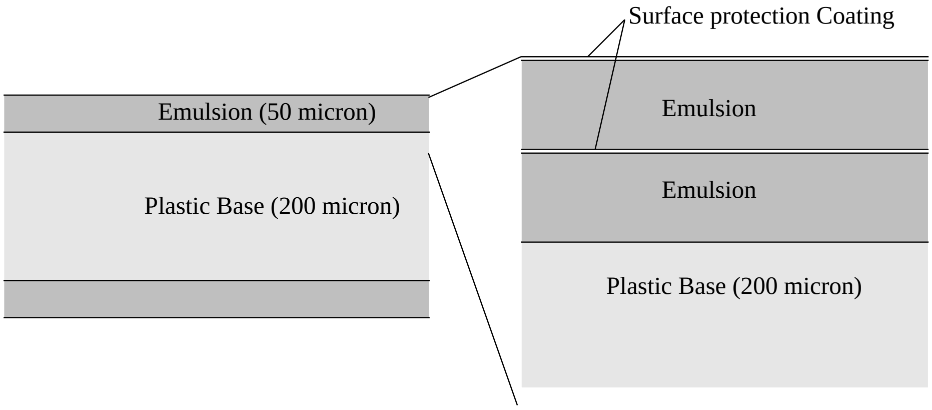

Figure 3.1: Schematic view of the cross section of MES. Diluted emulsion layers of 50 μm thickness are coated on both sides of a 200 μm thick triacetate film. One emulsion layer is formed by a two-step coating process of $\sim$ 25 μm each time. Thin ($\sim$ 1 μm) protection layer (gelatin) is coated over the emulsion layer at the same time of the emulsion coating.

In addition, the presence of this protection layer allows to make direct contact with the metal plates. Without protection layer, one would have to insert thin insulator sheets in order to avoid chemical reactions between the plates and the silver halides contained in the emulsion.

After several preliminary tests, Fuji has performed large scale production tests by using a line for photographic film mass production. As a result, they envisage a MES production rate of $\sim$ 10000 m^2 per month for a production of $\sim$ 100000 m^2.

Another important issue related to the present studies on the MES is the aging of the emulsion sheets. There are two aging sources: the degradation of the sensitivity and the fading of the stored image. Fading is not a severe problem for the experiment, since we plan to extract and develop the brick emulsions soon after an event occurred. Moreover, the existence of some fading could contribute to erase unwanted cosmic ray tracks accumulated during the pre-processing stage (MES production and transportation) before the run. This feature will be beneficial to suppress fake decays, the degradation of the electron identification efficiency and to keep adequate energy resolution for cascade showers. On the other hand, degradation of sensitivity has to be avoided or reduced to a level to ensure five years' running or more.

Fuji has been performing accelerated aging tests in order to obtain experimental results within a reasonable amount of time. Their present advice is to keep the environmental temperature at about 5^oC, as previously done for the CHORUS emulsion target. This condition would prevent the degradation of sensitivity. This requirement implies the need for temperature control (see also Section 3.5.2) of the emulsion target or of the experimental area.

Fuji MES have been employed in the test beam measurements presented in Section 5.1.

3.1.2 MES handling and transportation

After pouring, MES will have to be cut to the desired size and packed into air and light tight packages, prior to the transportation to the site where the assembling of the brick will be done (*e.g.* in the Gran Sasso Laboratory). Adopting an emulsion sheet size similar to that of present commercial or industrial X-ray films would minimise the extra labour needed for cutting and packing. At present, the size of the test MES is tuned to be 4×5 inches squared.

A production of 40000 cut and packed MES per day allows to produce the amount needed for OPERA in about two years. This value seems to be reasonable for existing cutting machines used for mass production.

The transportation of the MES is also an issue to be considered. The idea is to pack the MES immediately after their production in a package which will contain all the sheets needed for a brick. The brick will be built by keeping the relative position of the MES in the package. This will allow to reject track segments related to cosmic rays and reduce the amount of detected single track segments. The latter could, in fact, make the scanning procedure more complicated and could degrade the data quality. In addition, ground level (sea) transportation can be considered in order to avoid the hadronic components of cosmic rays, which can create black dirty tracks in the MES. As previously discussed, the above strategies against cosmic ray accumulation can be strongly relaxed if one could control the emulsion fading.

3.2 Target bricks

3.2.1 Passive material

Lead has high density and therefore optimises the interaction probability for a given plate thickness and for a given amount of emulsion.

The absence of radioactivity and the better mechanical properties, like the higher planarity, also leaves iron as a possible option. Iron has a lower price per kilogram than lead. However, if one wishes to keep the same amount of neutrino interactions, about 30% more emulsions are needed to compensate the difference in density, making the iron option globally more expensive. Normal iron is corroded by water and air, implying the need of adequate surface treatment. Stainless steel could be used, but with a cost about three times higher.

The main requirements for the spacer material are a low density, adequate mechanical properties and a low radioactivity. Several possibilities have been envisaged: Rohacell, PVC, polystyrene foam, paper honeycomb. For all these materials, the density is lower than 35 kg/m^3, *i.e.* within the experiment requirements. We performed test measurements on prototypes. Satisfactory results have been obtained with Rohacell and polystyrene foam, the latter being about five times cheaper. Rohacell density is 31 kg/m^3. With polystyrene one could reach 25 kg/m^3. Since density uniformity is also an issue, honeycomb structures does not seem to be an appropriate choice.

3.2.2 Brick assembly

The number of bricks to be constructed for OPERA can be as high as 150000. This large number necessitates an automatic assembly line. Several solutions can be envisaged for brick packing. The final choice will be dictated by practical requirements like good mechanical properties (brick handling), low density, small wall thickness and light tightness. The adopted solution will also depend upon the chosen support structure and upon the actual type of brick which will be used (weight and dimensions).

We performed tests to assess the properties of various solutions. A simple solution consists of paper envelopes for vacuum packing and metal strips to ensure mechanical stability. Another solution could make use of polypropylene boxes made of $\sim 2\ mm$ thick plates. This material is rigid and light ($1\ kg/litre$). Moreover, it allows ultrasonic welding by an automatic assembly line. The boxes are well suited to be handled by a robot for installation and removal.

The accuracy in positioning the elements of the brick (metal plates and ES) must be aimed at a mechanical precision of the order of $100\ \mu m$.

3.2.3 Brick production

We aim at a production capability of the order of one brick per minute so that all the bricks could be produced in $1 - 2$ years. This will be achieved by employing several assembly machines in parallel capable of adequate mechanical tolerances in the assembly of the brick components. We have established contacts with companies in the field of industrial automation. The first indications are positive. A dark room for brick assembly in the Gran Sasso Laboratory will be needed.

3.3 Electronic target trackers

3.3.1 Scintillator strips

Scintillator strips are the baseline option. The single strips are $25\ mm$ wide, $9\ mm$ thick and $50\ cm$ long. They have two grooves to accommodate the WLS fibres. The strips can be produced by the injection moulding technique. Granulated polystyrene is used as a base material with the two dyes (1.5% of PTP and 0.01% of POPOP). Each strip has a reflective coating except for the grooves.

Individual strips with length limited by the moulding technique are fixed onto an aluminium plate to form 16 rows of the required length. The fibres are glued into the grooves and routed to optical connectors at the edges of the plate. A plastic cover is placed on top and all sides are then made light tight. The ribbon optical cables carry the light from optical connectors to the photo-detectors.

The target tracker unit is a plane of octagonal shape of $6.4\ m$ from side to side. It is composed of 256 rows of strips. Two such planes with orthogonal strip orientation are placed downstream each target wall. Fig. 3.2 shows the layout of a plane with the fibre readout.

The WLS fibres are double clad fibres with a diameter of $1.2\ mm$. One of the two fibres of a row of strips is read out from both ends. It is used for pulse height measurements (*signal fibre*). The other one is read out from only one end. It is used for triggering (*trigger fibre*). The far ends of trigger fibres have a mirror to increase the effective attenuation length.

The target plane has eightfold multiplexing to the photo-detector. Eight even trigger fibres within a module are coupled to a single PMT pixel on one side of the module. Eight odd fibres are coupled to a PMT pixel on the other side. A total of 32 pixels (16 per side) are required for triggering. Each eight signal fibres spaced by $70\ cm$, one from each of eight modules, are coupled to a single pixel. A total of 64 pixels are required to readout a plane (32 per side). The combined patterns of trigger and signal pixels determine unambiguously the strips which are hit.

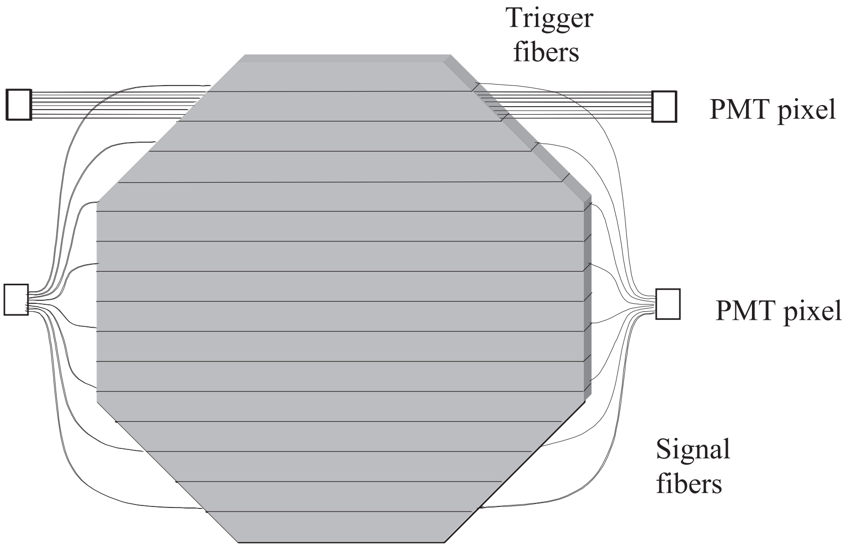

Figure 3.2: Tracker plane layout and sketch of optical readout.

The design goal for the tracker plane is to achieve an efficiency greater than 97% for detection of minimum ionising particle (*mip*). To ensure this efficiency, the number of photo-electrons (*p.e.*) per *mip* at normal incidence must be at least 5. The light yield depends on the light output of the strips, on the light collection efficiency, on the PMT and on the fibres. The key parameter of WLS fibre is its effective attenuation length. In the range of fibre lengths used in the tracker plane, double clad fibres which are commercially available from BICRON and KURARAY are suitable to meet the requirement. Fig. 3.3 shows the expected light yield at each side of the plane and the sum of signals from both sides. The calculations are based on the effective attenuation length of BICRON BCF91A fibres as measured by the MINOS experiment [23] (up to 7.5 m). The absolute scale is taken from measurements performed with prototype modules.

3.3.2 Liquid scintillator option

An alternative target tracker option foresees the use of liquid scintillator as active detection medium. Mineral oil scintillator detectors have been widely used in experiments. E734, KARMEN, LSND and MACRO are a few examples. A fully active liquid scintillator detector based on a design similar to the one described for the tracker planes, has been considered in the studies related to the I216 Letter of Intent [52] and in studies for a long baseline neutrino oscillation experiment [53].

Liquid Scintillator Trackers (LST) are made up of WLS fibres inserted in long cells filled with liquid scintillator. One LST is positioned downstream of each wall of emulsion bricks. A LST is made up of two consecutive planes, with a size matching the target walls (*i.e.* $\sim 6.5 \times 6.5\ m^2$). One plane is segmented with horizontal and the other one with vertical cells. The orthogonal cell orientations allow for reconstruction in space. The design is identical for both orientations.

Each plane consists of a series of 650 parallel cells of 1 cm^2 cross section. Planes are made of extruded, white polycarbonate profiles with dimensions of $1 \times 200 \times 650\ cm^3$. These profiles include thin separators every centimetre, thus defining the cell structure. Polycarbonate profiles can be extruded with a high

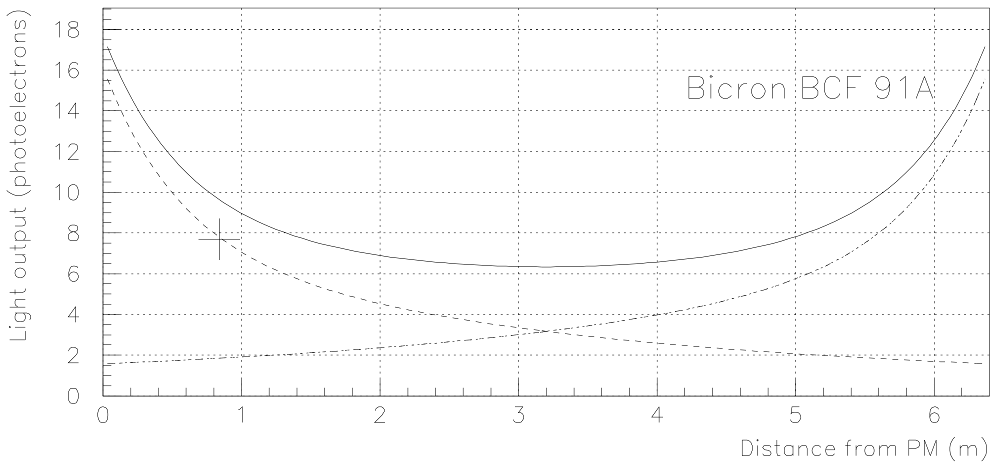

Figure 3.3: The expected light yield at each side of the plane and the sum from both sides. The point correspond to the test beam measurement.

reflectivity ($\sim$ 95%). The standard size is $2 \times 7\ m^2$ and the weight is $1.7\ kg/m^2$. The profiles are filled with liquid scintillator. The cell signal is extracted by means of a single WLS fibre, read out at either ends. The WLS fibres are bundled together and coupled to optoelectronics chains for readout.

By choosing the appropriate scintillating mixture one can expect to obtain more than 5 $p.e.$ per mip at the centre of the plane. The light yield of commercial mineral oil scintillator can vary from 20% to 65% with respect to anthracene. The necessary optimisation will be conducted by means of laboratory tests. Due to the local scintillation light capture and to the WLS conversion inside the fibre, a better optimisation of the liquid scintillator should be achievable compared to conventional implementations where a long attenuation length is required.

The WLS fibres have a diameter of 1 mm, the cladding is made of an acrylic material and has a thickness of about 15 μm. Their emission spectrum is centred at about 520 nm. They are coherently bundled before being pushed against the input window of the optoelectronics devices. The chemical compatibility of WLS fibres with mineral oil based scintillators has already been studied and various suppliers offer factory-tested products.

The optical signal produced at the end of the WLS fibre bundles is read out by means of connectors placed outside the liquid. The readout device is thus directly connected to the vessel signal outlet, minimising light losses in the optical coupling.

3.3.3 Photo-detectors

The baseline photo-detector option for the scintillator strips is the commercially available HAMAMATSU R5900-M16 16-pixel PMT[1]. The size of an eight fibres bundle matches that of the pixels ($4 \times 4\ mm^2$). A

[1]Hamamatsu Photonics K.K., 325/6, Sunayama-CHO, Hamamatsu City, 430, Japan.

total of six PMTs is required to equip a plane. That makes a plane-wise readout scheme. We also consider the 64-pixel PMT M64 from Hamamatsu with a twofold multiplexing scheme.

Another option is represented by HPDs from DEP[2]. HPDs would provide a better uniformity and linearity than the multi-anode PMTs as well as an easier coupling to VLSI front-end chips, which are already available for silicon detector readout. They have a typical gain of 10^3. Since they are also available with S20 photo-cathodes, they can reach a quantum efficiency of 20% at 520 nm, where the spectrum of the WLS fibre peaks. The low gain of the HPD would require a high gain pre-amplifier and a noise performance suitable to resolve the single photo-electron peak.

Due to the recent development of large size Avalanche Photo Diodes (APDs), we are also studying an alternative solution to the previously described fibre readout system. It foresees APDs attached to each end of the scintillator strips. Preliminary studies have been performed in a test beam. A signal to noise ratio of about 7 was achieved with a gain of about 50 at a voltage of 390 V. Further improvements are underway.

Another option is given by the Electron Bombarded CCD (EBCCD) [54] from GEOSPHAERA[3] which can be used for the readout of WLS fibres. Various gateable EBCCDs with photocatode diameter from 18 to 80 mm are available. They can accommodate from 512 up to 5180 1 mm fibres. The high spatial resolution allows to resolve easily individual fibres. The readout time of 100 ms is limited by CCDs. Several types of tubes with different CCDs were tested. Results are encouraging. The EBCCD looks very attractive for a liquid scintillator option, because of the large number of channels (fibres) which can be read out by a single device. The EBCCD could provide good gain uniformity, low cross-talk and single photo-electron detection capability. In Section 5.2 we will present experimental results on a test with EBCCD coupled to scintillator detectors.

3.4 Muon spectrometers

3.4.1 Toroidal magnets

Octagonal toroidal magnets are considered as a baseline option for the muon spectrometers. Their design must fulfil the resolution and acceptance requirements defined in Section 2.2.4. Each magnet is subdivided into 17 sandwiches, each made of a 3 cm thick steel plate and a 1 cm thick plane of plastic scintillator strips. These are mounted inside a 3 cm gap leaving space for the fixation system. The overall length of one magnet is 102 cm (Fig. 3.4). Two magnets are used to form a spectrometer. Its overall volume is $7.5 \times 7.5 \times 3.1\ m^3$ and its weight 400 ton.

In the following we give technical information about the steel specification, the steel plate assembly and suspension, the magnet coil and the magnetic flux density. The OPERA steel plates are similar in shape, size and magnetic requirements to those foreseen for MINOS. Extensive use has been made of the information available from the MINOS Technical Design [23] and the published NuMi notes.

The final choice of the carbon content in the steel will be the result of a compromise between tensile strength and magnetic properties. A carbon content in the range $0.04 - 0.06\%$ has been found adequate for the BABAR return yoke [55] and for the MINOS magnets [23]. The radioactivity in the steel will have to be kept low. Further specifications on thickness homogeneity and flatness of the steel plates will have to be defined.

[2]DEP Electronic Products BV, P.O. Box 60, NL 9300AB Roden, The Netherlands.
[3]Geosphaera Research Center, Moscow 117261, Russia.

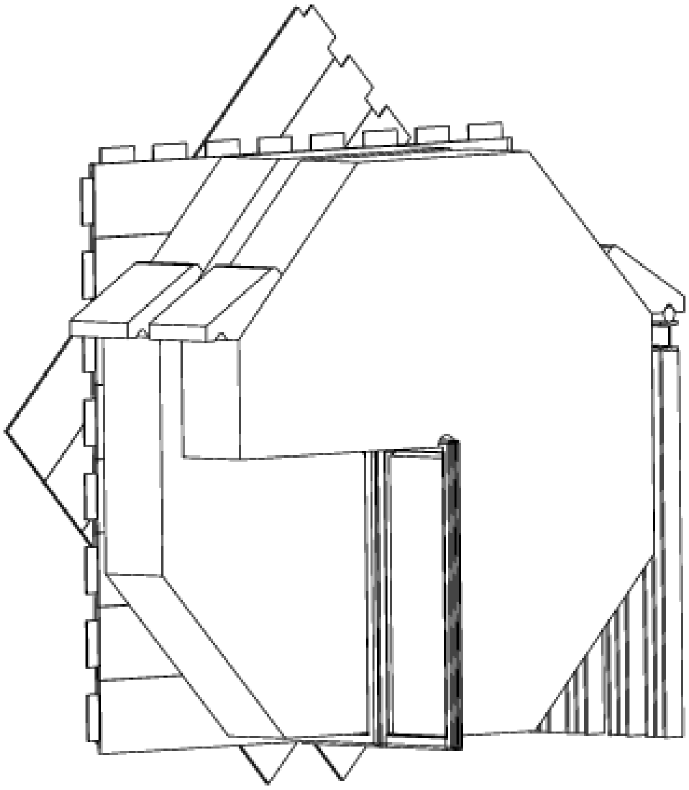

Figure 3.4: Layout of a muon spectrometer using two toroidal magnets. Only the back high precision tracker is shown for clarity. The two other trackers are placed betweeen the magnets and in front of the first. Only one of the two supporting structures is shown. A cut of the front magnet shows the coil.

Plates of up to 3.75 m wide and 3 cm thick with no practical length limitation can be produced by industry. Therefore, each steel plate could in principle be constructed by cutting and assembling together two 3.75 m wide and 3 cm thick plates. The total weight of a steel plate is 11 ton, giving 187 ton per magnet.

Other assembly schemes are being studied. We envisage the use of two layers made of 1.5 cm thick plates. The plates in one layer are orthogonal to those in the other layer. This criss-cross pattern could improve the flatness and result in an easier construction while insuring an equally good rigidity to the assembly. Fig. 3.5 illustrates these two schemes. In all instances, the steel plates will have to be welded inside the Gran Sasso cavern.

The following procedures are part of the plate assembly process which will depend on the chosen scheme and must be studied further:

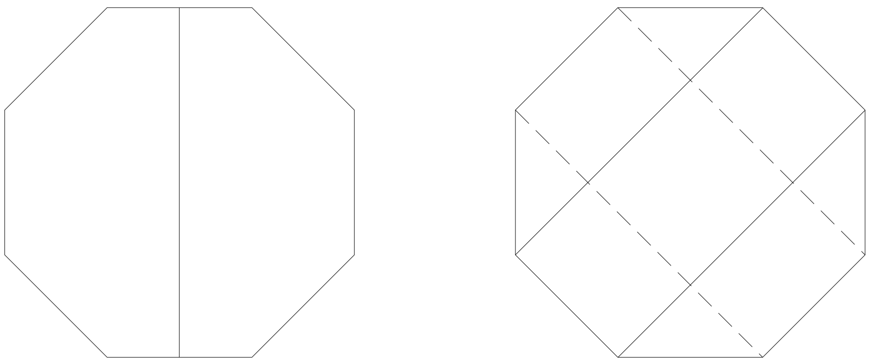

Figure 3.5: Assembly schemes of the toroid steel plates.

- an inexpensive way of cutting plates to their shapes, while insuring good edge straightness to avoid significant gaps between plates and thus distortion in the magnetic flux density;
- a technique to push plates together to reduce gaps and force them together as flat as possible during assembly;
- a plate bonding or welding process strong enough to support the shear strength caused by the plate own weight once suspended.

Various suspension methods are being considered. In the MINOS design, magnets hinge on support rails by extension ears placed above their centre of gravity and stabilised in position by axial restraints. This design is attractive in terms of mechanical stability and accuracy in positioning. The suspension has to be studied in relation to anti-seismic specifications. The installation procedure will depend on the chosen suspension method.

Each magnet has its own coil which induces a toroidal magnetic flux density of 1.5 T averaged over the surface of each steel plate. Fig. 3.4 shows a schematics of the coil, its return legs and its return base. The coil runs alongside the magnet at the middle of one set of octagon edges. Between the two magnets and their adjacent high precision trackers, space will have to be provided to host the coil legs. The coil goes through a 10 cm bore centred on the octagons. It delivers 15000 $A - turns$.

A calculation of the field map for the type of steel considered indicates that the magnetic field ranges between 1.6 T and 1.2 T, except in small areas near the corners. Fringe field effects, in particular on the nearby photo-detectors, will have to be evaluated. The details of the coil structure and the need for a coil cooling circuit have to be investigated.

The magnetic flux density must be known with an accuracy better than 10% in order not to contribute significantly to the momentum error. The coil current will be registered during data taking. The need for separate monitoring of the integral magnetic flux in each steel plate will be addressed by comparing the calculated flux density map with measurements of the first steel plates that will serve for the magnet prototype.

3.4.2 Dipolar magnet option

An option for the spectrometers foresees the use of dipolar magnets. The design presented here is preliminary and will be subject of forthcoming studies. The general detector scheme is shown in Fig. 3.6. Each of the spectrometers consists of a warm magnet of rectangular cross section providing a magnetic field of 1.5 T. The field lines are perpendicular to the beam direction.

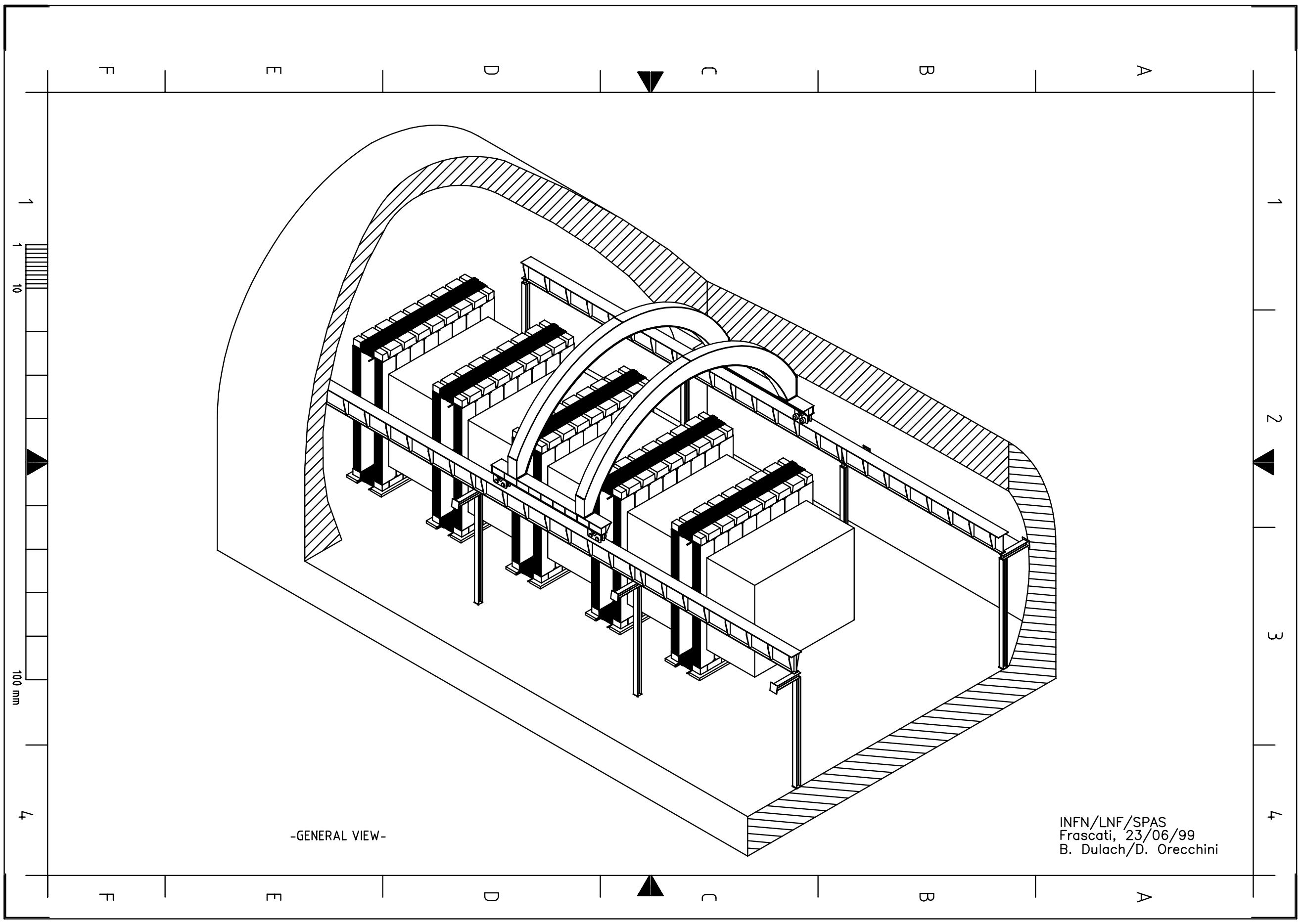

Figure 3.6: Detector setup with dipolar spectrometers.

Externally, the iron is 2.76 m long, 8.48 m wide and 8.86 m high. The 2.76 m length is given by two multi-layers of 0.88 m each, with a free internal space of 1.0 m in between (Fig. 3.7) to allow for insertion of tracking detectors. The free space is defined by the required momentum resolution. In the present design, each multi-layer is made of 10 iron walls 40 mm thick and 14 cells 20 mm thick to house the detector planes (Fig. 3.7).

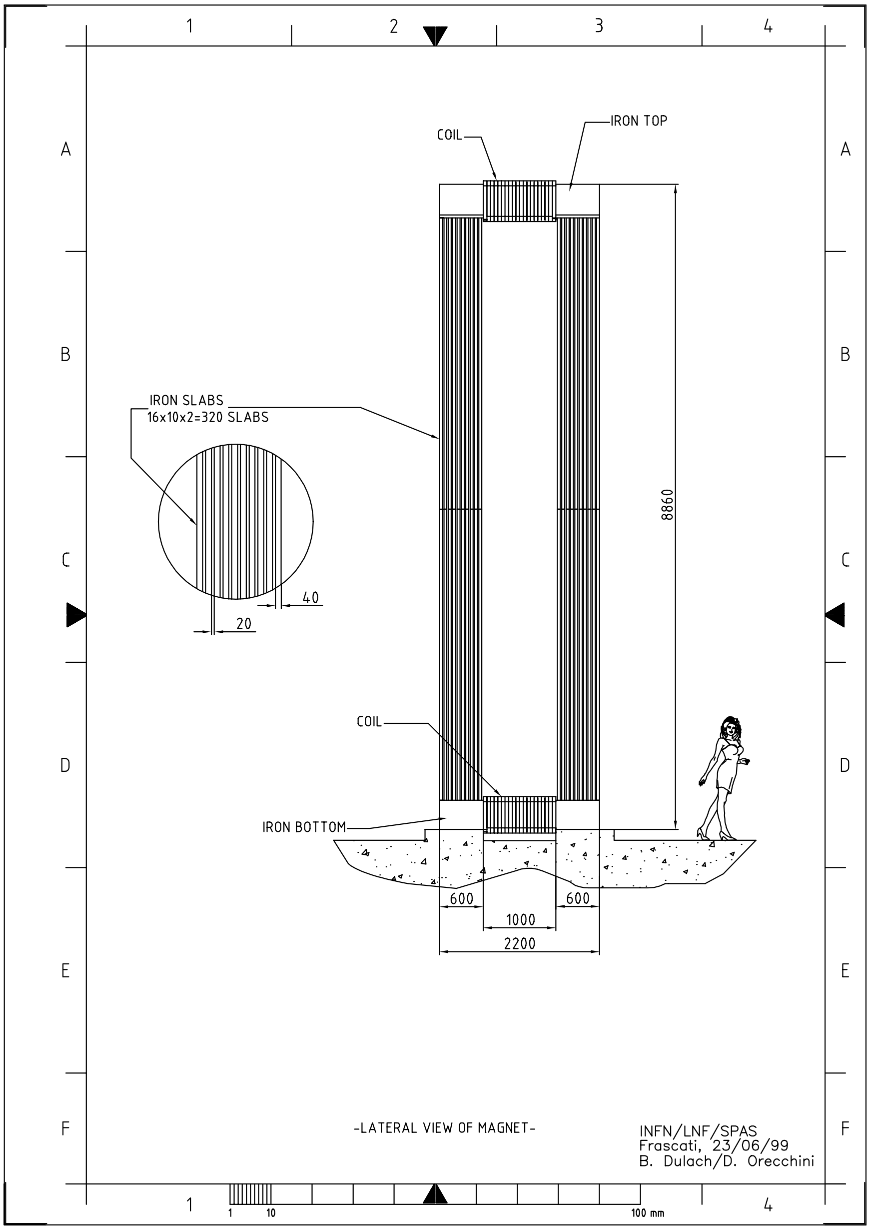

Figure 3.7: Dipolar magnet (side view).

The total weight of one magnet is about 800 ton: 150 ton for the top and bottom flux return path and 650 ton for the tracking volume. Each iron wall is made of 16 iron slabs $40 \times 1000 \times 4000\ mm^3$ to be assembled on site for a total of 320 slabs per spectrometer. The slabs are precisely machined along the two short sides (1000 mm) and have holes for bolting and lifting and slots for cables. They can be stitch welded on the vertical (horizontal) spacers or bolted.

The iron envisaged is a spin casted unalloyed quality steel with magnetic properties of the type Fe GM01 UNI 3595. The relative permeability is $7 \times 10^{-4}\ Hy/m$, for an average magnetic field of 1.5 T, well below saturation.

A preliminary field map has been obtained verifying a homogeneity of the wall magnetisation of 1 % and a fringe field of 10 G at a distance from the edge of 10 cm. The study of the magnetic field is in progress.

In order to simplify the construction and the operation, the coils have low current density and air cooling. Two symmetric coils are wrapped around the top and the bottom flux return paths. The turns are made of copper bars (type Cu-HCP UNI 5649-1) $80 \times 15\ mm^2$; their resistivity is $0.017\ \Omega \times mm^2$. The current density is 1 A/mm^2. The total current is 1200 A, obtained with 46 turns (23 per coil). The total length of the conductors is 810 m; the weight is 10 ton. The total resistivity is 0.011 Ω, the voltage 14 V and the power 16.5 kW.

3.4.3 Scintillator strips

Scintillator planes are formed by 3 cm wide strips. The strips in two consecutive planes are alternatively arranged horizontally and vertically (Fig. 3.8). Strips are staggered from plane to plane by half a strip width. They are equipped with wave length shifting fibres read out at each end by multi-pixel analog photo-detectors in much the same way as for the target trackers. The 3 cm width of the strip is limited by the light collection in the WLS fibre. With such a granularity the resolution on the muon energy measured by range is about 5%.

The WLS fibres are read out at one end while a mirror is sputtered on the other end. Simulations indicate that with a typical mirror reflectivity of 80% and light attenuation properties similar to the target scintillators, the relative light output from such a 3.45 m long strip compared to a 7.5 m long strip read out at both ends varies from 90% at the mirror to 106% at the photo-detector. A typical mirror reflectivity of 80% with 0.5 mm diameter fibres has been achieved by CHORUS [17].

For the toroidal design, strips have lengths between 3.1 and 7.5 m in order to approximately match the octagonal shape of the detector. Central strips are split into two pieces to leave space for the coil. The number of strips per plane is 248 and they cover the area of about 46 m^2. One magnet contains about 4220 strips and the entire detector (five spectrometers) $\sim$ 42200 strips, coupled to about twice as many readout channels. The plane is composed of 31 light-tight sleeves with 1 mm walls, each containing 8 strips. 9 sleeves at each side form a trapezoidal part of the plane and 13 central sleeves, the rectangular part. The sleeves will be produced at the same time as the steel plates and attached in position to their upstream steel plate before lifting for installation on the detector. Practical details of the installation procedure have to be studied.

3.4.4 Tracking detectors

The precision of the spectrometer tracker measurement has to be better than 1 mm over the whole transverse area of the spectrometer ($\sim 50\ m^2$). Furthermore, this condition has to be achieved *by construction* since in the underground cavern one cannot rely on an alignment by cosmic ray or beam-related muons.

Further desirable features of the muon tracker are: high single track detection efficiency, reasonable multi-hit capability for multi-track measurements, no angular dependence of the position measurement, no use of toxic materials and flammable gases, immunity against neutrals (gammas and neutrons) produced in showers developing in the target section and leaking into the magnet. Since the track pattern recognition and the muon idententification are entirely delegated to the coarse scintillator strip tracker described in the previous Section, the granularity of the precision tracker should match the spatial resolution of the strips ($2-3\ cm$). A finer granularity with the same space resolution will only lead to larger number of readout channels and may worsen the detection efficiency.

These considerations led us to 3 cm wide cylindrical proportional-drift tubes as a baseline option for the muon tracker. As a prototype, we shall use ATLAS Monitored Drift Tubes (MDT) [58] and benefit from their well understood performance, manufacturing technology and availability of the readout electronics design.

ATLAS MDTs have a design resolution of 80 μm per tube, thus offering a comfortable margin for downgrading them to achieve a maximum cost reduction, while keeping the global spatial resolution at a level of 500 μm per multi-layer. The MDT features to be retained are: the tube construction (including end-plugs); wire diameter, its material and stretching without spacers; the wiring machine; the gas mixture ($Ar{:}N_2{:}CH_4$=91:4:5) and proportional operating mode; the front-end electronics. Downgrading of the MDTs can be achieved by: commodity extruded tubes with thicker walls and looser tolerances; restricted number of basic tube lengths; a simpler support structure; relaxing the stringent requirements on the assembly precision; operating the chambers at atmospheric gas pressure.

The drift tube chambers here considered (Fig. 3.8 and Fig. 3.9) is a square multi-layer of 3 layers, glued to a flat supporting base. All chambers have a unique size of $L \times L\ m^2$, where L is the magnet side-to-side width plus 14 cm (two times the lower efficiency region at both ends of the tube). The multi-layer can consist of two halves joined together during the spectrometer installation. Rotated planes have a corner carved from the bottom apex to match the clearance between the detector and the floor.

For sagitta measurements with octagonal magnets, there will be three stations (upstream, medium and downstream), each having 3 multi-layers rotated $w.r.t.$ each other by 45 degrees. In five 7.5 m wide spectrometers with 3-layer multi-layers, we will have $\sim$ 34000 tubes (about 8% of the ATLAS MDT system).

For a dipolar magnet option with a horizontal bending plane, the required accurate positional measurement can be achieved with (only) vertical multi-layers of $4-5$ rows of tubes at front and back sides of the magnet. The vertical coordinate can be measured (with lower precision) by the coarse trackers in the magnets.

As an alternative option for the muon tracker, we are considering plastic streamer tubes with combined wire (digital, drift time) and orthogonal cathode strip (analog) readout. This well established technology has been used in detectors of similar size. In ZEUS [56], a local resolution of 290 μm across the wire and 760 μm across the 13 mm wide strip has been achieved. However, to achieve a sub-mm precision, the wire and strip positioning accuracy should be not worse than 500 μm. In order to cope with safety regulations,

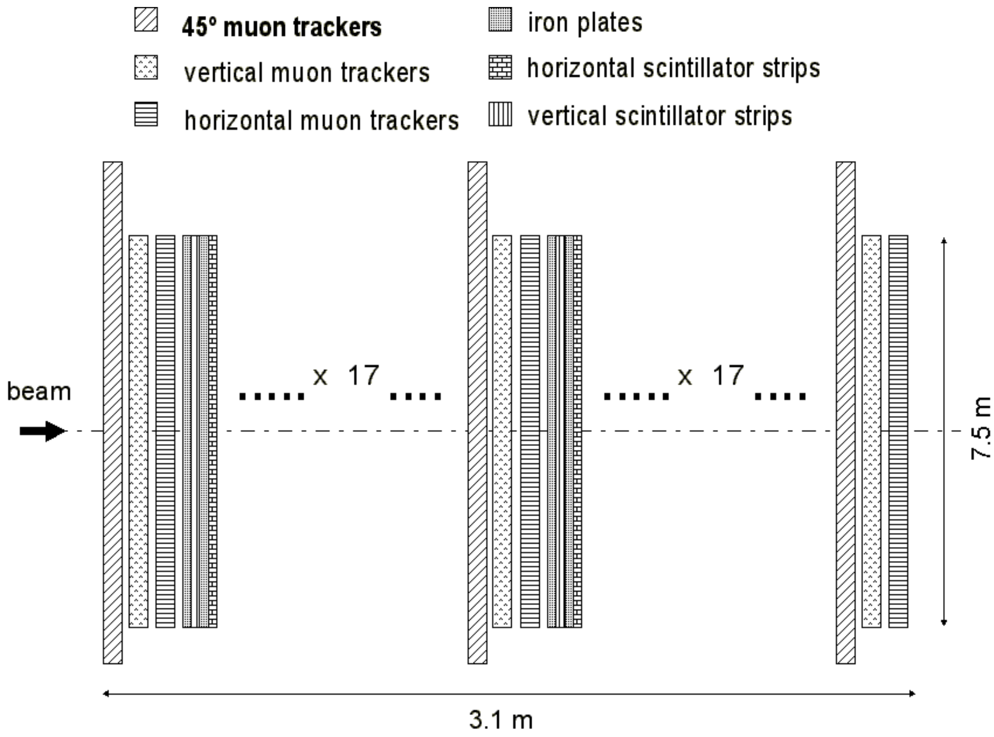

Figure 3.8: The longitudinal structure of the toroidal muon spectrometer (the coils are not shown).

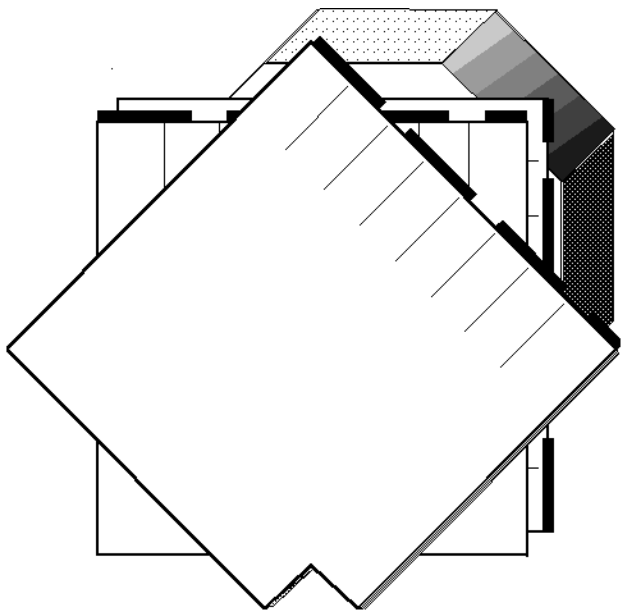

Figure 3.9: Schematic isometric view of the muon tracker. Black bars correspond to readout sides.

the plastic bodies of the ZEUS chambers are made of Noryl ENV509, rather than of PVC. Such chambers can be ordered from industry (*e.g.* POL.HI.TECH, Carsoli, Italy).

In the case of the toroidal magnets, each streamer tube tracker is made of four projection planes, two adjacent planes staggered by half a tube width with the wires running vertically, and two at 45 degrees. The plastic streamer tubes will be produced in different lengths between 3.1 and 7.5 m, in order to approximately match the octagonal shape of the detector. The planes with vertical wires are equipped with analog strips, while those at 45 degrees are not. The number of wires is 751 per plane, 3004 per tracker and 9012 per spectrometer. The corresponding numbers of strips are 501, 1002 and 3006.

Another possible scheme envisages each tracker made of six projection planes, two adjacent planes staggered by half a tube width with the wires running horizontally, two vertically and two at 45 degrees. The planes in this case are not equipped with analog strips. The number of wires is 751 per plane, 4506 per tracker and 13518 per spectrometer.

Methods of assembling tubes into chambers, profiles, planes and trackers with the required positioning accuracy are under study. We consider to embed the planes structure between two honeycomb layers which constitute a rigid and light backbone for each tracker.

3.5 Brick handling and infrastructures

3.5.1 Brick support structure

We have started the engineering study of the detector assembly by considering different solutions for the brick support structure. The solutions envisaged are in principle suitable for both compact or spacer bricks as well as for the two proposed spectrometer options.

The following requirements have to be fulfilled by the engineering implementation of the detector. The support structure has to guarantee sufficient precision and easy access to the bricks to be removed in order to have the possibility of quasi-online analysis, *i.e.* the extraction of the bricks fired during the beam exposure. The dead space between bricks should be limited, specially with regards to the brick-to-brick event connection. A light structure minimises the neutrino interactions ouside the active area. The structure has to be reliable, cost effective and stable in relation to the movement of bricks (walls). Easy access to the front-end electronics has to be guaranteed.

A possible scheme envisages to assemble rows of bricks in horizontal or vertical *wagons* (brick containers) which become a sub-unit of the installation. In the case of vertical wagons a wall consists of several pipes which are upright aligned as shown in Fig. 3.10. The wagons are installed in the vertical pipes like totem-poles. The total weight of a column is supported by a thick I-beam installed below the wall. In principle, the wall only acts a guide not as a weight supporter.

The above scheme could allow for brick removal without displacing the entire wall. Only light objects (of no more than $\sim 100\ kg$) are moved for each intervention. In this approach, the alignment of the wagons is decoupled from their general support, allowing the replacement of the bricks at any time without affecting the position stability of the general support structure. Online access to the fired bricks can be performed by robots. A supermodule incorporating the above assembly scheme is schematically shown in Fig. 3.10.

Another scheme, depicted in Fig. 3.11, shows a similar implementation done with horizontal wagons. A wall of horizontal wagons consists of long pipes aligned horizontally with the wagons installed inside the pipes. The total weight of a row is supported by the pipe which is glued or welded to a 1 mm thick stainless sheet. This sheet hangs on a thick beam which is installed on the general support, as shown in Fig. 3.11.

Figure 3.10: Schematics of a target supermodule assembled with the *vertical wagon* scheme.

A different approach foresees to place the bricks into a support matrix made of stainless steel strips (*harp*). In this case, bricks are installed in shelves directly at the front wall surface as shown in Fig. 3.12. The weight of a brick is supported by the bottom plate of the shelf and the brick column by two adjacent vertical stainless strips which are vertically stiffened. In this scheme, one has access to the individual bricks by displacing the entire wall either sideways or longitudinally.

The main difference between the wagon and the harp assembly schemes is given by the target part (*i.e.* a wagon or a wall) which has to be moved in order to access a fired brick. The weight and the number of bricks affected by this movement are very different for the two schemes: $\sim 100\ kg$ and several tens of bricks

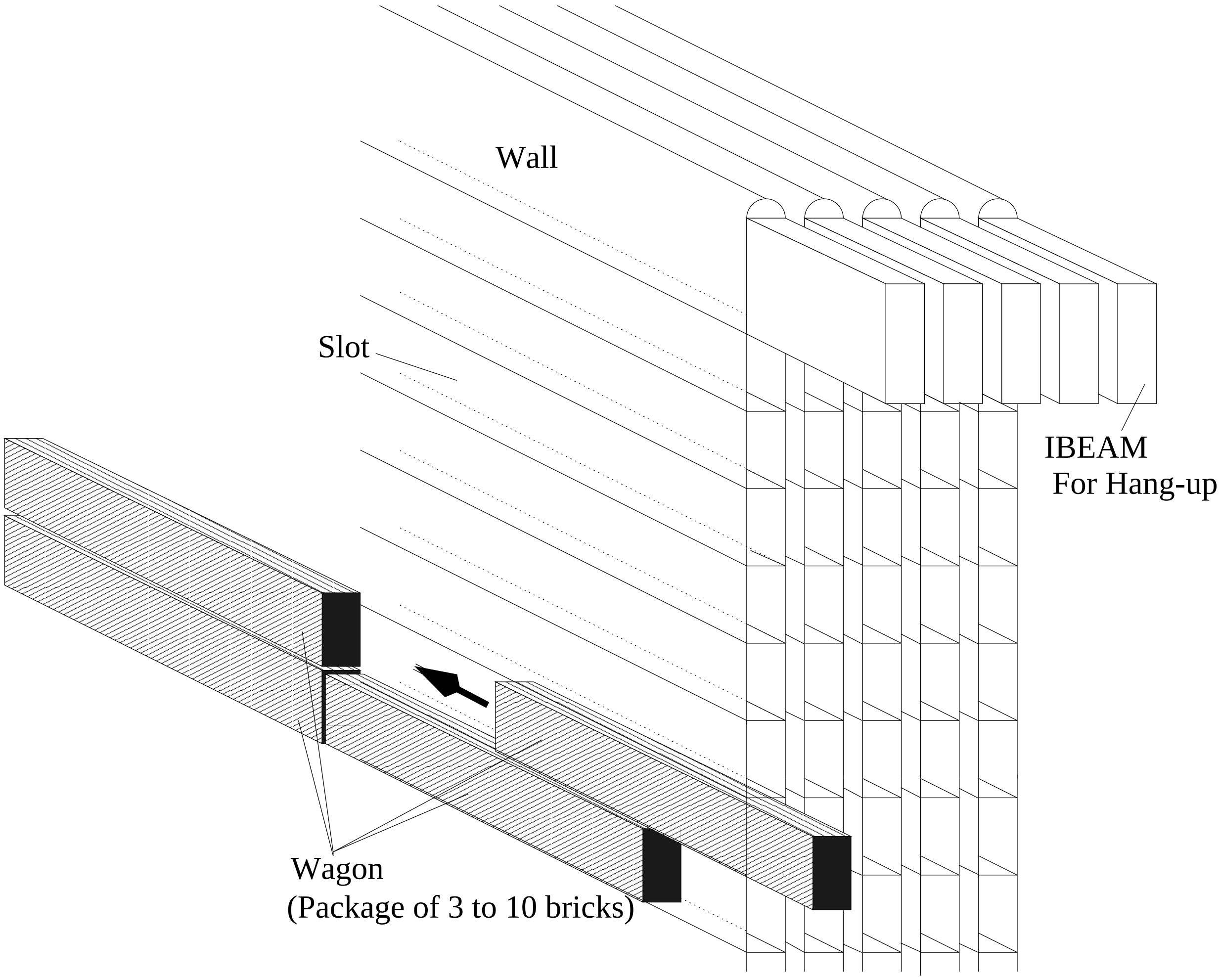

Figure 3.11: Schematics of a target supermodule assembled with the *horizontal wagon* scheme.

in the case of wagons and ~ 10 *ton* and several thousand bricks for the harp. We point out that the harp option requires brick removal during beam-off time or stopping data taking.

Designing and prototyping works for each of the above versions are underway. The actual detector structure (or a combination of them) will be defined following the evolution of these developments and of test measurements.

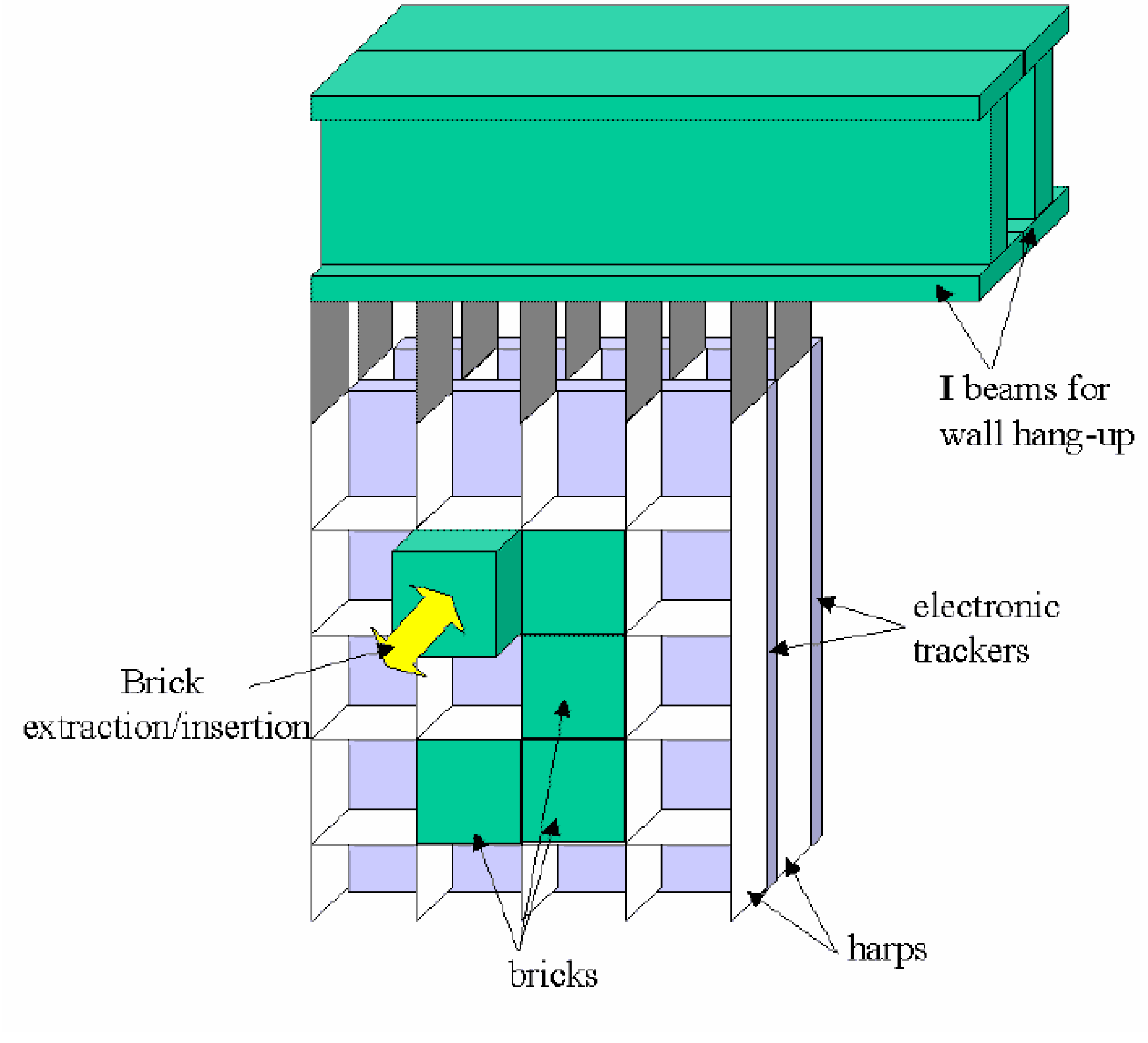

Figure 3.12: Detail of the *harp* support structure for two consecutive modules.

3.5.2 Environmental control and handling of removed bricks

The temperature around the emulsion target must be well controlled in order to reduce the thermal expansion and the emulsion shrinkage during the run. We refer to the experience of CHORUS [17]. In CHORUS the

~ 1 *ton* pure emulsion target was kept at constant temperature $(5 \pm 1^0 C)$ by placing it in a cool box.

In the case of OPERA, the machine coated emulsion sheets have a heat expansion coefficient of $\sim 8 \times 10^{-5}$. The temperature has to be then stable within ± 1 degree.

In addition, the fading process, namely the potential loss of the latent image before development and the aging effect of the sensitivity are a function of the temperature. Fuji advices to keep the detector at $\sim 5^0 C$ as done for CHORUS.

For the handling of bricks after removal, a dedicated laboratory will have to be set up at the Gran Sasso. Room temperature and humidity will have to be controlled, since the dimensions and shape of the emulsion sheets are affected by the ambient humidity. This dependence has not yet been checked for the MES. However, some difference with respect to previously used emulsion gel can be anticipated due to the larger gelatin content in the MES and to its different treatment. According to the experience with CHORUS we think of a relative humidity of $70 \pm 5\%$.

During the run, the fired bricks are removed from the support and unpacked. A precise map of fiducial marks and number code is then printed on all the emulsion sheets for internal reference and sheet identifier. During this operation, the temperature in the brick handling facility must be kept at the same temperature of the detector, *i.e.* $5^0 C$. Also in the likely case of brick exposure to cosmics for alignment purposes one has to provide a suitable transportation with controlled temperature and humidity.

A separate facility is required for the development of the emulsion sheets. Automatic development machines will be realised which are modified versions of the present automatic machine for X-rays films. The expected development capability should follow the event rate of 20 events per day ($\sim$ 1000 ESs per day). It is an advantage to have this facility in the underground laboratory.

The characteristics of the laboratories needed for the above facilities will be defined after the foreseen test programmes with prototypes.

Chapter 4

Data processing

4.1 Emulsion scanning

4.1.1 General features

For a five years' run, the total number of neutrino events collected by OPERA would be about 25000 including both CC and NC ν_μ events. This number in itself is much smaller than in CHORUS and could appear negligible from the point of view of the scanning load. However, in OPERA the scanning procedure is much more time consuming and will require further R&D work on the scanning systems.

Given the small number of events (of the order of 20 per day), one can periodically remove (and possibly replace) those target bricks where the events occurred and perform the emulsion scanning. This scheme reduces the relevance of the emulsion fading, thereby allowing a long running period.

4.1.2 Emulsion scanning procedure

In order to locate the neutrino interaction vertex in the brick, procedures similar to the one presently studied for the *Net Scan* R&D work will be applied. At first, the most downstream ESs of the brick are scanned. All the track segments within the angular acceptance ($e.g. \sim 400\ mrad \times 400\ mrad$) are pickedup (*general track pick-up* procedure). These track segments are then followed to the upstream ESs until vertex candidate(s) is(are) found (*scan back* procedure).

The time consuming scanning procedure is the *Net Scan* work. The time needed for track following is comparatively short due to the small expected number of tracks. It is short even considering the penetrating tracks which will be needed for ES alignment by exposure to cosmic-ray muons.

According to simulations, the area to be scanned depends on the brick type and on the performance of the electronic trackers. This has been discussed in Section 2.2.3 and test measurement results will be presented in Section 5.2. Even in the best case, the scanning area must be a circle with radius larger than 3 cm (2 rms). In order to keep high location efficiency an area of at least $\sim 50\ cm^2$ (corresponding to a radius of 4 cm) has to be scanned for the most downstream ESs.

In order to perform a quasi-online analysis, the event location speed has to follow the interaction rate ($\sim$ 20 events per day). The speed of the scanning system must be high enough to allow scanning of an area of $20 \times 50 = 1000\ cm^2$ per day. The development of automatic scanning systems has been outlined in Section 1.2.3. The aimed scanning speed of the Super UTS amounts to $\sim 10\ cm^2$/hour/machine. Therefore, about five Super UTS could stand the scanning load of the experiment. This strongly motivates the interest in developing the Super UTS and, possibly, even faster systems.

Event vertex candidates are identified as the point where more than two tracks are converging or where a single scan-back track stops. For each vertex candidate, the *vertex confirmation* scanning is applied, by performing a *Net Scan* to the restricted volume around the vertex. This allows, in turn, to identify additional meeting tracks or parent tracks. If a parent is detected, it is then followed upstream. If there is no parent and the vertex is validated, the decay search procedure starts by using the track segments picked up by the *restricted Net Scan*. The above sequences are analogous to those described in Section 1.2.3. The polishing of the off-line programs is in progress, profiting from the real analysis being carried out for the DONUT and CHORUS experiments.

As already pointed out, decay candidate events undergo a detailed analysis involving the determination of the relevant kinematical quantities. All primary vertex tracks have to be followed downstream (momentum measurement and particle ID) sometimes for several consecutive or adjacent bricks.

4.1.3 Development of the multi track approach

Groups of the OPERA Collaboration are following the approach of the so-called Multi Track Systems (MTS). In the following we present the SySal system [57] developed by the Salerno Group and the R&D underway by the Naples and Münster groups. Similar studies are being made in CHORUS by the CERN and NIKHEF groups.

In SySal all tracks in each field of view are reconstructed regardless of their slope, provided they are within a region of angular acceptance. A design goal of the system is to reconstruct tracks at the level of single grains, thus extracting from the emulsion the highest amount of information. The process of reconstruction and the representation of the tracks mimics very nearly the human way of recognising a particle track in emulsion. This facilitates to setup the system under different working conditions.

Particle tracks are given by a regular sequence of grains of metallic silver. The *raw data* are series of tomographic images of the emulsion, taken with the objective moving at regularly spaced depth levels (1.5 to 3.5 μm). A fast high-resolution camera (1024×1024 pixels, 30 Hz) with an electronic shutter (0.1 to 2 ms) sends each image to a frame grabber. There, it is converted to a matrix of gray-scale pixels (256 levels, 8 *bit* per pixel).

The first step for 3D tracking in emulsion is the recognition of grains. A digital filter is used to *clean* each 2D image. Its purpose is to enhance the dark spots with the expected size and shape and to suppress all other inhomogeneities of the image. This operation is usually performed in about 16 ms by a dedicated processor hosted on the frame grabber. A threshold is applied to the filter output to extract the dark spots that are candidates to become grains. Each pixel is then classified as *black* or *white*. Adjacent clusters of black pixels are recognised and those that exceed the bounds of a proper range of size are discarded. The clustering process performed in parallel with the digital filtering takes 4 to 15 ms depending on the number of clusters in the image. A full grabbing cycle of the camera lasts 33 ms. Thus, a considerable fraction of the CPU time is left free for other tasks.

The following step consists in combining grains from different layers to recognise geometrical alignments. This can be performed in a variety of ways. However, with an average number of 400 to 1000 grains in an image, and 20 to 30 layers, the combinatorial load on the CPU can be very high. For this reason, the field of view is subdivided in cells about 20 μm wide. Then, local alignments of grains are detected within each cell and across boundaries of neighbouring cells. This strongly reduces the possible combinations.

When a local alignment of grains on some consecutive layers is detected, the tracking module tries to extend it to the layers above and below, thus forming a track segment. A segment exceeding a certain threshold length is considered as a possible track. All tracks are checked to discard low-quality reconstructions and fakes. Then tracks are fitted with linear or parabolic trajectories. Sometimes the tracking procedure may split a track into two segments. If the two segments are recognised as part of the same track, they are tied together. All the 3D part of the track recognition process takes from 0.1 s to 0.5 s, depending on the number of layers, on the amount of fog grains and on the number of slow electrons in the emulsion.

A MegaPixel camera allows to use low magnification (30×), resulting in large fields of view (190 to 220 μm wide). Thus, with a frame rate of 30 Hz a wide area can be scanned. A relatively long time is needed to move the stage horizontally to the next field of view ($\sim$ 0.8 s). This is currently the tightest bottleneck. However, studies are going on to improve the mechanical performance of the microscopes and overcome the problem. Presently, the time needed to scan both sides of a field of view on an emulsion plate with a 200 μm thick base and 50 μm thick emulsion films is about 4.8 s.

Similar MTS approaches are presently under development in other institutes of the Collaboration, in particular in Naples. The driving principle in the design of this system is the use of state of the art commercial products, both for the hardware and for the software, and to make the system itself flexible enough to be upgraded following the rapid progress in the technology.

Preliminary tests were made using a large plate microscope stage (80×40 cm) produced by MICOS AG, Germany. The microscope is equipped with fast stepping motors both on the horizontal and on the vertical axes. The microscope adopts a low magnification optics system. A fast CCD camera is used with 512×512 pixels at 120 frames per second. This provides a field of view of about 200×200 μm^2 with an integration time of about 1 ms. Performance could be further improved by using fast MegaPixel cameras which will be soon available on the market. They will allow an increase of the field of view up to 350×350 μm^2.

During the vertical movement, the camera digitises a sequence of frames at different depths and sends the data to a Matrox Genesis board, a commercial frame grabber and video images analysis device. This board is equipped with a dedicated Digital Signal Processor (DSP) Texas Instruments TMS320C80. The board contains four parallel video processing units and a master processor. Up to six boards with 2 DSP and 2 Neighbour Operation Accelarator (NOA) can work together to analyse the image. The 64 $MByte$ internal memory of of each board is connected to the processing units by an high speed internal bus working at $\sim$ 400 $MByte/s$. The system is capable of filtering, digitising and clustering one frame in less than 10 ms. This allows to envisage a speed of 1 mm/s during data taking from the emulsion. The time needed to analyse a complete field (both emulsion sides) would thus be less then 300 ms.

The clusters produced by a mip are selected according to their size and darkness. The parameters of the grains (position, size, darkness and form factors) are then transferred to the PC memory. Here, the CPU of the PC applies a tracking algorithm similar to that one previously described. Track segments in the two emulsion layers are then connected and stored on the local database. The tracking is performed in parallel to the main acquisition sequence. By using a Pentium II class processor with 400 MHz clock, all tracks in a complete field are found in less than 200 ms. In perspective about 3 fields per second could be analysed taking into account the time needed to move to adjacent views. About 14 minutes could then be required to fully reconstruct all tracks contained in one centimetre squared of ES.

An approach oriented towards the use of software and of advanced commercial products in image processing is also followed by the CERN and NIKHEF groups of CHORUS. They have developed in collaboration with industry a new optics with a large field of view and optimised it for emulsion scanning. In the future, automatic scanning could profit from this development both in speed and quality.

4.2 Data handling

4.2.1 Data sources and storage

OPERA data have different origins: emulsions, electronic detectors, alignment, calibration, slow control, etc. The most important contribution to the data volume is due to digitisation of the tracks stored in the ESs.

Emulsions records information about all charged particles passing through their surface from production to development. The tracks stored in the emulsion come from several sources. The first (the most relevant) is represented by the particles which passed through the emulsion during the time between its production and its location in the underground laboratory. This background has two contributions: uncorrelated (before brick assembly) and correlated tracks (after assembly). The main source is given by penetrating cosmic rays (muons with $E > 1\ GeV$) We estimate this background as $\sim$ 12 muons$/mm^2/day$ at sea level. The contribution from natural radioactivity is less important. Another source of tracks is represented by cosmic rays in the cavern. According to data from Gran Sasso experiments, this flux amounts to about 3 muons$/m^2/hour$. This gives an additional density of 0.1 tracks$/mm^2/5\ years$.

Muons produced by neutrino interactions in the Gran Sasso rock upstream to the detector are an additional source of stored tracks. The mean energy of the muons produced by the CNGS beam is about 17 GeV, corresponding to a range of 90 m of water. The full OPERA thickness is equivalent to 40 m of water. In OPERA we expect about 18000 ν_μ CC events. Hence, the total amount of muons induced in the rock can be estimated to be $\sim$ 35000. For the emulsion this implies 10×10^{-4} tracks$/mm^2/5\ years$. Finally, neutrino events themselves produce tracks passing through other bricks (muons or penetrating hadrons). This rate is estimated in the same way and gives at most 6×10^{-4} tracks$/mm^2/5\ years$.

In conclusion, the amount of data coming from the emulsion amounts to about 10 tracks$/mm^2/5\ years$. This is the most time and disk-space consuming source of data in OPERA. Given the *Net Scan* analysis performed on $5 \times 5\ cm^2 \times 50$ sheets, this corresponds to 1250 cm^2 with 1.25×10^6 segments per event. Assuming 100 *byte* per segment, one obtains 125 $Mbyte$ per event or $\sim$ 3 $Tbyte$ in total.

Only additional $\sim$ 50 *Gbyte* will come from the other sources altogether: electronic detector data, simulated events, slow control and calibrations.

4.2.2 Database and handling

The various kinds of data mentioned above will be produced by different systems in different formats and laboratories. However, for further data analysis and processing they will have to be accessible in a uniform way. Some central data repositories will be needed. As shown above, the total amount of raw data will be of the order of 3 $Tbyte$. Taking into account the preliminary character of these estimates we do not expect the real amount of data to be more than $\sim$ 10 $Tbyte$.

95% of the data will be produced in the scanning laboratories. The raw data from *Net Scan* should be processed event by event to perform pattern recognition. Only $\sim$ 10 *kbyte* of the information about event and calibration tracks will be needed for further analysis. Each scanning laboratory should use $50 - 100$ *Gbyte* of temporary disk space, before transferring processed data to the central repository. There, 100 *Gbyte* of fast-access disk space will be enough to keep the complete information for physics analysis and back-up. All the hardware needed for the realization of the proposed scheme is conventional and affordable, already today.

From the software point of view there are several possible solutions for the database. As mentioned above, in general the data will be produced by different systems in different laboratories. The traditional solution for HEP represented by ZEBRA+DST will be obsolete.

Nowadays, three systems are used by scanning laboratories involved in CHORUS and OPERA: ORACLE, OBJECTIVITY and ROOT. ORACLE is the relational database world-wide used for many applications. The advantages of this system are its robustness and reliability. It is well supported and easy to use by non-physicists. Its disadvantages are that it has not been designed for HEP data and problems with the handling of huge tables interfacing to PAW or MathLab have been identified.

OBJECTIVITY is an object-oriented commercial database. Its main advantage is the use of the OO paradigm, today the leading approach for new HEP software (CERN LHC experiments). Some disadvantages are related to its scarce robustness and to the way it handles large data sets.

ROOT is a public domain software system being developed originally for the NA49 experiment at CERN and presently considered by a number of other experiments. The advantages of this system are the optimal match to the HEP requirements, and the fact that it has been developed for both data storage and data analysis, removing the need for interfaces.

4.2.3 Event graphics

Today's HEP experiments are typically carried out by large collaborations of many institutes and universities spread over several countries. Thanks to Internet physicists have direct access to the events of their experiment. WIRED [59] (World Wide Web Interactive Event Display) was created as an event visualisation framework using Java inside a World-Wide Web browser. OPERA joined the WIRED project for its event display. An example is given in Fig. 4.1.

WIRED is written in Java using the *Swing* set for its graphical user interface. It is completely portable and runs on any platform that fully supports the JDK (Java Development Kit 1.1 or better). WIRED's *graphic engine* handles both 2D and 3D drawings. It supports multiple views and control widgets, which interact with those views. It can access events and detector geometry data by using *XML* files. A converter is available from GEANT3 data into WIRED XML data.

Starting from the OPERA GEANT 3.21 detector and event simulation we created the XML files necessary to run WIRED. We began with a simple configuration using only one brick of ten lead cells with spacer, simulating ν_τ interaction with single prong τ decays. In order to run OPERA simulations under WIRED, 10 Java classes had to be created to define complete events.

Each event in the brick is fully described by the primary and secondary vertex and by the segments in the emulsion belonging to each particle (Fig. 4.2). Each segment retains the information about the particle producing it: particle ID, momentum and direction. These data are available for display on the screen. Fig. 4.3 shows a τ decay kink, and the path of secondaries particles generated in the interaction.

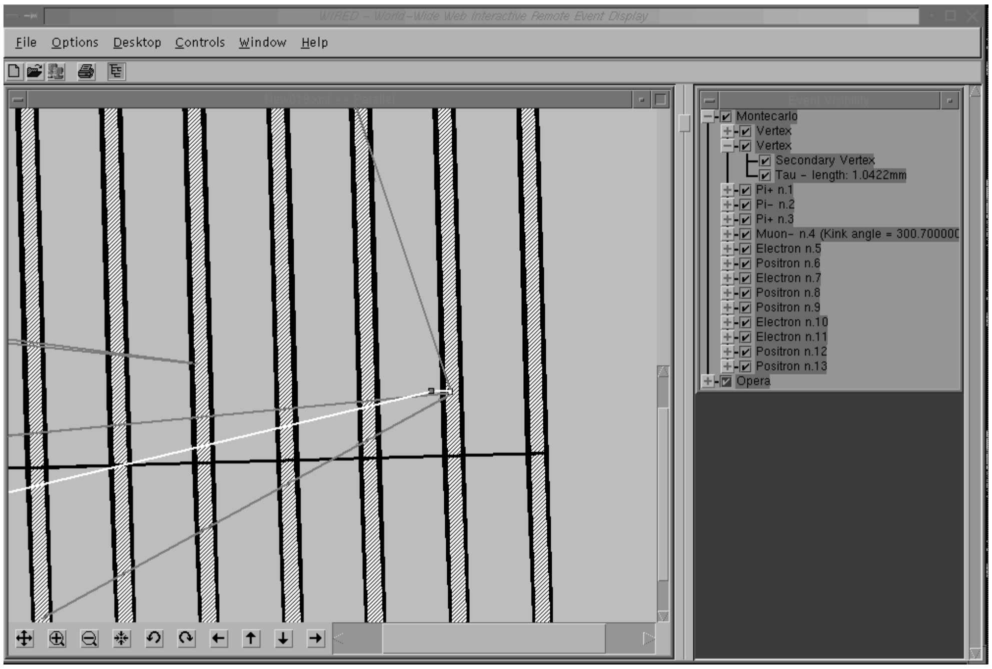

Figure 4.1: A WIRED application for OPERA also showing Menu Bar, Tool Bar, View Top and Control Top.

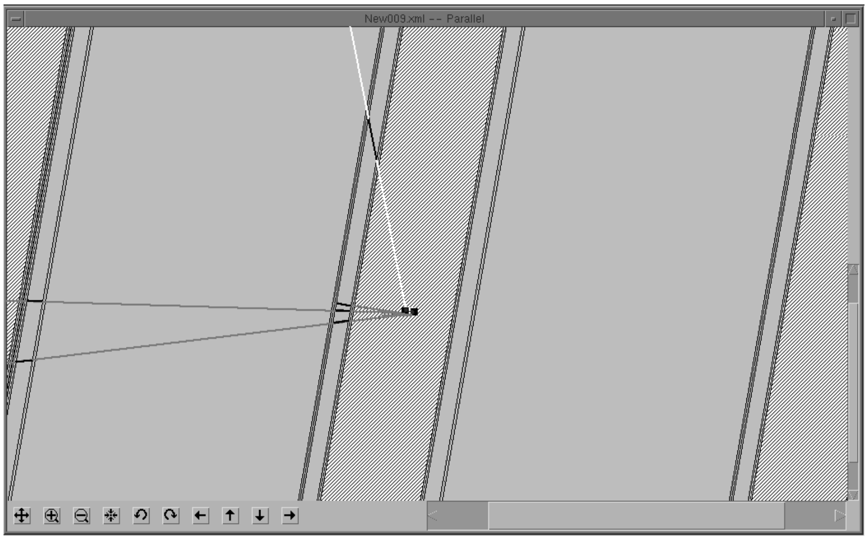

Figure 4.2: An example of WIRED zooming capabilities for a spacer cell: the τ decay length is as low as 72 μm.

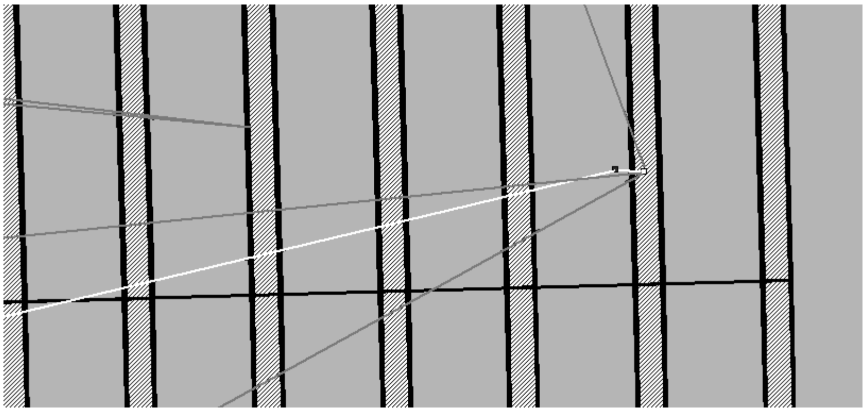

Figure 4.3: An OPERA event showing the τ decay kink in a spacer brick. The τ length is 1.04 mm and the kink angle is 300 $mrad$.

The whole OPERA detector event display, including spectrometers and electronic detectors information, will be realised using the WIRED *Fish Eyeing* capability, which allows to blow-up the inner detector parts and compress the outer ones, without sacrificing the visibility of the latter. Going from Monte Carlo to real data is relatively straightforward. We are starting to use WIRED to display real events, including grains and tracks in the emulsion sheets.

Chapter 5

Test measurements and results

5.1 Test beam measurements with prototype bricks

Several tests have been carried out at the CERN PS T7 beam line and at KEK to investigate various features of the experiment. The aim was to study the brick finding efficiency, the angular resolution, the kink finding capability, the momentum measurement by multiple scattering and the electron identification by detecting cascade showers in the brick. Bricks made with different emulsions, absorbers and spacers have been employed. Prototype electronic trackers have also been tested with their readout devices.

Further tests are underway at the PS T9 beam line on the vertex finding efficiency and some more are planned in the near future for specific studies on the emulsion performance.

5.1.1 Measurement setup

Going downstream along the beam line, the PS T7 setup consisted of two Cerenkov counters, four beam proportional chambers (BPC) (x, y, x, y) with a resolution of 300 μm on a area of 6×6 cm^2, bricks which could be rotated and tilted, two hodoscopes 10×10 cm^2 with vertical scintillating strips of various width (from the CERN NA52 experiment) and, finally, a 1.60 m iron block as hadron absorber. The bricks with the beam chambers and the hodoscopes are shown in Fig. 5.1.

Various trigger counters were placed along the beam line. The beam chambers and the bricks were mounted on a remote controlled movable table with possible movements of 50 cm in horizontal and vertical direction. This allowed a uniform exposure over a large area.

The pion beam was momentum selected between 1 and 10 GeV/c with a dispersion of $\sim 1\%$. The beam spot diameter was between 1.5 and 5 cm. The electron contamination was 24%, 16% and 3.7% at 2, 4 and 8 GeV/c, respectively. At 10 GeV/c the electron content was estimated to be around 0.3%. Closing the collimators provided a muon beam. However, the collimators could not be perfectly closed, resulting in a pion contamination of $\sim 5\%$ at 10 GeV/c. Track densities down to 0.1 tracks per mm^2 could be achieved by controlling each individual extraction.

5.1.2 Characteristics of the bricks

The prototype bricks with spacers consist of 30 cells with 15×15 cm^2 transverse dimensions. The metal plates are made of a 1 mm thick inox or lead sheet. The 3 mm spacer is Rohacell or polystyrene.

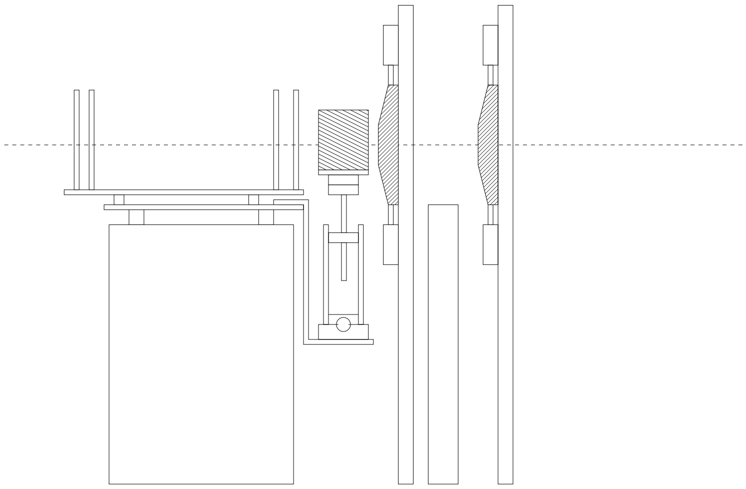

Figure 5.1: The test beam setup at the CERN PS. From left to right: the four BPC planes, a brick on the movable support and the two strip hodoscopes.

Two types of industrial ES were used: MES from Fuji Film, Japan and from FOMOS, Russia. Fuji MES have a 200 μm plastic substrate with 50 μm emulsion on both sides diluted by a factor two. FOMOS emulsion sheets have 180 μm base and 50 μm emulsion layers. They have two different dilution factors of 2 and 3. In addition to the industrial emulsions some emulsions sheets were poured at CERN from Fuji gel with 180 μm base and 50 μm emulsion layers.

A series of compact bricks was built by using Fuji MES and lead plates. The main purpose being the study of the electron identification capabilities and of the determination of the momentum by multiple scattering. The brick thickness is smaller than for the bricks with spacer for the same weight. 7 bricks of 29 cells and 1 mm lead absorber and 4 bricks of 44 cells and 2 mm inox absorber where built and exposed to the test beam. The MES have transverse dimension of $7 \times 7\ cm^2$.

One of the purposes of the test was the study of the brick identification efficiency by means of the electronic detectors placed downstream of each brick wall. A frame was carrying four dummy bricks, where the emulsion was replaced by a sheet of equivalent radiation and interaction length. The brick support, a small size harp structure, consists of a stainless steel strip structure whose thickness orthogonal to the beam is about 1 mm (Fig. 5.2).

The relative alignment of the hodoscopes and the BPC was carried out by using passing through pions. In Fig. 5.3 we show the result of such a procedure for two strips. The following step was the alignment of the brick support with the BPC. This is shown in Fig. 5.4 where the pattern of the support at the intersection between four bricks is clearly visible.

5.1.3 Angular resolution measurements

The angular resolution determines the minimum detectable decay kink angle. This quantity has direct implications on the signal detection efficiency.

Bricks with spacers were exposed to a 10 GeV/c muon beam at different angles of $0°$, $+6°$ and $-15°$ and to pion beams of 10, 4, 3 and 2 GeV/c up to a density of 1 track per mm^2. In the exposure to

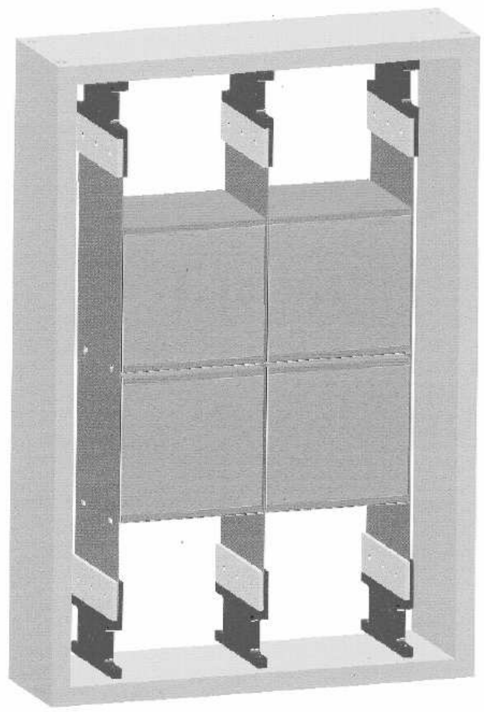

Figure 5.2: The four fake bricks used in the test beam and their support.

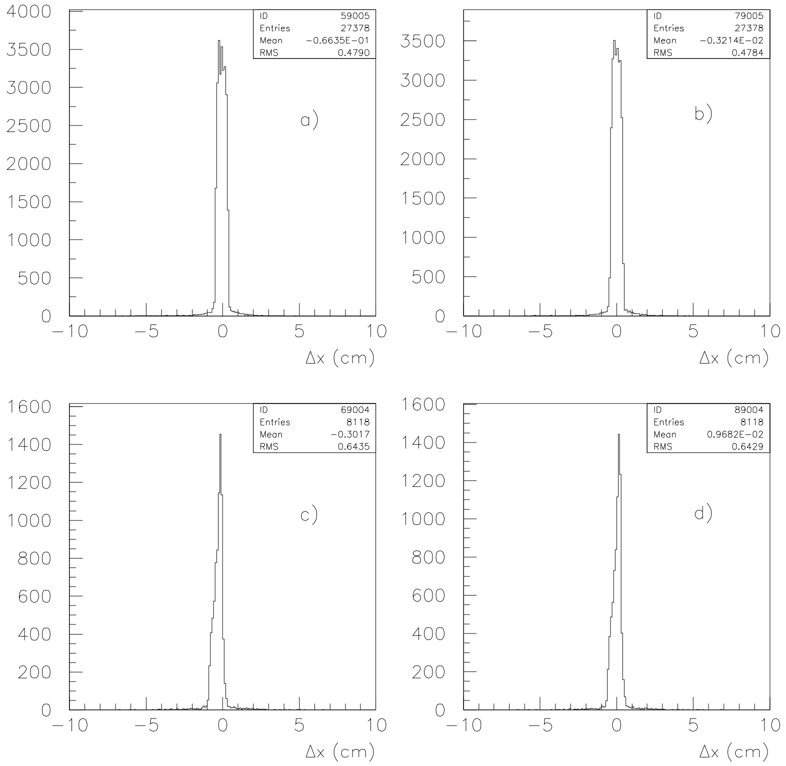

Figure 5.3: Strip positions before (a and c) and after (b and d) alignment.

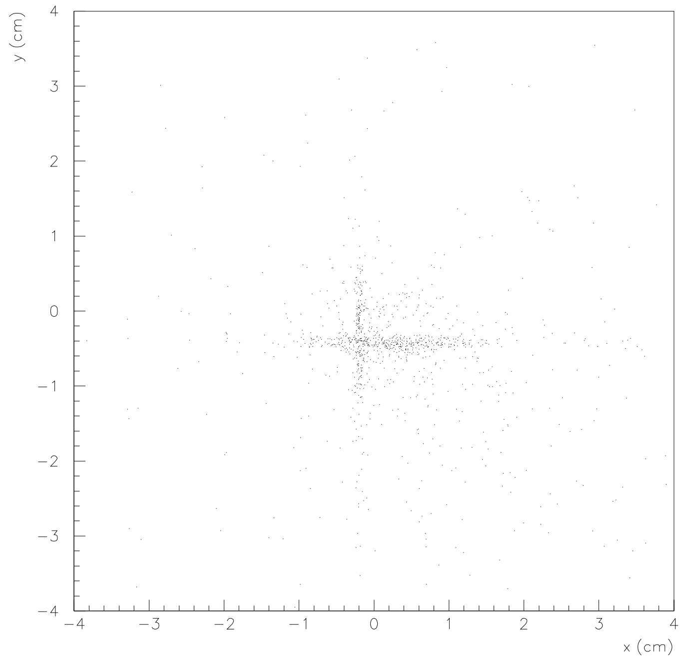

Figure 5.4: Pattern used to align bricks and BPC. The cross is due to pions going through the boundaries of four bricks.

pions, when the pion momentum was changed, the brick was rotated to the left or right and tilted up and down by $6°$. This allows a unique identification of the momentum in the analysis. The brick was uniformly illuminated over an area of 10×14 cm^2. The analysis presented below refers to the pion exposure.

Soon after exposure the emulsions are processed with standard techniques. A grid of fiducial marks is printed on each plate with an accuracy of a few hundreds microns to provide future reference for the scanning. The emulsion is developed and cleaned. Consecutive ESs are fixed onto a plastic support (plexiholder) having the size of the microscope stage (40×40 cm^2).

The scanning was performed by using a microscope equipped with a New Track Selector system. The angle of the passing particle is measured from the line connecting the grains near the ES plastic base. The accuracy in the position measurement of the grains (less than 1 μm) and the thickness of the base (200 μm) determine the angular resolution.

The result of the scan performed on one ES of the first cell is shown in Fig. 5.5. About 18 cm^2 of ES surface were scanned, subdivided into 25 rectangular areas. Prediction scan back was applied around the known pion beam direction. The sample of collected tracks shows four narrow peaks in the angular distribution corresponding to the four beam momenta (Fig. 5.6).

A first rough inter-calibration of different plates is given by the measurement of the reference fiducial grid printed on each ES. The precise alignment procedure requires the comparison of the spatial pattern formed by tracks measured on consecutive layers. Once a match has been found between two patterns, the affine transformation which relates the two samples is calculated by means of a maximum likelihood method. As

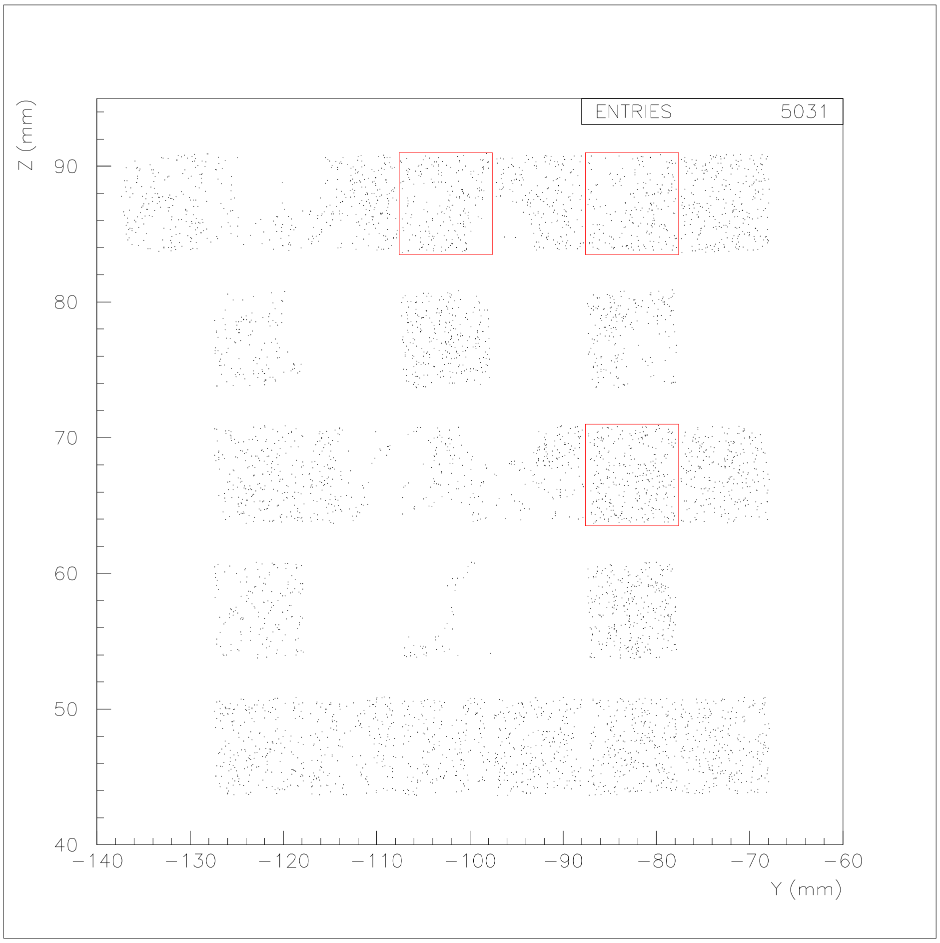

Figure 5.5: Result of ES scanning. The pattern of all tracks found in a cone centred around the nominal beam direction is shown. The squares identify the areas used for calibration.

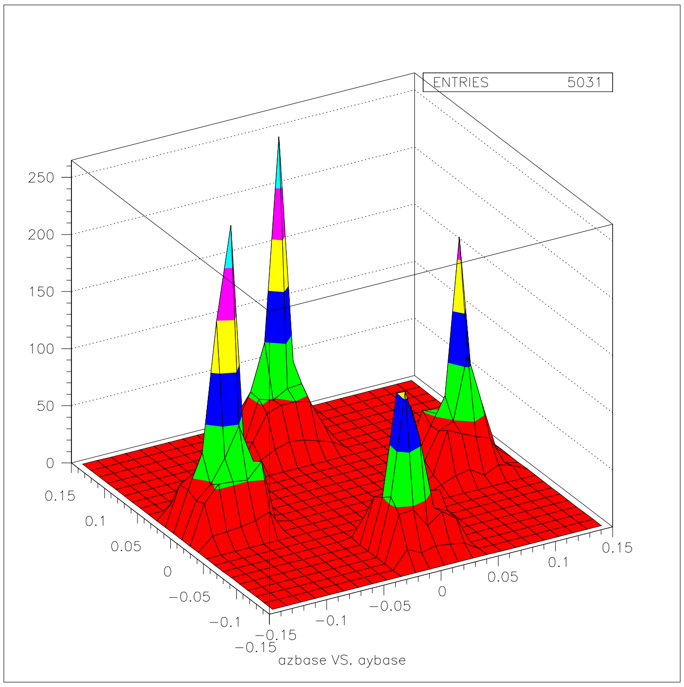

Figure 5.6: The peaks correspond to the different angles for exposures to 10, 4, 3 and 2 GeV/c pions, projected onto the first ES.

shown in Fig. 5.7, the measured spatial offsets are of the order of 500 μm and rotations less than 2 $mrad$. The intrinsic accuracy of the alignment procedure is of a few μm.

After calibration all tracks found in a given ES are projected onto the following ES and used as predictions for scan back. Tracks measured in at least three consecutive cells are selected (Fig. 5.8). This sample, consisting of straight passing tracks, is used to measure the angular resolution. For each ES and for the selected tracks the difference between the measured angle and that predicted by the upstream sheet is recorded in both projections, as shown in Fig. 5.9. The experimental distribution is a Gaussian, of zero mean, $\sigma \sim 5$ $mrad$ and no tails, as shown in Fig. 5.10. This results are consistent with expectations.

5.1.4 Momentum measurement by multiple scattering

With an emulsion detector it is possible to determine the momentum of a particle by measuring its multiple scattering, through the detection of the deviations of the track trajectory. This procedure is relatively effective in an ECC, where thin plates of dense passive material are inter-spaced with emulsion layers.

The rms scattering angle in any projection is given as a function of the momentum (p) and of the path length of the particle (x)

$$\theta_0 = \frac{13.6\ MeV}{\beta c p} \sqrt{x/X_0}\ [1 + 0.038\ ln(x/X_0)] \tag{5.1}$$

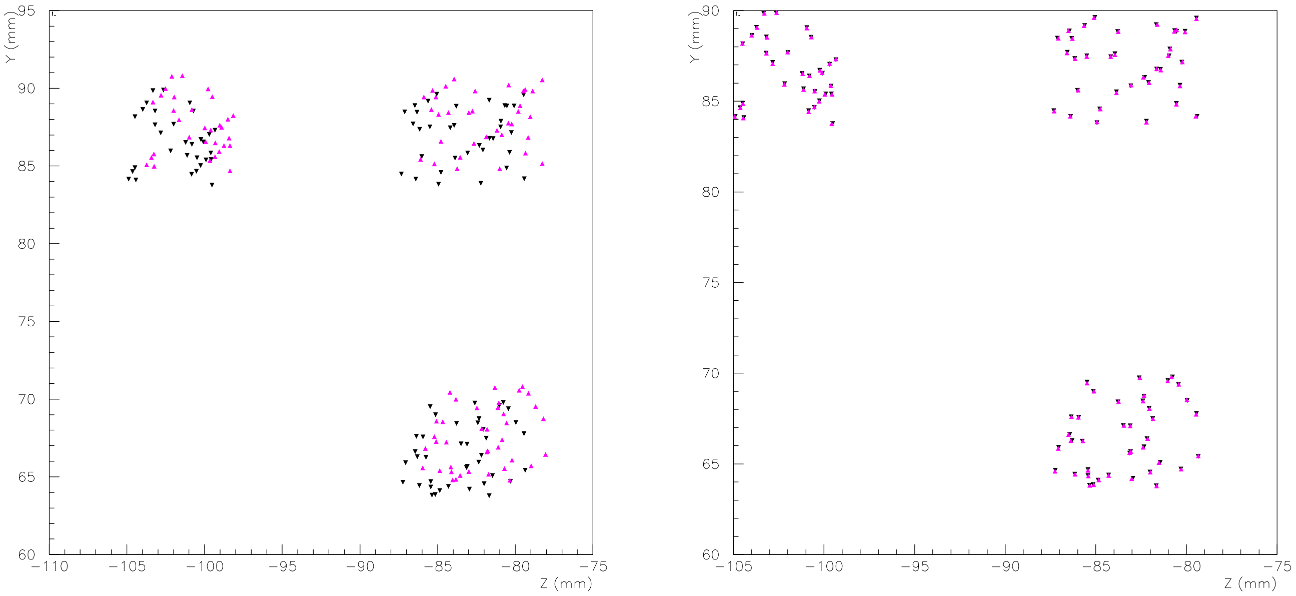

Figure 5.7: Detail of pattern of tracks associated in two consecutive ESs and superimposed, before (left) and after (right) calibration is applied.

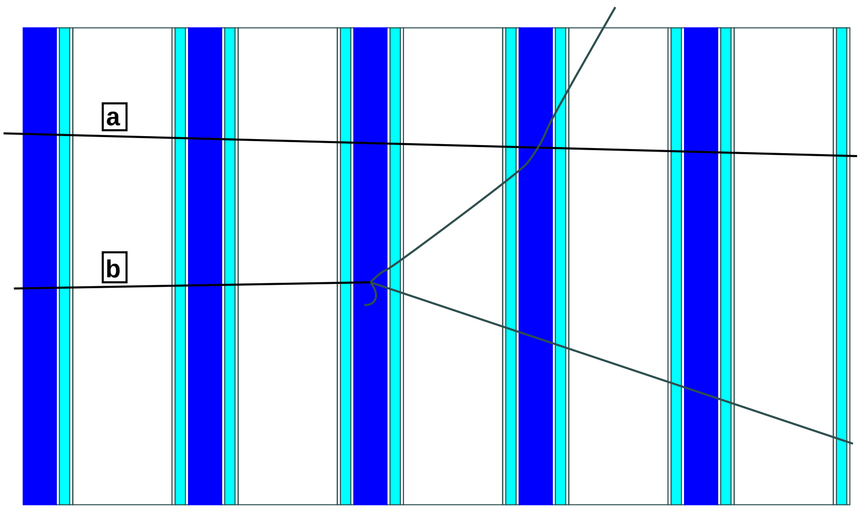

Figure 5.8: Selected sample: tracks followed through several cells (a). Also shown is a track found in the first two cells and not validated in the third (b).

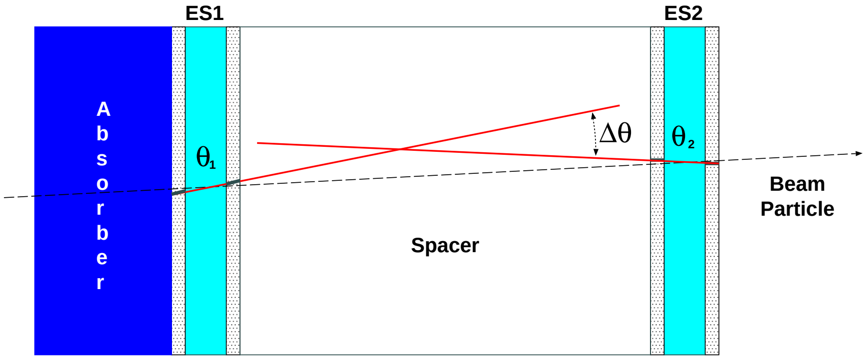

Figure 5.9: For each projection, the angular resolution is evaluated by computing the difference $\Delta\theta = \theta_1 - \theta_2$. The angles are artificially enlarged in the figure with respect to the real case.

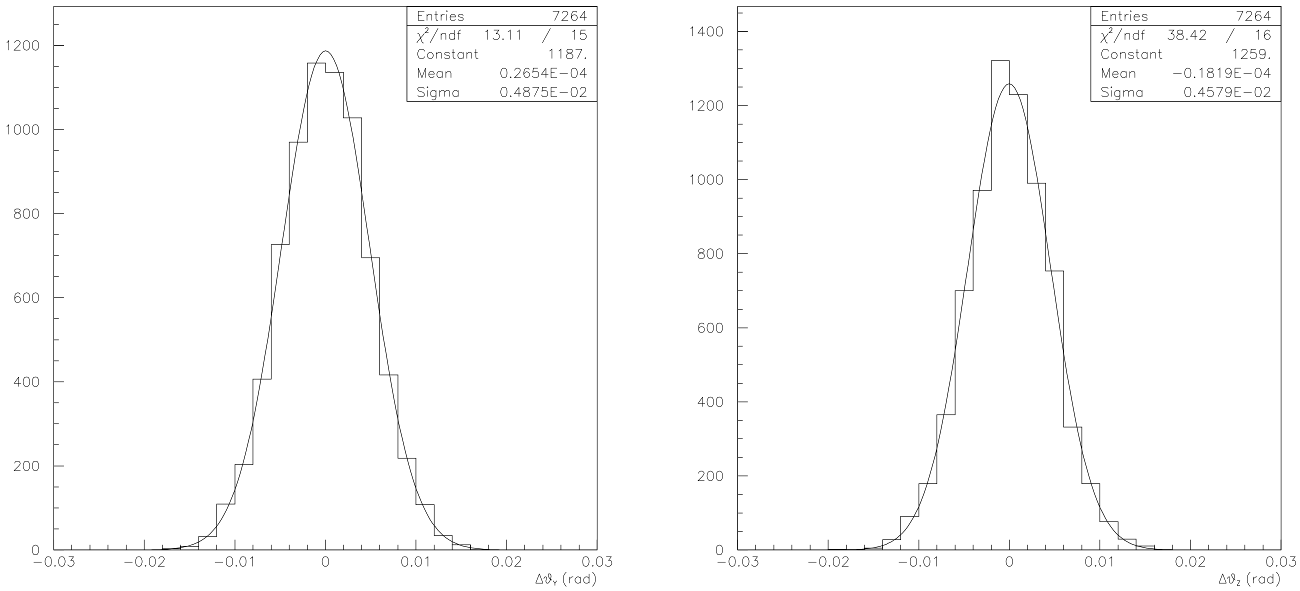

Figure 5.10: Measured angular resolution for spacer bricks (in projection).

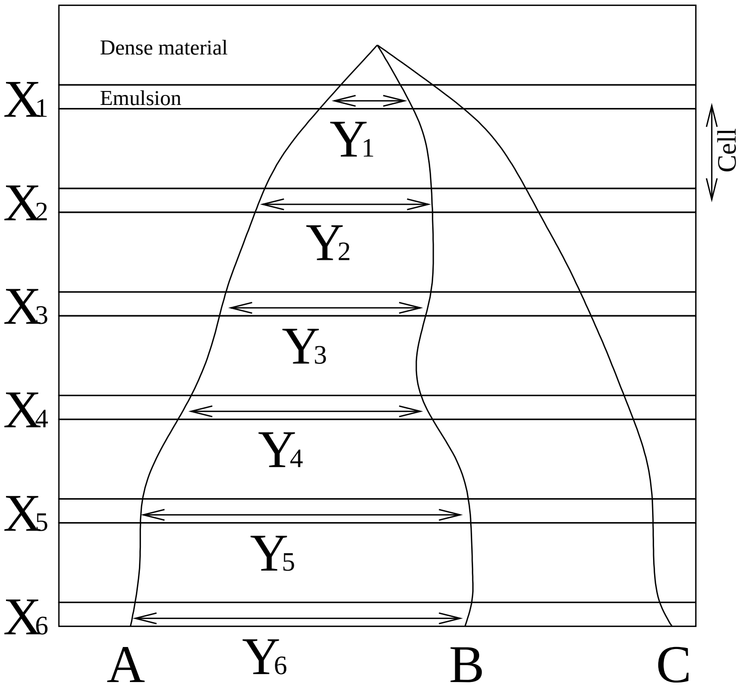

Figure 5.11: Relative scattering angles between two tracks A and B traversing an ECC, together with a track C.

One can measure y, z, θ_y and θ_z in each emulsion film of the ECC. Therefore, the sandwich structure of the detector allows a multiple measurement. The so called *Relative Scattering Method* is a powerful method to measure particle momenta. Let's assume to have three particle tracks A, B and C traversing an ECC. For the pair of tracks A and B, in each projection one can measure their distances Y_i at each emulsion layer (Fig. 5.11). If the distance between the emulsion layers is constant, for the ith cell the *second difference* is δ^i_{AB} is $\delta^i_{AB} = (Y_{i+1} - Y_i) - (Y_{i+2} - Y_{i+1})$.

If the measurements is performed through the whole ECC structure, by averaging one obtains $\langle\delta^2_{AB}\rangle$. The relative scattering angle is $\langle\theta^2_{AB}\rangle = \langle\delta^2_{AB}\rangle/L$, where L is the cell length.

The relation between the relative scattering angle $\langle\theta^2_{AB}\rangle$ and the absolute ones $\langle\theta^2_A\rangle$, $\langle\theta^2_B\rangle$ is the following

$$\langle\theta^2_{AB}\rangle = \langle\theta^2_A\rangle + \langle\theta^2_B\rangle$$

If one has at least three tracks A, B, C one can write

$$\langle\theta^2_{AB}\rangle = \langle\theta^2_A\rangle + \langle\theta^2_B\rangle \ ; \qquad \langle\theta^2_{BC}\rangle = \langle\theta^2_B\rangle + \langle\theta^2_C\rangle \ ; \qquad \langle\theta^2_{CA}\rangle = \langle\theta^2_C\rangle + \langle\theta^2_A\rangle$$

Therefore

$$\langle\theta^2_A\rangle = \frac{\langle\theta^2_{AB}\rangle + \langle\theta^2_{CA}\rangle - \langle\theta^2_{BC}\rangle}{2} \tag{5.2}$$

Similarly for $\langle\theta^2_B\rangle$ and $\langle\theta^2_C\rangle$.

By using N reference tracks to measure the momentum of a single track A, equation (5.2) can be extended as follows

$$\langle \theta_A^2 \rangle = \Big[\sum_{i=1}^{N} \langle \theta_{Ai}^2 \rangle + \sum_{i=1,N-1}^{j=i+1,N} \langle \theta_{ij}^2 \rangle / (N-1) \Big] / N$$

According to equation (5.1) one can then determine the momentum of the particle. The error on the momentum estimate depends on the number of independent measurement points. For example, for 22 plates and two plates for one cell, the number of independent points is 10 for one projection. For both projections, this number becomes 20. In this case, the momentum measurement error $\delta p/p$ is $0.8/\sqrt{n} = 0.8/\sqrt{20} = 0.18$.

One of the test beam measurements consisted in exposing a brick with a 3 mm Rohacell spacer and lead as absorber to pions of different momenta. In particular, data with momenta from 2 to 4 GeV/c were analysed. Scanning four cells corresponds to about 0.8 radiation lengths total thickness traversed by pions. For each nominal momentum about 100 tracks traversing one radiation length were measured.

The measurement method consists in evaluating the σ of the angular distribution as a function of the number of cells traversed ($i.e.$ material thickness). The width of this distribution is determined by two factors, the angular measurement error and the multiple scattering itself. The angular distribution of tracks just traversing the spacer is used to evaluate the first term since multiple scattering inside the spacer is negligible. After unfolding the angular resolution the multiple scattering contribution is obtained as a function of the traversed material. The multiple scattering angle (in $mrad$) as a function of X_0 is shown in Fig. 5.12. A fit to this curve allows to evaluate the intrinsic contribution of multiple scattering to a momentum measurement (Table 5.1).

Table 5.1: Contribution of multiple scattering to a momentum measurement.

Nominal beam momentum	2.0	3.0	4.0
Result of the measurement	2.0 ± 0.1	2.6 ± 0.2	4.1 ± 0.4

A test of the momentum measurement by the *Relative Scattering Method* was performed exposing a brick to a 4 GeV/c pion beam at KEK. The compact brick used is made of 23 lead plates 1 mm thick interspaced with Fuji emulsion sheets of the same type of those previously described (factor two dilution). The radiation length of the brick is 4 X_0. A brick portion of 11 $mm \times 9$ mm was scanned and 396 penetrating tracks were found. 301 tracks with an angle within ± 20 $mrad$ around the beam direction were selected. Fig. 5.13 shows the measured momentum distributions for data and Monte Carlo simulated pion tracks of 4 GeV/c. Fig. 5.14 shows the relation between the reconstructed and the nominal momentum obtained by measuring scattering every two plates, for the 4 GeV/c data pions and Monte Carlo simulated pions from 1 to 9 GeV/c. The measurement error $\delta p/p$ is determined by a two-Gaussian fit for the data and by a single Gaussian for Monte Carlo events. The momentum resolution is shown in Fig. 5.15.

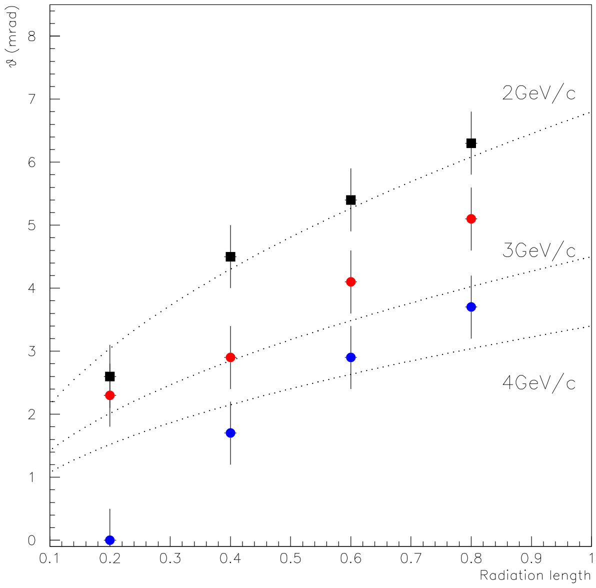

Figure 5.12: The multiple scattering angle (in $mrad$) is plotted against the number of traversed cells (in X_0) for three different pion momenta. The theoretical curves are also shown.

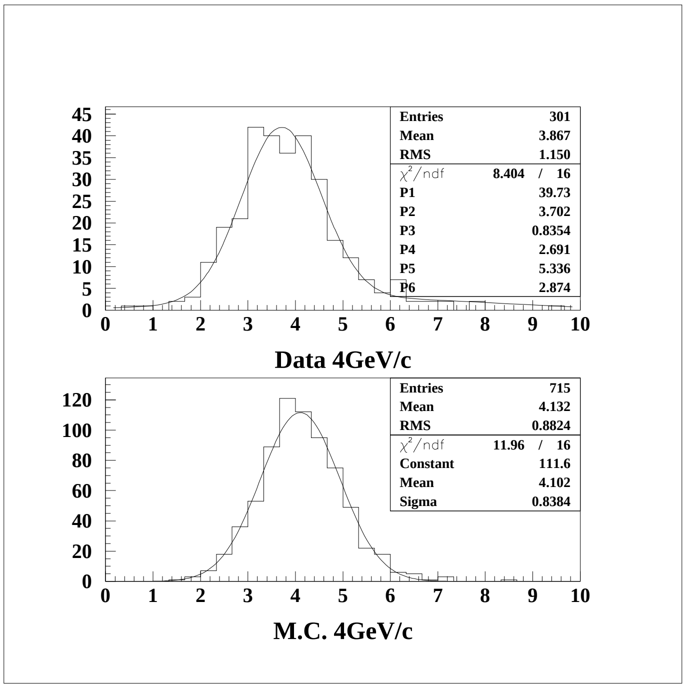

Figure 5.13: KEK test beam: momentum distribution for data and simulated events.

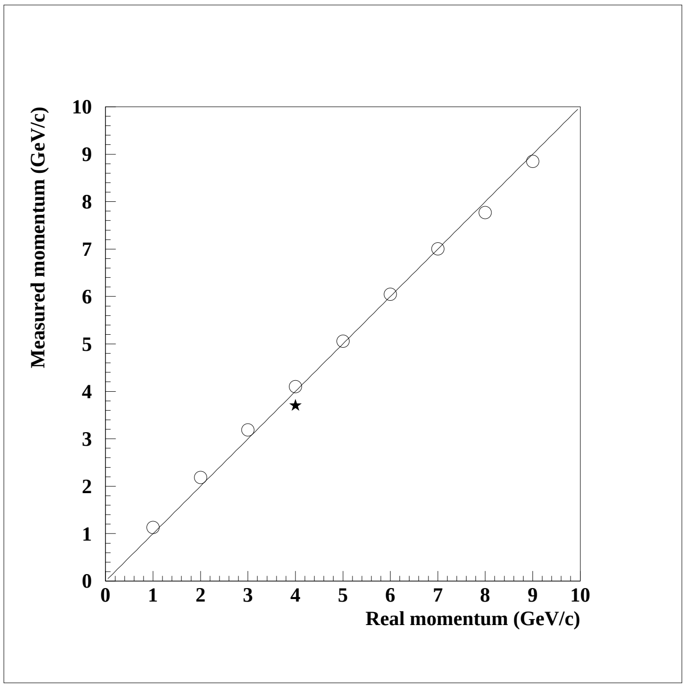

Figure 5.14: Relation between nominal and measured momentum (multiple scattering) for simulated events. The star indicates the test beam data.

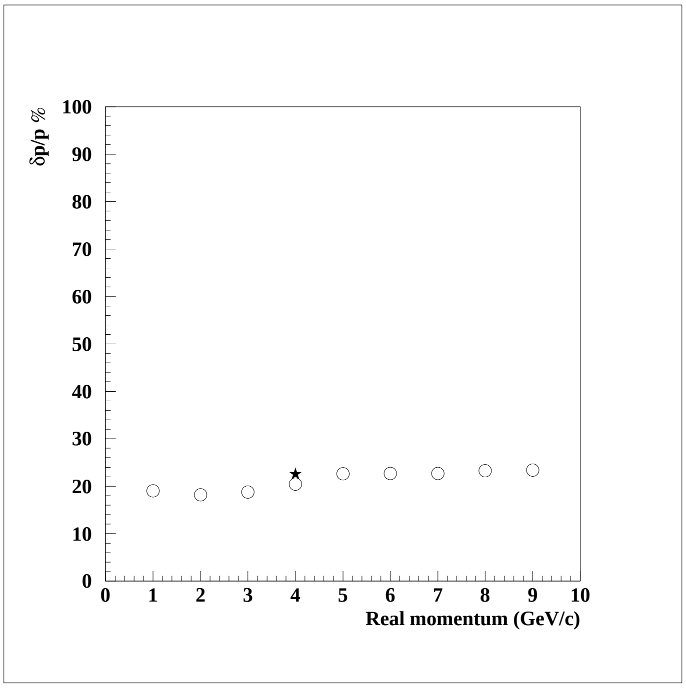

Figure 5.15: Momentum resolution as a function of the momentum for simulated events. The star indicates the test beam data.

5.1.5 Electron identification with compact bricks

Compact bricks were exposed to various beam momenta (2, 4 and 8 GeV/c) and with track densities between 0.02 and 10 tracks/mm^2. In order to tag beam electrons, the signal of the two Cerenkov counters in the beam line had to be related to track segments in the emulsion by extrapolating the tracks measured with the beam proportional chambers. The problem of the *high* track density was solved as follows. An emulsion sheet, placed between the beam chambers and the brick, was displaced by a few millimetres every SPS cycle. Pattern matching between the movable sheet and the bricks allows then to relate tracks inside the bricks to the corresponding SPS cycle. The density per cycle was chosen low enough to obtain a unique link to the beam chamber and therefore to the Cerenkov counters. In order to reduce the dead time an *electron* signal from the Cerenkov counters were required by the trigger.

A compact brick exposed to 8 GeV/c pions with a track density of 0.6 tracks/mm^2 has been scanned and analysed, following the predictions from the beam chambers and the electron tagging by the Cerenkov counters. The brick has a cross section of is $7 \times 7\ cm^2$ and is made of 32 lead plates, 1 mm thick, each followed by two ESs (*doublet* ES). This corresponds to 5.7 radiation lengths along the beam. The use of an ES doublet allows us to emulate the low background track density achievable in the Gran Sasso cavern, by rejecting segments not correlated in both ESs.

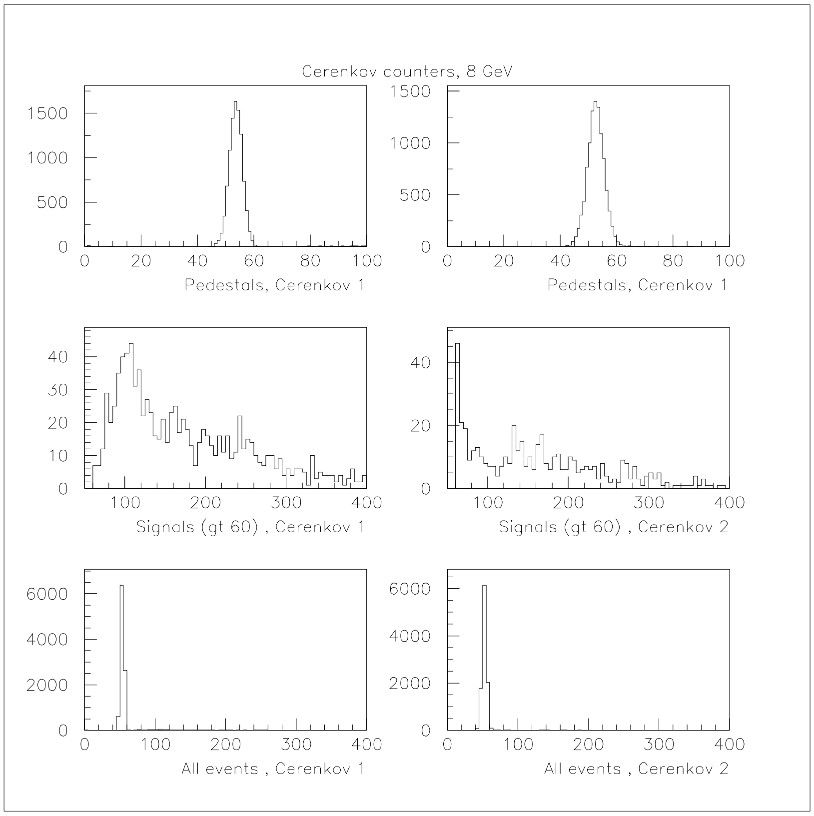

Figure 5.16: Cerenkov spectrum.

14 events tagged as electrons by the first Cerenkov counter ($C1 > 65$) were predicted to hit the $7 \times 7\ cm^2$

brick surface. One has to stress that the results of this analysis do depend on the electron tagging by the Cerenkov detector. Both Cerenkov counters were set such to have pions well below threshold, but the second one (C2) was not properly working during the data taking. For this reason we could not use it to quantify the purity of the electron sample. Fig. 5.16 shows pulse height distributions for both Cerenkov counters.

The predictions for tagged events were followed in the brick, with the aim to detect shower-electrons in the ES at the depth of 3 radiation lengths. General scanning was performed for both the doublet ES within a $5 \times 5\ mm^2$ surface, with an angular acceptance of $\pm 300\ mrad$. In order to reduce the background due to isolated ES segments, the connection of tracks in the doublet was required, with certain tolerances both in position and in angle. The requirement of the track association determines an energy cut-off. For 20 MeV electrons, about 50% of the tracks are retained (Fig. 5.17). An event is shown in Fig. 5.18.

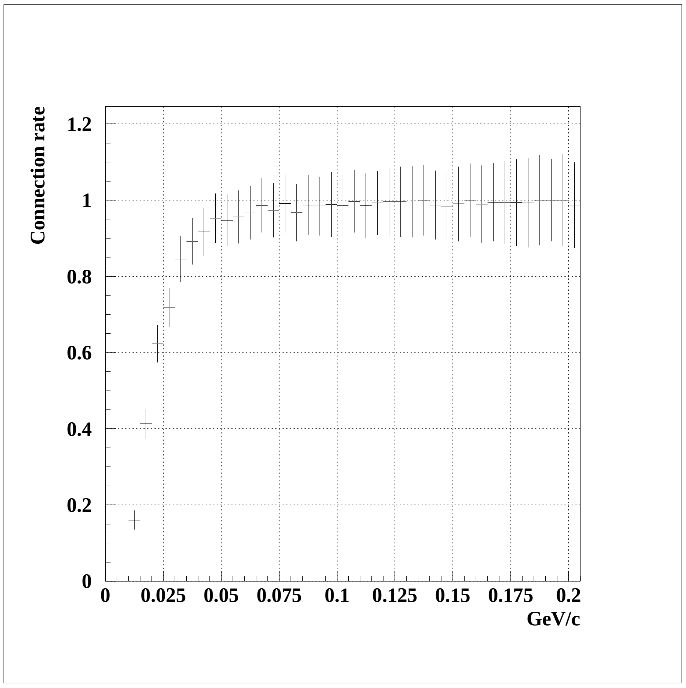

Figure 5.17: Energy cut-off due to doublet ES track association. All shower tracks with energy higher than 50 MeV and 50% of those with 20 MeV are reconstructed in the doublet ES.

The shower-electron positions and angular distributions are shown in Fig. 5.19. According to a GEANT 3.21 based Monte Carlo, 9.9 electrons are expected at 3 X_0 within $\pm 1.36\ mm$ (50 $mrad$ cone) and 300 $mrad$ angular acceptance, while 8.1 electrons are expected within $\pm 500 \mu m$.

The scanning status and the results for the 14 predictions are summarised in Table 5.2. The observed number of shower-electrons in the ES at the depth of 3 X_0 is in good agreement with the Monte Carlo predictions, proving the principle of electron identification by detection of cascade showers. However, the above result cannot be considered as a measurement of the electron identification efficiency. This can be determined by performing the scan of all the ESs where the shower develops. This complete analysis has been performed for one specific candidate, as presented in the following.

For this event, general scanning was applied to 44 ESs (22 doublets) in order to study the electron

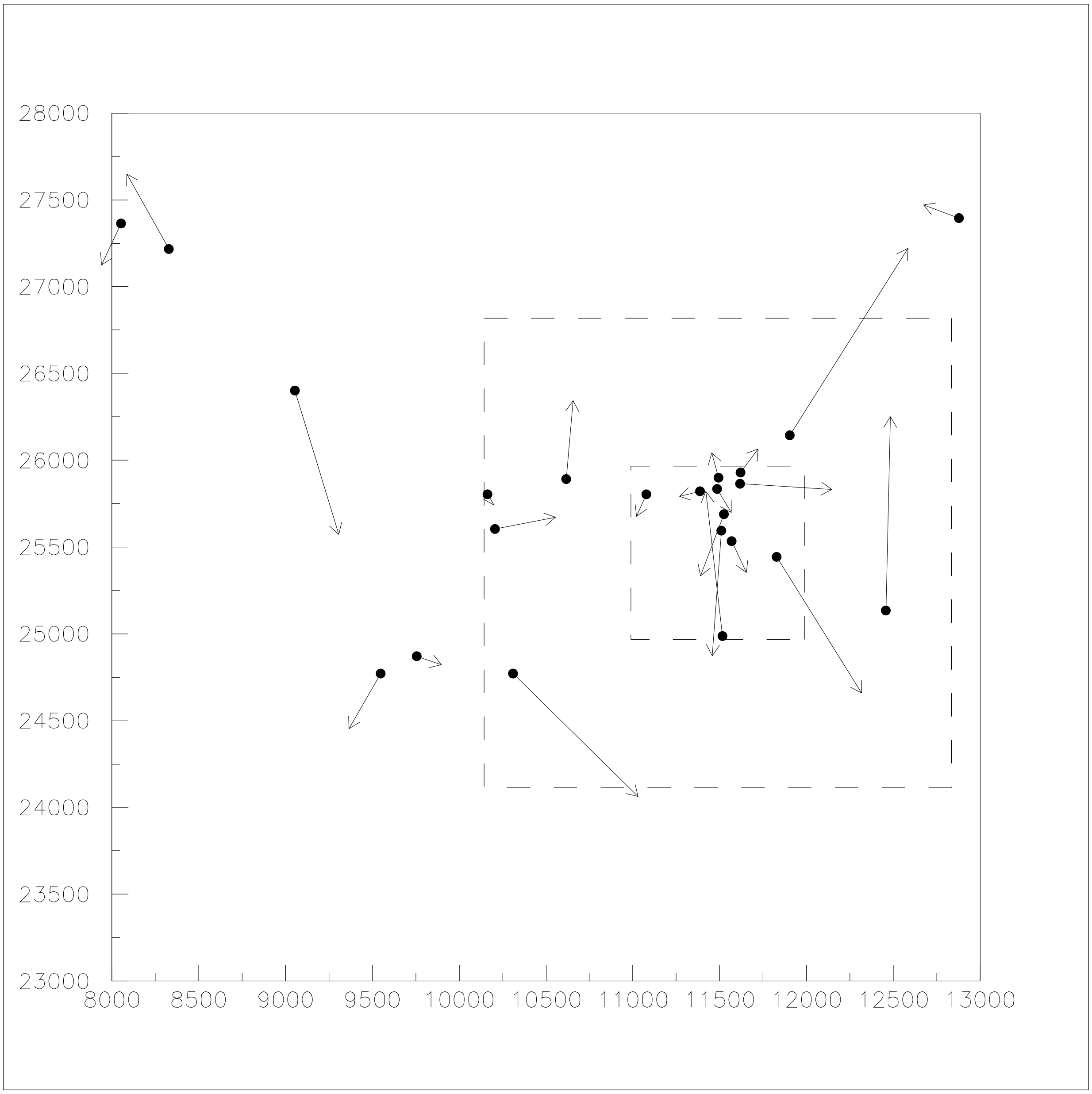

Figure 5.18: A 8 GeV/c electron shower event at 3 X_0 depth. Data are taken by the automatic scanning system following the BPC predictions $(X, Y) = (11513, 25463)$ μm for both the ESs doublet. Tracks are shown in 5×5 mm^2 and are associated in both ESs, within an angular acceptance of ± 300 $mrad$ around the beam axis. The arrows indicate the track angle as measured by the scanning system. 17 (11) tracks are found within ± 1.36 mm (± 500 μm) around the prediction with 2.4 (0.3) background tracks.

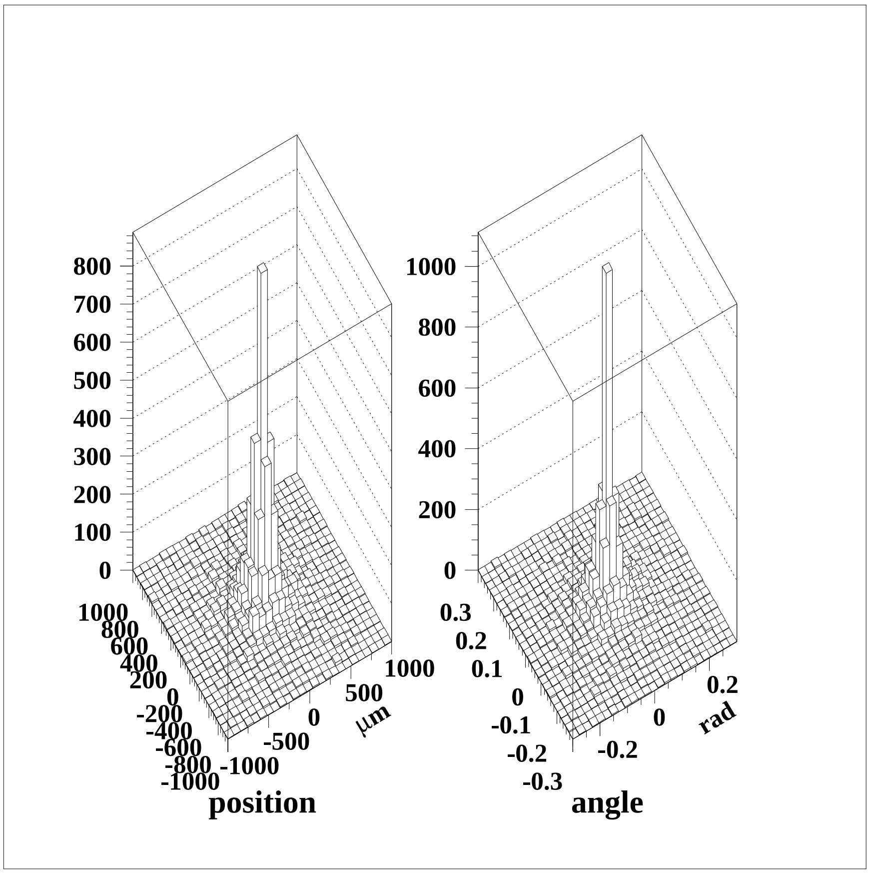

Figure 5.19: Shower-electron position and angular distributions at a depth of 3 X_0.

No.	θ_x	θ_y	Cerenkov		Electrons	BG
	$mrad$		C1	C2	at $3X_0$	
1	-1	-1	254	68	5(3)	5.7(0.8)
2	0	-2	76	54	9(2)	3.3(0.5)
3	-3	-7	173	55	9(3)	2.5(0.3)
4	-2	-9	88	53	8(1)	4.4(0.6)
5	-3	-10	94	51	1(0)	0.9(0.1)
6	-8	-5	118	52	20(9)	6.2(0.8)
7	-6	-2	120	52	16(9)	3.2(0.4)
8	2	-1	129	284	12(11)	2.6(0.3)
9	2	-2	92	56	9(2)	3.4(0.5)
10	3	0	264	295	17(11)	2.4(0.3)
11	38	-20	256	224	3(1)	4.2(0.6)
12	1	-1	304	58	14(7)	3.0(0.4)
13	1	-1	257	178	13(4)	3.4(0.5)
14	17	20	90	52	6(4)	3.6(0.5)

Table 5.2: Features of the test beam electron events for which scanning has been completed at the depth of 3 X_0. The number of shower electrons is given by the number of tracks within ± 1.36 mm ($\pm$ $500\mu m$) around the predicted primary electron position.

shower development in the brick. Each doublet was scanned over a surface of 5×5 mm^2 within an angular acceptance of ± 300 $mrad$. Fig. 5.20 shows the shower structure inside the compact brick. In total, 106 track segments are found within a 50 $mrad$ cone with an expected background of 34.6. Monte Carlo predicts 141 shower electrons with a rms of 36.6.

The analysis of test beam electron data will continue with the aim of studying the electron identification efficiency and the energy measurement capabilities. These results will also be used to tune and calibrate the Monte Carlo simulations.

5.2 Tests on electronic detectors

5.2.1 Prototype scintillator strip modules

In order to evaluate the performance and gain experience for a larger module construction, four small prototype modules have been built. Each module is made of 32 scintillator strips arranged in an array of 16 rows of two strips. The strips were produced by injection moulding technique with a cross section of 20×9 mm^2 and a groove of 1.3×1.3 mm^2 centred on a face. The strip length (30 cm) is limited by the existing mould. Each strip is coated except for the groove using the method developed by UNIPLAST[1]. Double clad 1.2 mm diameter BICRON BCF 91A WLS fibres are glued into the grooves with a transparent silicon couplant. On one side of the module the fibres are routed to a 4×4 multianode HAMAMATSU M16 PMT through a cookie. On the other side of the module the fibres are gathered in a bundle and routed to a block of Plexiglas with a built-in LED pulser. A photograph of the prototype is given in Fig. 5.21.

[1]UNIPLAST Vladimir, Russia

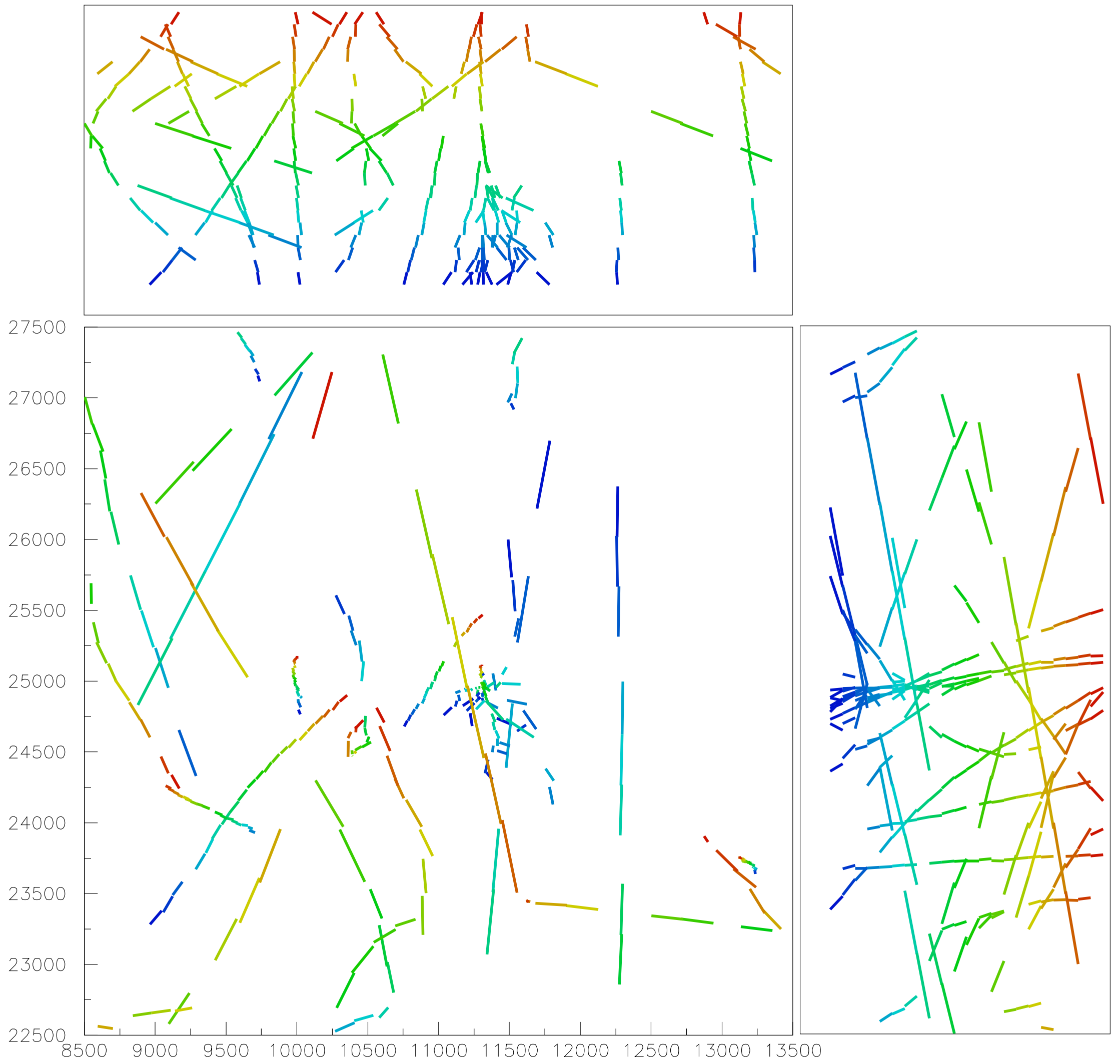

Figure 5.20: Electron shower development for one event. The Figure shows tracks in the $5 \times 5\ mm^2$ cross section times 33.6 mm depth. Tracks are required to be in the angular acceptance of $\pm 300\ mrad$ around the beam axis.

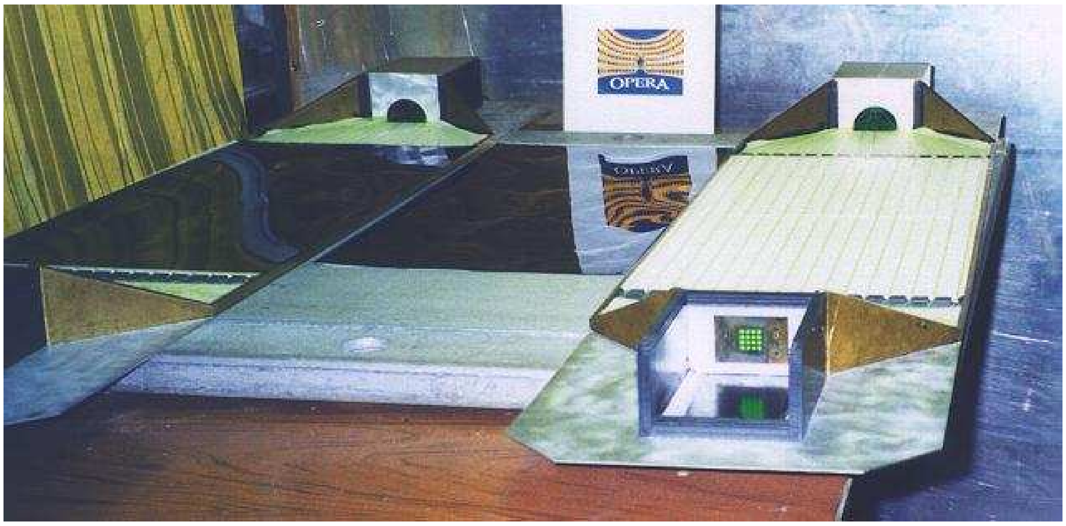

Figure 5.21: Prototype scintillator strip modules at the assembly site.

The PMT signals are transmitted via a screened twisted pair ribbon cable (55 m long) amplified with a $\times 9$ gain amplifier and digitised with the LeCroy 4300 11-bit ADC.

5.2.2 Performance of a scintillator strip module

A mixed beam of negative pions and muons with momenta up to 15 GeV/c was used for the PS T9 measurements. The following issues were addressed in these tests:

- performance of individual modules (the average response to minimum ionising particles (*mip*), the efficiency and uniformity across the strip planes);
- location accuracy with a prototype scintillator strip tracker and a dummy brick target.

The modules were stacked, with their planes perpendicular to the beam, on a remotely controlled platform which could be moved vertically (along y-axis) and horizontally (along x-axis) across the beam to scan the sensitive area of the modules and measure their response at different positions across and along the strips.

The beam spot had a full width of about $3 \times 5\ cm^2$. The trigger telescope includes scintillator counters and the four multi-wire beam profile chambers (BPCs) previously described. Only non-interacting beam particles with less than 2 *mip* deposition in each trigger counter are selected for the analysis. Additional cuts are imposed on the beam incidence angle and impact position, as measured by the BPCs.

The module PMTs are calibrated with the LED pulser tuned so as to measure the response of each pixel to a single photo-electron. Single photo-electron signals are clearly separated from the pedestals (Fig. 5.22). This allows us to express raw strip signal pulse-heights (PH) in photo-electrons, defined for each strip as the PH at the maximum of its single photo-electron peak. The effect of pixel-to-pixel gain variations is eliminated.

Due to pixel-to-pixel cross-talks in a PMT, small signals (≤ 1 *p.e.*) appear in pixels adjacent to the one coupled to the hit strip. Therefore, we associate a hit in a *mip* event with the strip producing the largest pulse-height (PH_{max}). Fig. 5.23 (left) shows the average PH_{max} as a function of the corresponding strip

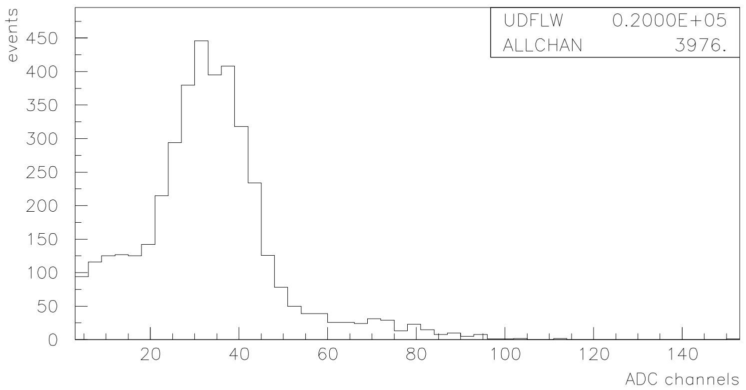

Figure 5.22: A typical PMT response to a LED pulse in the single photo-electron region. Pedestals are subtracted.

number in one module. The strip response fluctuates by 6% due to variations in scintillator strip and WLS fibre light yield, light attenuation in fibres, strip-fibre and fibre-PMT coupling, light trapping efficiency, etc., and also due to the photo-cathode non-uniformity. Fig. 5.23 (right) shows the overall $\mathrm{PH_{max}}$ distribution measured at the far end of one module (at 84 cm from the PMT). The mean value of this distribution is 7.7 $p.e.$ for events with $\mathrm{PH_{max}} > 1$ $p.e.$ It is interesting to note that a single $p.e.$ signal is still recognisable in the $\mathrm{PH_{max}}$ distribution.

The inefficiency peak at zero PH is mainly due to a dead space between strips. This is illustrated by Fig. 5.24 showing a detailed $\langle\mathrm{PH_{max}}\rangle$ distribution around one of the strips. The peak contains about 1.5% of all mip events and quantifies the module hermeticity. A cut of $\mathrm{PH_{max}} < 1$ $p.e.$ eliminating the cross talk signals introduces an additional inefficiency of 0.2%.

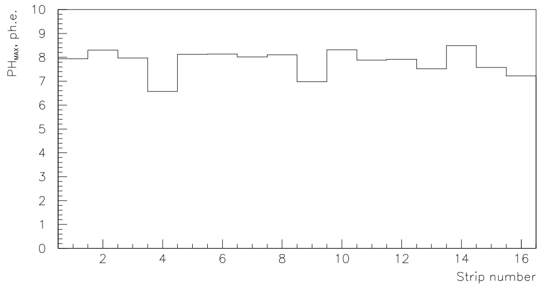

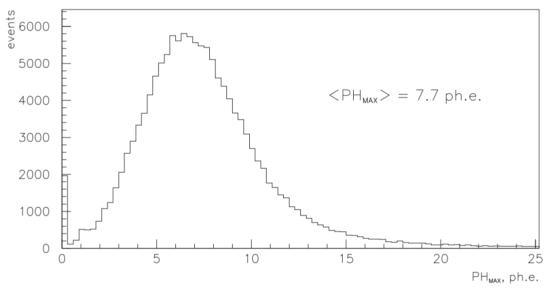

Figure 5.23: Scintillator strip response to a mip at 84 cm from the PMT. Left: average $\mathrm{PH_{max}}$ across one module, with each entry corresponding to a single strip. Right: the $\mathrm{PH_{max}}$ distribution in one module.

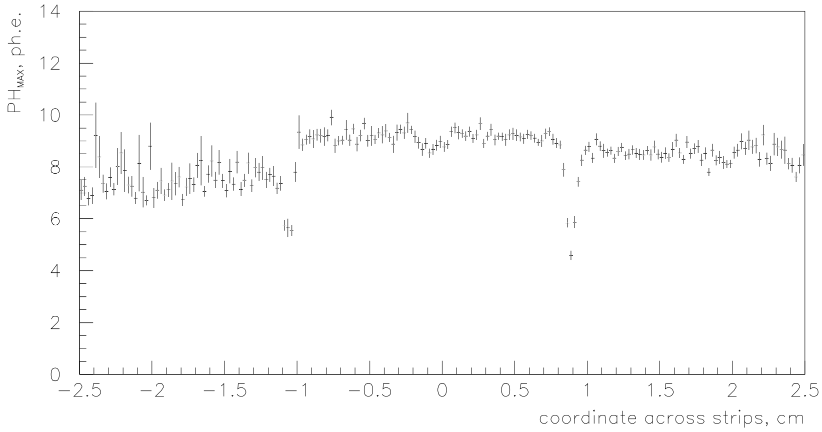

Figure 5.24: Average $\mathrm{PH}_{\max}$ around one strip.

5.2.3 Event location accuracy

The experimental setup simulating two OPERA target modules is shown in Fig. 5.25. It consists of two mini-walls of four dummy bricks, each followed by a pair of prototype scintillator strip planes oriented horizontally and vertically. The two pairs of strip planes are staggered transversally by 1 cm with respect to each other. Two types of dummy bricks were tested: one simulating OPERA bricks with spacers and containing 30 cells, and the other simulating compact bricks with 56 cells. In both, 1 mm thick lead absorbers are used. The beam telescope includes the BPCs and scintillator counters C1-C3. An additional larger counter C_μ, installed downstream behind a wall of 1.6 m iron and 2 m concrete, was used to tag beam muons. The setup was exposed to 15 GeV/c mixed beam of negative pions and muons, shifted diagonally by 2.5 cm away from the brick wall centre and defocussed to illuminate the area of $\sim 5 \times 5$ cm^2 (defined by the trigger counter C1).

We analysed two types of events: muon events, simulating CC neutrino interactions with a single leading track emerging from the brick (*e.g.* quasi-elastic events), and pion interaction events simulating deep-inelastic muon-less neutrino events. Muons are selected by requiring a hit in the C_μ counter and less than 6.5 mip for the total PH in the first three strip planes. Events with no hit in C_μ and more than 6.5 mip in the first three planes are identified as pions, mostly interacting in the first brick wall.

In each scintillator strip plane, centres of gravity of pulse-heights are calculated. Only strips with signals above 1 *p.e.* are retained. The pulse-heights are expressed in mip units to equalise all strips. The vertex position in one projection is determined as the mean value of the centres in two planes with the same orientation. The actual beam impact point in each event is accurately measured by the BPCs. The difference Δ (vertex) between the true and the reconstructed vertex positions is plotted in Fig. 5.26, representing data with spacer bricks.

For muon events, with predominantly one strip hit per plane, the rms vertex resolution is 0.62 cm. The Δ (vertex) distribution for muons can be approximated by two Gaussians with σ of 0.46 cm and 1.8 cm, the broader one containing less than 1% of events.

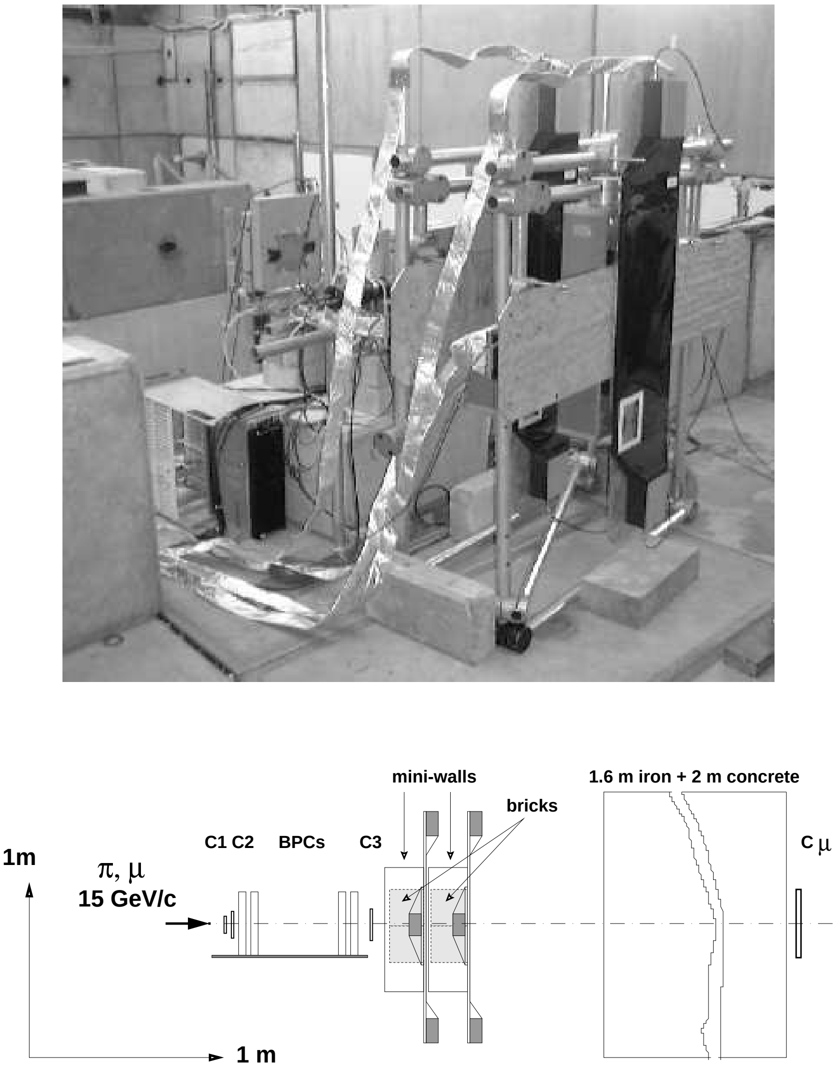

Figure 5.25: The experimental setup with prototype OPERA tracker mini-modules at the CERN PS T9 zone. Top: a general view. Bottom: a schematic layout of the setup.

For pion interactions, the hit multiplicity is much higher (up to all 16 strips per plane), and the *rms* spread in Δ (vertex) increases to 1.8 *cm*. The pion Δ (vertex) distribution, when approximated by two Gaussians, shows a narrow peak containing about two thirds of the events and having a σ of about 0.8 *cm* and a broad one with a σ of 2.2 *cm*.

Compact bricks show very similar results. In an additional measurement, the entire setup was turned by 100 *mrad* with respect to the beam, to simulate an average hadronic shower angle in neutrino events. Practically no change was found for both types of bricks.

5.2.4 EBCCD readout

A detector made of 54 scintillator strips made by different methods with three different types of WLS fibres has been tested with 15 GeV/c pions, by using an EBCCD for the readout[2].

A MegaPixel EBCCD tube with 40 mm photo-cathode and demagnification of 1.61 was used. The EBCCD chip has 1024×1024 pixels with active area of 13.4×13.4 mm^2. The useful area on the photo-cathode is 21.4×21.4 mm^2. A total of 525 fibres with 1 mm diameter. can be read out by such a tube. An Image Intensifier (II) by GEOSPHAERA with high quantum efficiency, optimised for green light (20% at 520 nm) was coupled to the EBCCD tube in order to increase the quantum efficiency up to a factor of two. A 10 *bit* ADC and a frame grabber connected to a PC was used to digitise the EBCCD signals.

We tested various scintillator strips with different cross sections, produced either by extrusion or by injection moulding. The length of the strips is in the range of $30 - 75$ cm. Polystyrene scintillator was used with three combinations of dyes: 1.5% PTP + 0.01% POPOP, 1% PTP + 0.01% POPOP and 1% PPO + 0.01% POPOP. Strips are coated by different materials: Teflon, tyvec, tetratec, aluminized mylar. Three different types of double cladding WLS fibres with 1 mm diameter were used: POL-HI-TECH S248, KURARAY Y11, and BICRON BCF91A. The far ends of the fibres had no mirrors.

Fig. 5.27 shows images of single photo-electrons from 1 mm WLS fibres 2.7 m long for a typical event, obtained from mip crossing 6 strips with cross section of 18×25 mm^2.

The test beam data are being analysed. Preliminary results are reported here. The best results were obtained with 18×25 mm^2 cross section made by extrusion, coated by tyvec with Y11 fibres. The fibres were glued at the centre of each strip. A mip produced 22.6 $p.e.$ at 1.25 m, 21 at 2.7 m and 13.4 at 5.7 m. This corresponds to a light attenuation length of 8 ± 1 m. For a similar strip 9 mm thick with the fibre glued in a groove on its surface 13.3 $p.e.$ were obtained at the distance of 2.7 m.

The same strips with 9×20 mm^2 cross section and 30 cm length made by UNILAST, previously tested with PMT readout, were also measured with EBCCD readout. A BCF91A fibre 1.2 mm in diameter and 2 m long was used. A light yield of 9 $p.e.$ at the distance of 1.85 m from the beam was measured. A light output of 7.7 $p.e.$ was obtained by PMT readout at a distance of 0.84 m. Extrapolated to the distance of 1.85 m according to the fibre attenuation curve, it corresponds to about 4.5 $p.e.$. This agrees well with the EBCCD measurement when taking into account the lower quantum efficiency of the PMT of about 10%.

We also tested three cells made of extruded white polycarbonate profiles with inner cross section of 9×8.5 mm^2 with 0.9 m length. The cells were filled with liquid scintillator EJ-399-01 (ELJEN TECHNOLOGY, US) and read out by KURARAY WLS fibres with 1.2 mm diameter. The result is 6.9 $p.e.$, measured at a distance of 2.5 m from the beam, 5 $p.e.$ at 5 m and 3.7 $p.e.$ at 6.5 m. This corresponds to an attenuation length of 7 ± 1 m.

[2]The work presented here has been carried out in collaboration with S. Golovkine, I. Kreslo and A. Medvedkov (IHEP, Protvino) and with the group of G. Martellotti (Rome).

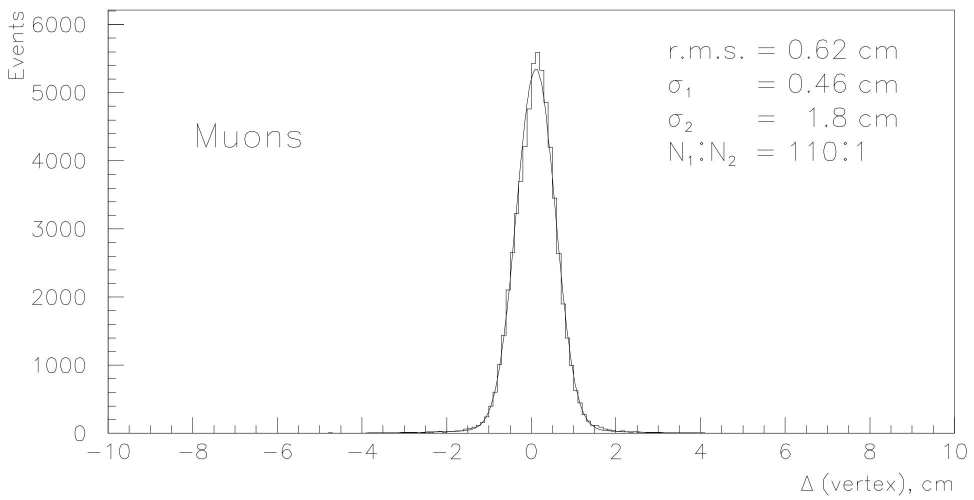

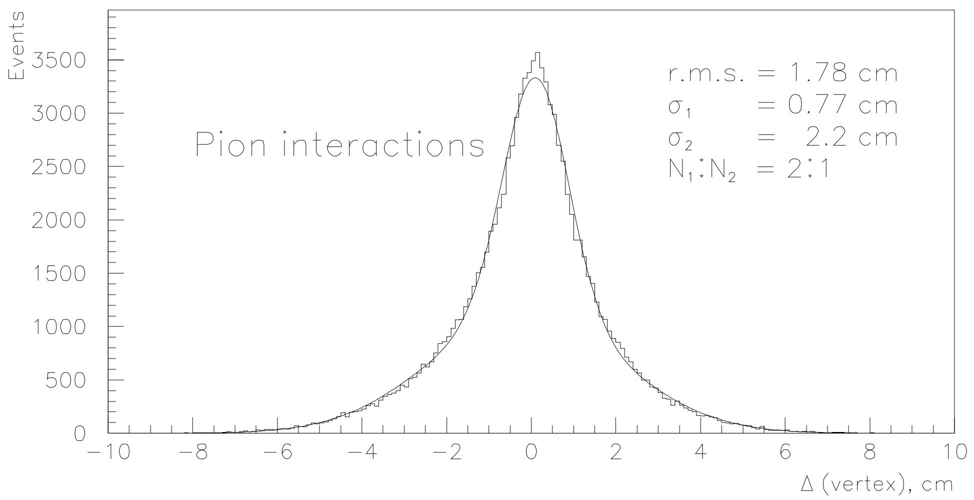

Figure 5.26: Δ (vertex) distributions for spacer bricks at 0 *mrad* beam incidence. Top: for muon events, bottom: for pion interaction events.

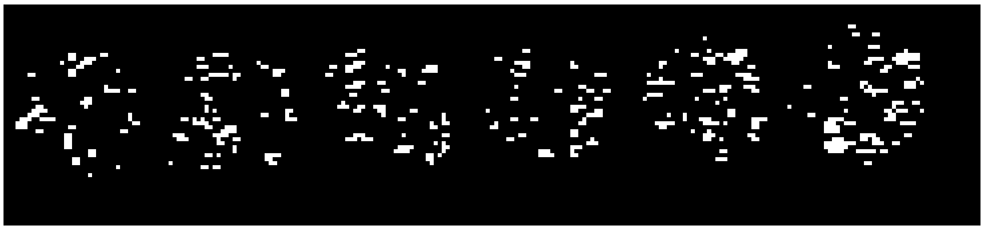

Figure 5.27: Typical image from the EBCCD. The display of the signal from six WLS fibres for a passing through *mip* is shown.

Chapter 6

The Collaboration

The OPERA Collaboration has increased since the Letter of Intent. The present members of the Collaboration agree to pursue studies and tests towards the realization of the proposal. After the CNGS approval, the groups will decide on the sharing of responsibilities for the construction of the detector. A preliminary list of the fields of interest of the various groups is given in Table 6.1.

Table 6.1: Fields of interest.

Item	**Institutions**
emulsion sheets	Nagoya, Salerno
emulsion handling	Bari, Kobe, Nagoya, Rome, Salerno, Toho
bricks	Israeli gr., Münster, Nagoya, Naples
target electronic detectors	Brussels, CERN, Frascati, Moscow, Münster
photo-detectors and electronics	Bern, Frascati, Hamburg, Israeli gr., IN2P3
mechanical structures	Bern, Brussels, CERN, Frascati, Nagoya, Naples
spectro. tracking and electronics	Frascati, Hamburg, IN2P3, Israeli gr.
spectro. scintillators	Brussels, CERN, Frascati, IN2P3, Moscow
magnets	Brussels, CERN, Frascati
trigger and DAQ	Bern, Hamburg, Moscow, Naples
emulsion scanning	Ankara, Bari, Bern, Münster, Nagoya, Naples, Rome, Salerno, Toho, Utsunomiya

Chapter 7

Conclusions and outlook

Since the OPERA LoI [16], experience has been gained on the ECC technique and several tests and simulations have been performed. Progress has been made in the understanding of the features and the basic design of the experiment as well as in the evaluation of the expected performance, in particular of the detection efficiency. The low background confirms the merits of the emulsion for the direct observation of the τ decay. Different lead-emulsion cell structures are being considered. Prototype bricks and electronic detectors have been exposed to test beams with encouraging results. Further studies are required with new tests in progress or planned.

OPERA implies an unprecedented, massive use of emulsion as tracking device of extremely high precision and granularity. It relies on the development of automatic scanning, on specific tests and on the experience with ECC detectors by the Japanese groups. The industrial procurement of the vast quantity of emulsion with adequate sensitivity is crucial. R&D programmes conducted jointly with emulsion producers are giving positive results. Automatic scanning continuously improves in speed and performance. The analyses being done for CHORUS and DONUT are furthering the understanding and stimulating improvements. An additional boost will be needed for the OPERA requirement of scanning large emulsion areas. The scanning performance is ultimately linked to the τ detection efficiency. The approaches under investigation exploit the progress in the electronics and in the technology of image analysis.

Electronic detectors require mature technologies to ensure adequate performance, cost effectiveness and high reliability. Different options are still open with tests done or underway. Collaboration with industry has started also for electronic detectors as well as for automation of the bricks assembly. The layout of the experiment and other technical issues have to be studied together with the Gran Sasso Laboratory.

The schedule for further studies, tests, R&D, prototyping, detector design and construction is tight. The near future will be devoted to assess the detector performance and to complete its design.

With the present running scheme of the CNGS facility, the OPERA sensitivity reaches $\Delta m^2 \sim 10^{-3}\ eV^2$, covering the oscillation parameter region indicated by Super-Kamiokande. A positive result from OPERA will clearly identify the source of the oscillations. If oscillations occur at the preferred Super-Kamiokande parameter values $\Delta m^2 = 3.5 \times 10^{-3}\ eV^2$ and $\sin^2 2\theta = 1$ the experiment will detect several unambiguous events. With these events, the oscillation parameters will be constrained. However, even a negative search would effectively contribute to the clarification of the oscillation scenario.

As the sensitivity is not limited by background, the experiment will profit from the statistics increase through a dedicated operation of the SPS or an improved performance of the CNGS.

Bibliography

[1] C. Weinheimer (Mainz Coll.), Proc. of the XVIII Int. Conf. on Neutrino Physics and Astrophysics, Takayama, 1998.

[2] V.M. Lobashev (Troitsk Coll.), Proc. of the XVIII Int. Conf. on Neutrino Physics and Astrophysics, Takayama, 1998.

[3] B. Pontecorvo, *Zh. Eksp. Teor. Fiz.* **33** (1957) 549.

[4] B. Pontecorvo, *Zh. Eksp. Teor. Fiz.* **34** (1958) 247.

[5] Z. Maki et al., *Prog. Theor. Phys.* **28** (1962) 870.

[6] B. Pontecorvo, *J. Exptl. Theoret. Phys.* **53** (1967) 1717;
V. Gribov and B. Pontecorvo, *Phys. Lett.* **B28** (1969) 493.

[7] Y. Fukuda et al., *Phys. Lett.* **B335** (1994) 237.

[8] M. Apollonio et al., *Phys. Lett.* **B420** (1998) 397;
M. Apollonio et al., hep-ex/9907037.

[9] Y. Fukuda et al., *Phys. Rev. Lett.* **81** (1998) 1562.

[10] C. Walter (Super-Kamiokande Coll.), Proc. of the Int. Conf. HEP 99, Tampere, 1999.

[11] Y. Fukuda et al., *Phys. Rev. Lett.* **82** (1999) 2644.

[12] W.W.M. Allison et al., *Phys. Lett.* **B449** (1999) 137;
A. Mann, XIX Int. Symp. on Lepton and Photon Int. at High Energies, Stanford, 1999.

[13] D.G. Michael (MACRO Coll.), Proc. of XXIX Int. Conf. on High Energy Physics (ICHEP), Vancouver, 1998.

[14] G. Acquistapace et al., CERN 98-02, INFN/AE-98/05, 19 May 1998.

[15] H. Shibuya et al., LNGS-LOI 8/97.

[16] K. Kodama et al., CERN/SPSC 98-25, SPSC/M612, LNGS-LOI 8/97, Add. 1.

[17] E. Eskut et al. (CHORUS Coll.), *Nucl. Instr.and Meth.* **A401** (1997) 7.

[18] A. Ereditato, K. Niwa and P. Strolin, INFN/AE-97/06, Nagoya DPNU-97-07, 27 January 1997.

[19] S. Aoki et al., *Nucl. Instr. and Meth.* **B51** (1990) 466;

[20] T. Nakano, Ph.D. Thesis, University of Nagoya (1997);
T. Nakano, The Ultra Track Selector, Nagoya University note, in preparation.

[21] M. Sakuda, KEK preprint 97-254.

[22] A. Curioni et al., hep-ph/9805249;
M. Aglietta et al., CERN/SPSC 98-28, SPSC/M615;
K. Winter et al., CERN/SPSC 98-36, SPSC/M623.

[23] E. Ables et al., Fermilab Proposal P-875 (1995);
NuMI-L-337 (1998);
NuMI-L-375 (1998);
http://www.hep.anl.gov/NDK/Hypertext/numi.html.

[24] The Fermilab NuMI Group, Fermilab Report NuMI-346, October 1998.

[25] The DONUT experiment: http://fn872.fnal.gov/;
T. Kafka (DONUT Coll.), *Nucl. Phys.* **B70** (1999) 204.

[26] M.F. Kaplon et al., *Phys. Rev.* **85** (1952) 900.

[27] J. Nishimura, *Soryusiron Kenkyu, Japan* **12** (1956) 24.

[28] J. Nishimura and K. Kamata, *Progr. Theor. Phys.* **5** (1950) 899;
J. Nishimura, *Hand. bd. Phys., Springer* **46/2** 1.

[29] C.M.G. Lattes et al. (Mt. Norikura exp.), Int. Conf. on Cosmic Rays, Jaipur, Vol. 5 (1963) 326;
M. Akashi et al., *J. Phys. Soc. Japan* **17** (1962) 427.

[30] S.L.C. Barroso et al. (Mt. Chacaltaya exp.), Proc. of the XXV ICRC, Durban, 1997.

[31] S.G. Bayburina et al. (Mt. Pamir exp.), Proc. of the XXIV ICRC, Rome, 1995.

[32] M. Akashi et al. (Mt. Fuji exp.), Proc. of the Cosmic Ray and Particle Physics Conf., Newark, 1978.

[33] J. Ren et al. (Mt. Kanbala exp.), *Phys. Rev.* **D38** (1998) 1417.

[34] K. Niu, E. Mikumo and Y. Maeda, *Progr. Theor. Phys.* **46** (1971) 1644.

[35] K. Niu, I Int. Workshop on Nuclear Emulsion, Nagoya, 12-14 June 1998.

[36] K. Hoshino et al., Contr. Paper at the 14th Int. Cosmic Ray Conf., Munich, **7** (1975) 2442.

[37] K. Hoshino et al., *Prog. Theor. Phys.* **53** (1975) 1859.

[38] N. Ushida et al., *Lett. Nuovo Cim.* **23** (1978) 577;
H. Fuchi et al., *Phys. Lett.* **85B** (1979) 135.

[39] H. Fuchi et al., *Lett. Nuovo Cim.* **31** (1981) 199.

[40] K. Niwa et al., Proc. Int. Cosmic Ray Symp. on High Energy Phenomena (Cosmic Ray Lab., Univ. Tokyo, 1974) 149.

[41] A. Ereditato et al., ICARUS-TM-98/13, OPERA 980722-01.

[42] R. Bailey et al., CERN-SL/99-034 (DI); INFN/AE-99/05.

[43] E. Eskut et al. (CHORUS Coll.), *Phys. Lett.* **B434** (1998) 205.

[44] B. Van de Vyver, *Nucl. Instr. and Meth.* **A385** (1997) 91.

[45] M.C. Gonzalez-Garcia and J.J. Gomez-Cadenas, *Phys. Rev.* **D55** (1997) 1297.

[46] J.M. Conrad et al., *Rev. Mod. Phys.* **70** (1998) 1341.

[47] N. Ushida et al. (E531 Coll.), *Phys. Lett. B* **206** (1988) 375.

[48] T. Bolton, hep-ex/9708014, 1997.

[49] Particle Data Group, *Euro. Phys. J.* **1** (1998) 1.

[50] T. Junk, CERN-EP/99-041, to appear on *Nucl. Instr. and Meth.*

[51] G.J. Feldman and R.D. Cousins, *Phys. Rev.* **D57** (1998) 3873.

[52] N. Armenise et al., CERN-SPSC/97-21 (1997).

[53] M. Doucet et al., hep-ex/9905029, 1999.

[54] S. Buontempo et al., *Nucl. Instr. and Meth.* **A413** (1999) 255.

[55] F.C. Porter et al. (BABAR Coll.), SLAC-PUB-7951 (1998).

[56] G. Abbiendi et al., *Nucl. Instr. and Meth.* **A333** (1993) 342.

[57] G. Rosa et al., *Nucl. Instr. and Meth.* **A394** (1997) 357.

[58] ATLAS muon spectrometer TDR, CERN/LHCC/97-22, ATLAS TDR 10, 31 May 1997, and references therein.

[59] WIRED Web Page: http://wired.cern.ch.